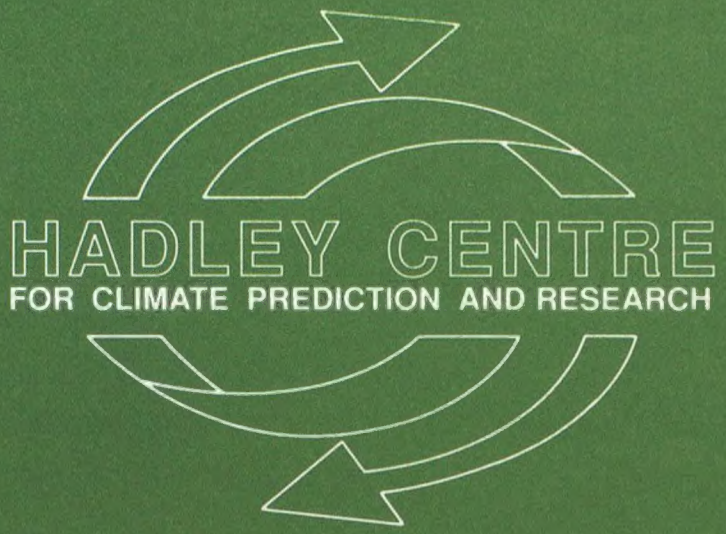

A prediction of the transient response of climate

by

J. M. Murphy

CRTN 32 September 1992

CLIMATE
RESEARCH
TECHNICAL
NOTE

Hadley Centre
Meteorological Office
London Road
Bracknell
Berkshire RG12 2SY

CLIMATE RESEARCH TECHNICAL NOTE NO. 32

A PREDICTION OF THE TRANSIENT RESPONSE OF CLIMATE

by

J M MURPHY

Hadley Centre for Climate Prediction and Research
Meteorological Office
London Road
Bracknell
Berkshire RG12 2SY
U.K.

NOTE: This paper has not been published. Permission to quote from it should be obtained from the Director of the Hadley Centre.

A PREDICTION OF THE TRANSIENT RESPONSE OF CLIMATE

1. Introduction

The atmospheric concentration of carbon dioxide (CO_2), and of certain other greenhouse gases, has grown steadily since the late 18th Century, leading to increased radiative heating of the Earth (see the Intergovernmental Panel on Climate Change (IPCC, 1990)). These increases, and the resulting warming of the Earth's climate, are set to continue into the next century. Once a new, constant level of anthropogenic greenhouse forcing becomes established, the response of climate may be expected to converge to some time-independent equilibrium value. The magnitude of the equilibrium warming will be determined by the signs and strengths of various feedbacks which occur in the climate system. For example, increases in atmospheric water vapour (Raval and Ramanathan, 1989), and reductions in surface snow and sea-ice cover (Ingram et. al, 1989), will act to increase the response, whereas changes in cloud distributions may either increase or decrease the response, depending on the nature of the changes (Wetherald and Manabe (1988), Roeckner et. al (1987), Senior and Mitchell (1992)).

Determination of the equilibrium response is an important task. Equally important, however, is to predict the time-dependent adjustment of climate towards equilibrium, i.e. the *transient* response. In addition to the climate feedbacks, this is influenced by the thermal inertia of the oceans (e.g. Hoffert et. al, 1980). If the anomalous heating generated within the atmosphere is transferred efficiently to the deep ocean, a significant response of surface temperature could be delayed by hundreds of years; alternatively, if the heating is confined to the top few metres of the ocean, the full response will be realised within a few years. Geographical variations in the efficiency of ocean mixing are likely to result in differences between the pattern of the transient response, and the pattern of the equilibrium response (Schneider and Thompson (1981); Bryan et. al (1988)). Furthermore, changes in the ocean circulation may influence both the transient response (Manabe et. al, 1991), and the equilibrium response.

Prediction of the transient response therefore requires a global coupled ocean/atmosphere general circulation model (AOGCM), which includes the deep ocean, and represents ocean dynamics explicitly. A suitable AOGCM has been developed at the Meteorological Office, and this has recently been used within the Hadley Centre in an experiment to predict the transient response. This report briefly summarises some of the main results from this experiment. The following Section describes the model and experimental design, and sets out the scientific difficulties encountered in seeking a stable simulation of the base climate of the AOGCM. Section 3 considers the modelled rise in global-mean temperature, comparing the results against corresponding experiments produced at other centres, and also against the observed temperature record. In Section 4 the global response patterns are presented, including an assessment of the role played by the ocean circulation in modifying the transient response. The evolution of the patterns is also considered. A summary of the results is provided in Section 5.

2. Experimental Details and Control Climate

A comprehensive description of the AOGCM is given in Section 2.1. Readers wishing to omit these details can skip to Section 2.2 without loss of continuity.

2.1 Model Description

Both the atmospheric and oceanic components of the AOGCM employ a horizontal grid with a spacing of 2.5 degrees in latitude and 3.75 degrees in longitude, with 11 vertical levels in the atmosphere and 17 in the ocean. The atmospheric model is a primitive equation sigma coordinate model, employing realistic geography with grid-box mean orographic heights. The dynamical formulation, and the distribution

of vertical levels, is as described by Slingo and Pearson (1987). The parametrisation of Palmer et. al (1986) is used to represent the drag on the large-scale atmospheric flow induced by the breaking of gravity waves excited by flow over mountains.

The radiation scheme, which is that employed by Wilson and Mitchell (1987), and by Slingo et. al (1988), includes the seasonal and diurnal cycles of insolation, and computes shortwave and longwave fluxes which depend on temperature and cloud amount, and also on the concentrations of water vapour, carbon dioxide and ozone. In the present experiment, layer clouds are predicted according to the scheme of Smith (1990), based on the use of an explicit cloud water variable. Within a given grid box, layer cloud cover is diagnosed from the difference between the total water content and the saturation specific humidity, assuming a simple statistical distribution about the grid-box mean value. Layer cloud is divided into three categories: low (bottom three levels), medium (next three) and high (next four). No cloud can exist in the top layer. At any given time cloud of a particular category is confined to one of its range of layers, taken to be the one in which the greatest amount of cloud is predicted. Cloud radiative properties are fixed, independent of cloud water content. Large-scale precipitation is parametrised in terms of cloud water content, with allowance made for the greater efficiency of precipitation when the cloud is glaciated. Evaporation of precipitation is accounted for, and below 0 Deg C precipitation is assumed to fall as snow. See Senior and Mitchell (1992) for a comparison of this version of the layer cloud scheme (which they refer to as 'CW'), with alternative formulations.

Convection is represented using the penetrative scheme of Gregory and Rowntree (1990), based on a calculation of convective mass flux using parcel theory modified by entrainment and detrainment, where the initial mass flux is taken to be proportional to the stability of the lowest convecting layers. Convective cloud amount is determined assuming a logarithmic dependence on the parcel liquid water path (Slingo et. al, 1988). No convective precipitation is allowed until the cloud has exceeded a critical depth of 4.0km over the land, and 1.5km over the sea, to represent crudely the effect of differing size distributions of cloud condensation nuclei (Gregory and Rowntree, 1990). If the cloud top is cooler than -15 Deg C, a value of 1km is used,to allow for precipitation produced by the growth of hail from the freezing of supercooled water droplets. The amount of precipitation is then determined by removing cloud condensate above a certain threshold.

In the atmospheric boundary layer, turbulent mixing is modelled using an eddy diffusivity approach, with stability-dependent transfer coefficients. The version of the scheme is that employed by Slingo et. al (1988), modified to allow for the presence of cloud water (Smith, 1990). The surface fluxes of heat, moisture and momentum are determined using simple bulk formulae, assuming that the flux is proportional to the local gradient multiplied by the surface wind speed. The transfer coefficients are derived from Monin-Obukhov similarity theory, and depend on stability, and surface roughness length (Slingo, 1985). Over sea points the effect of sub-grid scale gustiness associated with convection is accounted for, by adding an increment to the surface wind used in the bulk formulae for heat and moisture, proportional to the convective precipitation rate (Gordon, 1989). Over land, evaporation is restricted by including a 'surface resistance' term, intended to account for the influence of vegetation on moisture transport from the soil to the atmosphere (Warrilow et. al, 1986).

Land surface temperature is computed from the balance between the net heat flux from the atmosphere, and the surface soil heat flux, which is obtained from a four-layer model of soil thermodynamics, whose layer depths are chosen to optimise the response to forcing on timescales ranging from 1 day to 2-3 years. The surface hydrology scheme includes a vegetative canopy, which intercepts and stores some of the incoming rainfall. Water stored in the canopy is allowed to re-evaporate at zero resistance. Soil moisture content is augmented by throughfall (rainfall not intercepted by the canopy) and snowmelt, and reduced by evaporation and runoff.

Total runoff is the sum of 'fast' runoff, which occurs when the rainfall rate exceeds the maximum infiltration rate of the soil, and slow gravitational drainage from the root zone, which increases with soil moisture (see Warrilow et. al (1986) for further details of the surface hydrology and soil thermodynamics schemes). Note that in the present experiment, runoff from the land is not added to the ocean. Snow depth is increased by snowfall, and reduced by snowmelt and sublimation. Over snow-covered land, surface albedo varies between prescribed values for snow-free land and deep snow, according to an exponential dependence on snow depth. When the surface temperature is close to 0 Deg C, the deep snow albedo is reduced to account crudely for the ageing of the snow cover. At permanent land-ice points (i.e. over Greenland and Antarctica), a fixed albedo of 0.75 is used. Required soil and vegetation parameters (e.g. surface albedo, surface roughness, thermal conductivity, surface resistance to evaporation, etc.) are specified as spatially-varying values (Warrilow and Buckley, 1989).

The ocean model is based on that of Cox (1984), incorporating seventeen unequally spaced vertical levels (see Table 1), with a high resolution near the surface to allow the seasonal variation of the mixed layer to be represented. A realistic bottom topography, obtained from the US Navy Scripps 1x1 degree dataset, is employed. The equations of motion predict currents, potential temperature and salinity, treating the ocean as a hydrostatic, Boussinesq fluid. Fourier filtering is used north of 75 Deg N, in order to avoid instabilities arising from the small zonal grid spacing in this region. A rigid-lid boundary condition is employed at the surface, to remove external gravity waves. The vertical velocity at the sea floor is computed assuming flow parallel to the slope of the bottom topography, and zero vertical fluxes of momentum, heat and salt are specified. The lateral boundaries are treated as non-slip, with zero normal fluxes of heat and salt. A timestep of 30 mins. is used. Static stability is maintained through the use of a convective adjustment scheme: if the potential density profile between two vertically adjacent cells is unstable, temperature and salinity values are mixed so as to remove the instability. Density values are obtained using the equation of state for sea-water, according to the prescription of Bryan and Cox (1972).

The model grid is too coarse to resolve oceanic mesoscale eddies (of typical scale 100km), however they can be crudely parametrised as sub-grid scale turbulent diffusion and viscosity. In fact the coarse horizontal resolution dictates the use of a large horizontal eddy viscosity coefficient of $3.0 \times 10^9 cm^2 s^{-1}$, in order to achieve computational stability (Mead, 1988). This exceeds the range 10^6-$10^8 cm^2 s^{-1}$ thought to be appropriate for eddy mixing (Gill, 1982), hence the horizontal currents simulated by the model are too small (e.g. $10 cms^{-1}$ in the Gulf Stream cf $1 ms^{-1}$ observed). Lateral diffusion of temperature and salinity is carried out along isopycnal (constant density) surfaces, according to the formulation of Redi (1982). The coefficient of isopycnal diffusion varies exponentially with depth, decreasing from $2.0 \times 10^7 cm^2 s^{-1}$ at the surface to $1.0 \times 10^7 cm^2 s^{-1}$ at approximately 500 metres, and to $0.5 \times 10^7 cm^2 s^{-1}$ in the deep ocean. A small cross-isopycnal mixing coefficient of $0.1 cm^2 s^{-1}$ is assumed. In addition, a background horizontal diffusion of $2 \times 10^5 cm^2 s^{-1}$ is added to eliminate roughnesses in the horizontal temperature and salinity fields. Note also that within the surface mixed layer (see below), the isopycnal slopes are set to zero, so that the isopycnal diffusion represents purely horizontal mixing in this region. Vertical mixing (in addition to that produced when isopycnal surfaces are inclined relative to the horizontal) is parametrised using the scheme of Pacanowski and Philander (1981), in which the vertical eddy viscosity and diffusivity are functions of the local Richardson number, thus allowing for increased mixing when the local shear is large. The coefficients of diffusivity and viscosity vary from a background value of $0.1 cm^2 s^{-1}$ in very stable regions (e.g. below the main thermocline), to a maximum of $55 cm^2 s^{-1}$ in turbulent (e.g. near surface) layers.

The ocean model also contains an embedded mixed layer model, based on that of Kraus and Turner (1967), to account for the effect of wind stirring in promoting mixing of the surface layers. Of the mechanical energy input from the atmosphere, 70% is assumed to be available for mixing the ocean interior. Working downwards

from the surface, temperature and salinity are mixed between the existing mixed layer and the next layer down, depleting the mechanical energy to balance the resulting loss in potential energy (p.e.). Where the density profile is convectively unstable mixing leads to an increase in p.e., in which case the mechanical energy is increased by 15% of the gain in p.e. In addition, the mechanical energy is decremented exponentially with depth, with a scale depth of 100m. This process continues until all the available mechanical energy is used up.

The prediction of sea-ice is based on the 'zero-layer' thermodynamic approach of Semtner (1976). Changes in ice and snow depth arise from snowfall and sublimation, and from the net surface energy balance, involving the net flux from the atmosphere, the ocean to ice heat flux, and the diffusive heat flux through the ice (and snow). The ocean to ice flux is assumed to be proportional to the difference between the temperature in the top layer of the ocean, and the temperature at the base of the ice. The diffusive flux is calculated by assuming that temperature varies linearly in the ice and snow, with a change of gradient at the ice/snow interface caused by the lower thermal conductivity of snow. Ice depth can also increase by 'white ice' formation, which occurs when snow depth increases to the point where the ice/snow interface sinks below the waterline. The role of leads in the surface energy balance is accounted for by introducing a parametrisation of ice concentration, A, due to Hibler (1979), which assumes that the distribution of ice depth within a grid box is uniform over the range (0,2h/A), h being the grid-box average depth. Maximum values of A of 0.995 (Arctic), and 0.980 (Antarctic) are imposed, since completely unbroken ice cover is rarely observed in reality. Changes in ocean salinity arising from the freezing of sea water or the melting of sea-ice are accounted for, assuming a uniform salinity of 0.6% for sea-ice. In addition, sublimation of ice increases ocean salinity, (as the salt left behind is assumed to blow into the leads), and white ice formation reduces ocean salinity (to account for the salt added when the snow is converted to ice). Sea-ice surface temperature is computed in the atmosphere half of the coupled model, using a surface heat capacity set to a value which ensures that diurnal variations have a realistic amplitude. The surface albedo is specified as 0.5 at 0 Deg C, and 0.8 at and below -5 Deg C, with a linear variation between these points. The performance of the sea-ice model is discussed by Roberts and Cattle (1989).

The integration of the coupled model proceeds as a series of five day 'coupling intervals'. Within a coupling interval, the atmosphere model runs seperately for five days, with fixed sea surface temperatures (SSTs) and sea-ice extents, accumulating relevant time-mean surface fluxes, which are then used to drive a corresponding integration of the ocean model, following which the updated SSTs and sea-ice extents are passed back to the atmosphere for the next coupling interval. The quantities required to drive the ocean are wind stress, fresh water flux (precipitation minus evaporation), and downward energy flux, comprising net shortwave and longwave radiation, and turbulent fluxes of sensible and latent heat. All components of the energy flux are assumed to be absorbed exclusively in the top layer of the ocean, with the exception of shortwave radiation, a proportion of which penetrates to deeper layers according to the scheme of Paulson and Simpson (1977), assuming water type 1B of Jerlov (1968). With this choice, 82% of the incoming radiation is absorbed in the top layer, and none penetrates below 200m. At sea-ice points, the atmosphere computes seperate energy fluxes for the leads and icy portions of the grid box, and sublimation is also supplied as a component of the mass budget for snow/ice. In addition, 'wind mixing' (mechanical) energy, proportional to the cube of the surface wind speed (Kraus and Turner (1967)), is provided to drive the mixed layer model.

2.2 Experimental Design

The climate change experiment consisted of two integrations, each of 75 simulated years (see schematic Figure 1). In the 'Control' integration, CO_2 was held constant at 323 parts per million, in order to obtain a reference climate simulation. In the 'Anomaly' integration a 1% per year (compound) increase of CO_2

was prescribed, resulting in a doubling after 70 years. At any given time-level, the difference between the Anomaly and Control simulations is interpreted as the transient response to the increased forcing in the Anomaly run at that point. The experiment was performed on the Meteorological Office Cyber 205 computer. The AOGCM ran at the rate of approximately one simulated year per 24 hours of CPU time.

It is important to ensure that the Control climate does not 'drift' with time during the experiment, since any such drift may distort the simulated climate response. The experiment should therefore be initialised from a balanced state of the AOGCM, in which the atmospheric and oceanic components have been brought into equilibrium with one another. Whilst the atmosphere and land surface respond relatively quickly to a given forcing, the equilibration time scales for the ocean are much longer, ranging from a few years for the upper mixed layer (50 metres or so), to centuries for the deep ocean, due to the long transit times associated with the deep circulation. Thus a long integration of the ocean component of the AOGCM is required to obtain a suitable initial state.

As shown in Figure 1, this was carried out in a three-stage preliminary experiment. Firstly, the atmospheric model was run alone, with fixed climatological SST and sea-ice distributions. In Stage 2, time-mean atmosphere-ocean fluxes from this run were used to drive an integration of the ocean model, started from observed conditions of temperature and salinity, taken from Levitus (1982). During this stage, the ocean adjusted towards equilibrium with the driving atmospheric model fluxes. In stage 3 this process was continued as a coupled integration, thus allowing the AOGCM to establish an internally-consistent balance between its atmosphere, land surface and ocean components. The end-point of Stage 3 was taken as the initial state for the climate change experiment.

The total ocean 'spin-up' time was limited to 150 years on the grounds of computational expense. This was sufficient to achieve equilibrium in the top few hundred metres of the ocean at the end of Stage 3 (Figure 2). However, a slow warming trend persisted in the deeper layers, consistent with a net heat flux into the ocean (consisting of the net flux from the atmosphere plus the flux correction (see below)), of approximately 1.2 Wm^{-2}. Figure 2 shows that the deepest layers are the furthest from equilibrium after Stage 3, but the absolute rate of warming is larger near the base of the permanent thermocline, amounting to 0.6 Deg C per century between 500 and 1000m. On time scales of a century or less, a slow trend in the deep ocean is unlikely to cause a large drift in the climatically important surface variables, such as SST. Nevertheless, a longer spin-up time will be desirable in future experiments, in order to eliminate the risk that ongoing deep ocean adjustments may influence the simulated climate response.

2.3 Flux Correction

AOGCM simulations of present-day climate tend to develop large systematic errors (Washington and Meehl (1989); Manabe and Stouffer (1988)). These errors can be suppressed by adding artificial forcing terms to the fluxes simulated at the ocean-atmosphere boundary (Sausen et. al (1988); Manabe and Stouffer (1988)). In the present experiment, this process, known as flux correction, was carried out using a methodology similar to that of Manabe et. al (1991). Specifically, during stages 2 and 3, the sea surface temperature, salinity and sea-ice were continuously relaxed towards specified climatological values, thus limiting the development of systematic errors in the upper ocean simulation. The resulting forcing terms were then averaged over the last 10 years of Stage 3, as functions of position and season, to form constant flux correction fields. The flux corrections were then added to the surface heat and water fluxes simulated in the Control and Anomaly integrations, in order to maintain the base climate of the AOGCM close to reality.

Figure 3 compares the relative magnitudes of the heat flux correction and the

atmosphere-ocean heat flux. Typically the two terms are of comparable size, however the zonally-averaged values are opposite in sign almost everywhere. This suggests that the ocean model generally fails to achieve sufficient horizontal heat transport to maintain the correct local heat balance. This may be associated with the use of an unrealistically large horizontal viscosity, which is dictated by the coarse resolution of the ocean model (see Section 2.1).

The motivation for the flux correction scheme is confirmed by Figure 4(a), which shows the deviation of SST from climatology in an integration of the AOGCM without flux correction. A particularly large cooling occurs in the North Atlantic and Arctic Oceans, and there is a substantial warming in the Southern Ocean. Clearly errors of this magnitude must influence the climate response of the AOGCM, and are therefore unacceptable. Figure 4(b) shows that the inclusion of the flux correction terms is largely successful in suppressing these errors in the Control integration, particularly in the northern hemisphere. However, there is still a gradual warming in the Southern Ocean, leading to SST errors of up to 3 degrees in this region by the end of the experiment. This is sufficient to cause the disappearance of most of the Antarctic sea-ice, which degrades the ability of the AOGCM to model the temperature/albedo feedback correctly in the southern hemisphere.

It should be noted that the use of flux correction introduces other drawbacks: the flux correction terms have no physical basis, and it is necessary to assume that terms calculated with respect to a reference Control climate remain valid when the climate is perturbed. The reliability of this assumption is not clear. Future research should aim to reduce the size of the flux correction terms by improving the atmospheric and oceanic components of the AOGCM. In particular, the horizontal heat transport by the ocean may need to be increased, perhaps by refining the horizontal resolution of the ocean model grid. For example, a 1x1 degree grid would allow the use of a viscosity much closer to that thought to be appropriate for the real ocean. Tests are currently in progress with such a version of the ocean model. Note, however, that a 1x1 degree grid implies a significant increase in computational expense.

Finally, as discussed above, Figure 4(b) demonstrates that systematic errors can emerge *even with* a flux correction scheme in operation. In particular, the Southern Ocean warming is related to a gradual change in the strength of the deep ocean circulation during the Control integration. In this region, mixing between the surface and the deep ocean plays an important role in determining the properties of the surface layers (Bryan et. al, 1988). This mixing may be influenced by detailed features of the surface forcing operating in the AOGCM. For example, a test integration (not shown) suggests that the mixing is sensitive to the methodology for inserting the flux correction terms at sea-ice points. Further development of the experimental strategy is therefore needed, to avoid the occurrence of secular climate drift arising from subtle problems of this kind.

3. Global-Mean Temperature Response

Figure 5 shows the annually-averaged global-mean surface temperature response of the AOGCM. Initially the response is slow, showing a mean surface warming of only 0.2 degrees after 20 years, with almost no warming at all over the sea. Subsequently the response proceeds at a faster rate, close to 0.3 degrees per decade, with the land warming significantly faster than the sea. Averaged over years 66-75, the decade centred on the time of CO_2 doubling, the global-mean warming is 1.7 degrees. The effective AOGCM oceanic heat capacity, calculated by dividing the average net heat flux into the ocean by the mean rate of increase of SST, is equivalent to a column of water 403 metres thick. Over the ocean this implies that a net flux of 0.5 Wm^{-2} has to build up at the surface before a rate of warming of even 0.1 degrees per decade can be achieved, yet it takes 20 years before a flux of this magnitude becomes established. By contrast, the effective heat capacity of the land surface is very small, due to the inefficiency of soil as a conductor of heat, so the land temperature is able to respond immediately to

any anomalous heat flux from the atmosphere. Hence both the delay in the response, and its land\sea contrast, are associated with oceanic thermal inertia. However, other factors are also important, and these are discussed in Section 3.2 below.

3.1 Comparison of Transient Responses Simulated by Different AOGCMs

To date, AOGCM transient experiments have been carried out at four different climate modelling centres. These are the Geophysical Fluid Dynamics Laboratory (GFDL; Manabe et. al (1991,1992)) and the National Center for Atmospheric Research (NCAR; Washington and Meehl (1989)) in the USA, the Max Planck Institute (MPI; Cubasch et. al (1991)) in Hamburg, Germany, and the Hadley Centre at the UK Meteorological Office (UKMO). A brief comparison of these experiments is given below (see also the Supplementary Report of IPCC (1992)). Figure 6 compares the rate of warming simulated by each model. Also shown are lower and upper bounds for the transient response estimated by IPCC (1990), using calculations produced with the idealised one-dimensional climate model of Wigley et. al (1991). The lower and upper bounds assume a climate sensitivity of 1.5 and 4.5 degrees respectively, these being the IPCC (1990) limits on the likely equilibrium surface warming resulting from a doubling of CO_2, based on a range of evidence available from general circulation model studies, observational evidence and sensitivity analyses.

To interpret Figure 6, note that different forcing scenarios were used in the various experiments. The GFDL and UKMO experiments both used a 1% per year (compound) increase (CO_2 doubling time 70 years), whereas the MPI and IPCC curves both refer to the IPCC (1990) Scenario A 'Business-as-Usual' forcing. This is a faster rate of increase, giving a doubling time of 60 years. The NCAR experiment, which ran for 60 years, used a slower 1% per year (simple) scenario, giving a doubling time of 100 years. Accounting for these forcing differences, all four AOGCMs lie within the range given by IPCC beyond about year 50. The differences between the models are probably due mainly to differences in climate sensitivity. The NCAR model is the only one not to employ a flux correction scheme. In their model, this results in an underestimation of tropical SSTs, and an overestimation of high latitude SSTs. These systematic errors are likely to reduce climate sensitivity, by reducing the water vapour and temperature/albedo feedbacks respectively (Washington and Meehl, 1989). The GFDL model, which has an estimated climate sensitivity of 4.0 degrees, lies close to the top end of the range. The response of this model is quasi-linear throughout, with only a short initial delay. In contrast, the other three models exhibit a more pronounced delay. For example, at the CO_2 doubling point the MPI and UKMO experiments both show a response comfortably in the middle of the IPCC range, yet, over the first few decades, the warming is close to or below the lower bound. More experiments are needed to determine whether this enhanced delay is characteristic of the transient response, or simply a consequence of natural climate variability in these particular cases. Regarding the UKMO experiment, this issue is investigated further in Section 3.2.

The warming at the time of doubling is shown in Table 2. The results show that the range of uncertainty defined by IPCC cannot be narrowed on the basis of these AOGCM simulations. This reflects the continuing difficulty of developing optimum representations of sub-grid scale physical processes in AOGCMs, particularly those controlling the formation of clouds, which exert an important influence on the net climate feedback strength.

Table 2 also gives the fraction of the expected equilibrium response, F, realised at the time of doubling, showing that the AOGCMs are in reasonably close agreement. The existence of a gap between the realised and equilibrium responses arises from the storage of heat by the ocean, hence this result suggests that the models agree, at least in a gross globally-averaged sense, on the retarding effect of the oceanic thermal capacity. Note, however, that this is a rather crude comparison, since the magnitude of F is also likely to be influenced by other factors, such as the climate sensitivity (see IPCC (1990), Chapter 6), and the

forcing scenario.

3.2 Assessment of Response using an Energy Balance Model

This sub-section describes some calculations performed with a simple, globally-averaged energy balance model (EBM), in order to understand better the AOGCM response, and to assess its prediction in the light of the observed temperature record.

In the EBM, shown schematically in Figure 7, the land, ocean, troposphere and stratosphere are each represented by a single box, characterised by a temperature response, ΔT, and an effective heat capacity, C. For the land and ocean boxes, ΔT represents the mean surface temperature, whereas for the troposphere and stratosphere it represents the volume-averaged temperature. In each box (see Figure 7), the response is driven by an imposed radiative perturbation ΔQ. Resulting changes in the radiation lost to space are represented by $\lambda\Delta T$, the climate feedback term, and energy exchanges between connecting boxes by $k\,(\Delta T_{Box1}-\Delta T_{Box2})$. Once the feedback parameters λ and energy exchange coefficients k are known, the coupled energy balance equations can be integrated numerically to simulate the response to the imposed forcing.

The EBM was calibrated by using the fluxes and temperature response of the AOGCM to determine its adjustable parameters. For example, the effective heat capacity for each box was deduced by dividing the average net heat flux into the box by the average rate of change of box temperature. The surface feedback parameters λ_o and λ_l were calculated as the sum of separate contributions from short- and long-wave radiation. The short-wave component was taken as the change in net solar radiation absorbed at the surface, whereas the long-wave component was found from the change in outgoing surface infra-red radiation, allowing for the (estimated) long-wave transmissivity of the model atmosphere. The surface exchange coefficients $k_o(k_l)$ were then calculated from the remainder of the ocean(land)-atmosphere energy balance. The tropospheric and stratospheric feedback parameters λ_t and λ_s were determined by calculating the radiation budget at the top of the atmosphere separately over land and ocean points, and removing the contribution from the relevant surface feedback term. Finally, the tropospheric (or stratospheric) energy balance was used to obtain the troposphere-stratosphere exchange coefficient k_s.

For the forcing terms ΔQ, values for the instantaneous change in radiative heating resulting from an impulsive doubling of CO_2 were required. These were obtained by running a pair of one-timestep integrations from each of a number of atmospheric states extracted from the Control ($1xCO_2$) integration. Each pair of one-timestep runs consisted of a $1xCO_2$ member and a $2xCO_2$ member. The required forcing terms followed from the mean $2xCO_2$ minus $1xCO_2$ difference between the radiative fluxes at the surface, the tropopause (defined as the level where the maximum increase in the downward flux occurs, following Schmitt and Randall (1991)), and the top of the atmosphere.

3.2.1 Land\Sea Contrast in Response

Figure 8 shows the result of driving the EBM with the forcing scenario deployed in the AOGCM, with values of the heat capacities determined from years 1-75 of the AOGCM response, whereas the feedback parameters and energy exchange coefficients are based on years 46-75 (the significance of this choice of period is discussed in Section 3.2.2 below). The EBM slightly overestimates the ocean warming, for reasons discussed later. Nevertheless, the land\sea contrast in the response is reproduced well. An estimate of the equilibrium AOGCM response to a doubling of CO_2 was obtained by setting the rate of change of temperature to zero in the energy balance equations. The resulting equilibrium land warming is 3.7 degrees, compared to 2.4 degrees for the ocean, giving the global-mean value of 2.8 degrees quoted in Table 1. These figures can be approximately verified by referring to an existing study of the equilibrium response, namely the 'CW'

experiment of Senior and Mitchell (1992). This was carried out using the UKMO 'slab' model, in which the atmospheric general circulation model is coupled to a simple thermodynamic ocean, consisting of a 50m mixed layer with prescribed heat convergence terms to represent heat transport by ocean currents (see Wilson and Mitchell (1987)). Apart from a coarser horizontal resolution (5x7.5 degrees), the atmospheric model in CW is almost identical to that employed in the AOGCM, so the equilibrium surface warming is likely to be similar to that of the AOGCM. In fact, the equilibrium response for CW (global-mean 2.8 degrees; land 3.7 degrees; ocean 2.4 degrees) corresponds exactly with that obtained above. Whilst such a precise match is perhaps fortuitous, it does provide strong supporting evidence that the estimate obtained using the EBM is realistic.

As indicated in Section 3.1, the difference between the AOGCM transient response at the time of doubling (1.3 degrees ocean; 2.8 degrees land), and the predicted equilibrium warming, reveals the retarding effect of the ocean heat capacity. In principle, this factor may also influence the *land/sea contrast* in the transient response. In the AOGCM, however, the gap between the land and sea response at the time of doubling is 1.5 degrees, compared with a corresponding gap of 1.3 degrees in the equilibrium response. This suggests that only 0.2 degrees of the land\sea difference in the AOGCM can be attributed to oceanic thermal inertia.

Study of the AOGCM energy budget suggests that a more important factor may be the changes in net surface shortwave radiation. Averaged over years 46-75 there is increased absorption of 2.4 Wm^{-2} over land, after removing the contribution arising directly from the increase in CO_2. However, over the ocean the increase is only 0.4 Wm^{-2}. The disparity is related to the distribution of changes in cloud cover. On average, there is a reduction in medium-level cloud over both land and ocean. However, whilst low-level cloud also decreases over land, there is an increase over the ocean, which limits the increase in surface solar radiation. The effect on the temperature response was evaluated by re-running the EBM, with the shortwave contributions to the surface feedback parameters removed. The difference between the land and sea warmings at the time of doubling is reduced to 0.3 degrees, suggesting that 80% of the difference simulated by the AOGCM is accounted for by the shortwave feedback, with a maximum of 20% attributable to oceanic thermal inertia.

3.2.2 Delay in Response

In Section 3.1, it was remarked that despite possessing a climate sensitivity in the centre of the range specified by IPCC (1990), the initial response of the AOGCM lies close to or below the lower bound of the expected range for the transient response. It is therefore interesting to consider the factors influencing the shape of the response curve. Clearly heat storage by the ocean plays an important role in limiting the initial rate of response. This is demonstrated by the EBM curve in Figure 8, which shows that the rate of warming gradually increases with time as the anomalous flux at the ocean surface builds up. Nevertheless, the EBM still underestimates the delay in the AOGCM response over the first 15-20 years, resulting in an overestimation of the ocean response throughout. In principle, this could occur if the effective oceanic heat capacity, c_o, assumed constant in the EBM, actually decreased with time during the AOGCM experiment. Table 3 shows values of c_o calculated from individual 15-year periods of the experiment. The results are influenced by natural variability in both the simulated net heat flux into the ocean, and, in particular, the change in ocean surface temperature over the period in question (Figure 5). Nevertheless, there is clearly no evidence from Table 3 that c_o decreases with time.

In fact, as in Section 3.2.1 above, the explanation involves the surface shortwave feedback. In the EBM, it is assumed that the feedback parameters λ are constant, implying that the feedbacks are directly proportional to temperature. This is standard procedure in simple models of this type (e.g. Wigley et. al, 1991). However, the surface shortwave feedback in the AOGCM does not behave in this manner. In particular, over the ocean there is a small but significant

decrease in net downward shortwave radiation over the first 40 years of the experiment (see Figure 9(a)), whereas there is an *increase* over the last 30 years. Over land (Figure 9(b)), the shortwave feedback follows the linear law more closely, however there is a delay of around 15 years, before a (net globally-averaged) positive feedback sets in. This results in a time (or forcing) dependence of the AOGCM climate sensitivity. To illustrate this, Figure 10 shows alternative estimates of climate sensitivity, obtained from the EBM parameters as described in Section 3.2, where the EBM has been calibrated using a variety of different 30-year periods of the AOGCM experiment. Over years 1-30, for example, the AOGCM effectively behaves as a model with a small climate sensitivity of only 1.0 degrees. Later the climate sensitivity increases, levelling off at a value of 2.8 degrees over the last 30 years. The results of Figure 10 are subject to random error, arising from natural variability in the time-mean AOGCM fluxes and temperature changes from which they are calculated. However, estimates of the natural variability of relevant fluxes and temperature changes, obtained from the Control run, suggest that sampling effects are too small to explain the changes in climate sensitivity shown in Figure 10.

Further investigation is needed to identify the physical mechanism(s) underlying this time-dependent behaviour of the shortwave feedback (which appears to be linked to cloud changes), and hence the climate sensitivity. Nevertheless, the effect on the AOGCM response can be quantified using the EBM. This was done by repeating the EBM integration of Figure 8, with the surface shortwave feedback terms parametrised as simple functions of the CO_2 forcing, chosen so as to match the time-dependent behaviour observed in the AOGCM. For both ocean and land, an improved match to the AOGCM response over the first 20 years resulted (not shown), and the positive bias in the subsequent ocean response was removed. It is therefore reasonable to conclude that the delayed response of the AOGCM is partially due to a corresponding delay in the onset of positive feedbacks associated with increased net surface shortwave radiation, particularly over the ocean. The gap between the EBM and AOGCM curves in Figure 8 indicates the magnitude of this effect. If confirmed by future experiments, this has implications for the problem of climate change detection (see Section 3.2.3 below).

3.2.3 Comparison with Observed Temperature Record

The EBM can be used to estimate the likely response of the AOGCM to alternative CO_2 forcing scenarios, by changing the forcing profile $\Delta Q(t)$. For example, by choosing $\Delta Q(t)$ to match the anthropogenic greenhouse forcing for the period 1765-1990, the simulated transient response can be assessed against the observed temperature record. A suitable forcing scenario was therefore constructed by calculating equivalent CO_2 concentrations to represent the combined forcing arising from increases in carbon dioxide, methane (and associated stratospheric water vapour), nitrous oxide and the chlorofluorocarbons (CFCs). The required estimates of historical trace gas concentrations were taken from IPCC (1990). Note that the CFC contribution does not include the compensatory negative radiative forcing thought to arise from the role of halocarbons in promoting stratospheric ozone depletion. According to Ramaswamy et. al (1992), this may reduce the effective CFC forcing by 80%, thus reducing the total equivalent CO_2 forcing in 1990 by 9%, from 2.45 Wm^{-2} to 2.22 Wm^{-2}. Whilst this represents a non-trivial difference, it is not large enough to alter the main conclusions reached below. In contrast, the cooling effect of aerosols resulting from sulphur emissions may have offset a significant proportion of the greenhouse forcing (IPCC, 1992). This issue is considered in Section 3.2.4.

Figure 11 shows the result of driving the EBM with the above forcing scenario, where the EBM parameters correspond to the 2.8 degree constant climate sensitivity (CCS) case of Figure 8. The EBM overestimates the observed warming. (The observed land temperatures are taken from Jones (1988, updated), and the sea temperatures from a new UKMO analysis, described in Section CS.1.2.1 of IPCC (1992)). By 1990, there is a substantial difference of at least 0.5 degrees over

land, with a smaller difference of approximately 0.1 degrees over the ocean. In assessing these differences, it is important to consider the variability in the observed record. Whilst the land(sea) temperature has increased by about 0.6(0.5) degrees since the mid-19th Century, the rises have not been regular. Between 1910 and 1940, for instance, the rate of warming exceeded that predicted by the EBM, whereas from 1940 to 1970 there was a *decrease* in temperature, suggesting that much of the variability takes place on time scales of 10 years or longer. Therefore, whilst the EBM ocean warming exceeds the observed warming in every year bar one beyond 1960, the possibility that this is due to natural variability cannot be ruled out. Over land, however, the difference beyond 1950 is sufficiently large to conclude with some confidence that the overestimation of the warming is genuine.

Assuming that the above conclusion also applies to the EBM ocean warming, it is interesting to consider candidate reasons for the differences. The most obvious is that the AOGCM climate sensitivity is larger than that of the real climate system. Certainly the range of responses shown in Figure 6, for example, is sufficient to encompass the gap between model and observations in Figure 11. However, alternative explanations exist, and these are discussed below.

For example, the AOGCM may simulate the wrong value of the effective ocean heat capacity, c_o. However, the EBM response is not very sensitive to c_o. For example, increasing c_o by 20% leads to a reduction of less than 0.05 degrees in the 1990 warming. Whilst this may be marginally sufficient to account for the excessive warming over the ocean, it clearly does not explain the much larger difference over land.

Another possibility, following from Section 3.2.2, is that the effective climate sensitivity of the Earth may have varied over the period 1765-1990. To investigate this properly requires an AOGCM transient experiment using the observed anthropogenic forcing profile. However, a crude assessment can be made by assuming that the relationship between the AOGCM surface shortwave feedbacks and the imposed CO_2 forcing implied by Figure 10 remains valid under the forcing scenario of Figure 11; in other words, that the climate sensitivity depends on the *value* of the forcing, but not on the *history* of the forcing. Accordingly, Figure 11 shows an alternative EBM prediction, obtained by including the forcing-dependent parametrisations of the surface shortwave feedback terms used in Section 3.2.2. Over land, the warming is retarded until the increase in equivalent CO_2 forcing reaches 20% (i.e. in the late 1930s), but then recovers towards the CCS value once a positive short-wave feedback sets in. Beyond 1960 there is little difference from the CCS case, hence the gap between the EBM and observations cannot be explained by variable climate sensitivity. Over the ocean, however, the transient response is reduced by a significant amount (almost 0.2 degrees at 1990), which is indeed sufficient to encompass the discrepancy between model and observations. This reflects the fact that, relative to the CCS case, the difference in feedback is larger over the ocean (see Section 3.2.2).

3.2.4 Sensitivity to Assumed Anthropogenic Forcing Profile

Finally, the specified forcing $\Delta Q(t)$ may not match that experienced by the real climate system. This could arise, for instance, from interannual variations in the amount of solar radiation reaching the Earth. Alternatively, as discussed below, the anthropogenic forcing may differ from that prescribed above.

In particular, interest has grown recently in the role of tropospheric sulphate aerosol in the Earth's radiation budget. Aerosol particles exert a cooling influence on the globe by scattering incoming solar radiation back to space. (In fact, through their role as cloud condensation nuclei, they may indirectly cause a further cooling by increasing the reflectivity of clouds (Charlson et. al, 1992), but this aspect will not be considered here). Until recently, the tropospheric aerosol burden has been interpreted as a constant background arising from natural processes, however it is now clear that a

significant proportion is due to industrial emissions. This component gives rise to a time-dependent anthropogenic radiative perturbation, which must be added to that associated with increased trace gas concentrations.

Charlson et. al (1991) have calculated the present-day radiative perturbation associated with anthropogenic sulphate aerosol. They used a numerical model of the transport and chemistry of sulphur compounds, driven by the input from surface sulphur emissions, to predict the geographical distribution of the tropospheric aerosol burden. The effect on the solar flux at the TOA was then determined from an approximate calculation of the optical properties of the aerosol layer, which is assumed to be confined to the atmospheric boundary layer. Globally-averaged, the estimated perturbation is a cooling of 0.6 Wm^{-2}. This represents a significant modification to the current heating of about 2.5 Wm^{-2} due to the enhanced greenhouse effect. Unlike the anthropogenic greenhouse forcing, however, the aerosol forcing is spatially highly inhomogeneous, due to the relatively short lifetime (about 6 days) of aerosol particles in the troposphere. For example, the forcing is concentrated in the northern hemisphere, where over 90% of anthropogenic sulphur is emitted. Furthermore, on average the cooling at the TOA is much larger over land points than over ocean points (1.3 Wm^{-2} cf 0.3 Wm^{-2}, H Rohde (personal communication)). At the surface, the cooling exceeds the corresponding TOA value, since some of the solar radiation reflected from the top of the aerosol layer is absorbed in the atmosphere. Based on a value (used by Charlson et. al) of 0.76 for the mean atmospheric transmissivity of solar radiation, the surface forcing is 1.8 Wm^{-2} over land, and 0.4 Wm^{-2} over ocean.

The anthropogenic aerosol forcing was included in the EBM by specifying the radiative perturbation at the TOA, the tropopause and the surface (see Section 3.2), based on the values given above, and assuming zero flux divergence in the stratosphere. Taking those values to be appropriate for 1990, an aerosol forcing profile was constructed by making the simple assumption that the historical aerosol concentration was proportional to the corresponding equivalent CO_2 concentration. (Note that due to the short lifetime of the aeresol particles in the troposphere, it would strictly be more accurate to relate the historical aerosol concentration to the rate of CO_2 emissions (e.g. Figure 1.5 of IPCC (1990), however this is unlikely to make a significant difference to the results given below).

Figure 12(a) shows the result of running the EBM (CCS version), with the aerosol forcing included. Over the ocean, there is a reduction in the surface warming, similar to that arising from the forcing-dependent shortwave feedback. The major effect is over land, however, where the forcing is sufficient to offset the greenhouse warming completely. Indeed, a cooling trend is initiated beyond 1960. This is because the aerosol forcing is linearly dependent on concentration, whereas the CO_2 forcing has a logarithmic dependence, so that the aerosol forcing becomes proportionately greater at higher concentrations.

It is important to emphasise that the estimated aerosol forcing is subject to many uncertainties. These range from errors in the estimated source strengths for sulphur emissions, to the many approximations made in converting the aerosol burden into a radiative forcing, such as the use, for example, of empirical estimates of the short-wave scattering properties of the aerosol. Overall, Charlson et. al estimate that their values are uncertain to within a factor of two. To account for this, Figure 12(b) shows the effect of halving the aerosol forcing in the EBM, which removes the net cooling trend over land in the latter part of the record. Nevertheless, there is still a considerable reduction in the warming over land compared with the no-aerosol response. Indeed, the response fits the observations quite well over both ocean and land in this case. Also, the resulting reduction in global-mean temperature at 1990, 0.3 Deg C, lies in the middle of a range of 0.15-0.45 Deg C for the sulphate aerosol cooling, suggested by some recent calculations of Wigley and Raper (1992), although their aerosol forcing included an estimate of the cloud reflectivity effect, omitted in the present study.

The results of Figure 12 demonstrate the potential sensitivity of the transient response to the direct anthropogenic aerosol forcing. In particular, they suggest that the spatial inhomogeneity in the forcing offers a possible explanation for the absence in the observed record of the land/sea contrast seen in the AOGCM response. A priority now is to refine the estimates of the aerosol-induced component of the response. This requires, firstly, a more precise specification of the forcing. (Note, in this connection, that Penner et. al (1992) suggest that there is a further direct anthropogenic aerosol forcing, associated with smoke particles arising from biomass burning. According to their calculations, this may give an additional global-mean cooling of approximately 1 Wm^{-2}). Secondly, a more rigorous calculation of the sensitivity of the climate response is needed, involving, for example, the use of a general circulation model to predict the regional response to an imposed, spatially-varying radiative perturbation designed to represent the reflectivity of the aerosol layer. Beyond this, the indirect radiative perturbation associated with possible (sulphate and smoke) aerosol-induced increases in cloud albedo also needs to be addressed.

4. Global Response Patterns

4.1 Surface Temperature

Until recently, general circulation modelling studies of greenhouse-gas induced climate change have concentrated on the equilibrium response to a doubling of CO_2. A particular example is the 'CW' slab model experiment of Senior and Mitchell (1992), in which the atmospheric component is almost identical to that of the AOGCM, apart from a coarser horizontal resolution (see Section 3.2.1). Figure 13 compares the equilibrium response of annual-mean surface temperature predicted by this model against the AOGCM transient response at the time of CO_2-doubling (years 66-75). The amplitude of the AOGCM response is generally smaller, since it has not yet reached equilibrium with the imposed forcing. Nevertheless, the geographical distributions show a number of common features. In the northern hemisphere there is a poleward amplification of the warming, associated with the retreat of sea-ice cover (not shown). In the zonal mean, the land warming exceeds the ocean warming almost everywhere, the biggest contrast occurring in northern mid-latitudes (see Section 4.3 below). In winter, the warming over northern continents is maintained, thanks, at least partially, to the release of heat stored in the high latitude ocean during the summer. As in other models (see IPCC, 1990), the response is smaller in the tropics, where a greater proportion of the surface radiative heating is used to increase evaporation, rather than to raise surface temperature; the increased evaporative cooling reduces the surface warming relative to higher latitudes. Also, compared with higher latitudes, the warming is transferred more efficiently to the upper troposphere, due to enhanced latent heat release in tropical convection.

There are two main areas of difference, however, between the AOGCM and slab responses (see also Manabe et. al, 1991). Firstly, in the Southern Ocean the poleward amplification seen in the slab experiment is absent in the AOGCM. Secondly, the AOGCM response is also relatively small in the North Atlantic Ocean, compared with the North Pacific, whereas this is not the case in the slab model. These differences are associated with geographical variations in the downward penetration of the ocean warming simulated by the AOGCM (see Figure 14). In the Southern Ocean, the warming is distributed over the entire depth of the water column, hence the effective oceanic heat capacity is very large in this region, and the surface response is relatively small. An enhanced downward penetration of the warming also occurs in the North Atlantic sector, leading to a significant zonal-mean response down to about 1.5 km at 60 Deg N. In contrast, the response in the tropics and mid-latitudes is generally confined to the upper 500 metres of the ocean. In these regions, advection and diffusion are the dominant mechanisms for transferring heat between the surface mixed layer and the deep ocean. Since oceanic vertical currents are small below the near-surface layers (typically a few centimetres per day), and the heat capacity of the water is large, the time-scales

associated with these processes are long. At high latitudes, however, winter cooling increases the density of surface water, resulting, at certain locations, in the onset of deep convection. This promotes increased mixing between the surface and the deep water, leading to the deep ocean warming shown in Figure 14.

4.2 Influence of Changes in Ocean Circulation

These results demonstrate the importance of accounting for the deep ocean when modelling the transient response. In principle, the consequent variations in effective ocean heat capacity could be catered for simply by introducing a refined slab model, incorporating prescribed spatial and seasonal variations in the thickness of the slab. However, since the slab model lacks an explicit representation of ocean dynamics, such an approach ignores the possibility of changes in the ocean circulation.

However, the AOGCM is equipped to model such changes. To explore this issue further, Figure 15(a) illustrates the mean meridional circulation produced by the Control simulation. In addition to the presence of three major wind-driven cells, there are two large-scale thermohaline overturning cells, centred at 55 Deg N, and 65 Deg S. These cells, associated with the aforementioned high-latitude convective mixing, are of especial interest in this case. The northern hemisphere cell is confined to the Atlantic, involving northward transport of warm, saline sub-tropical water in the upper ocean, a sinking branch at 60 Deg N, coincident with the site of convective deep water formation, and a compensating southward return flow at depth. In the corresponding southern hemisphere cell the deep water formation occurs adjacent to the coast of Antarctica, driven partly by brine rejection associated with seasonal sea-ice growth (Manabe et. al, 1990).

Relative to the Control, the Atlantic cell weakens by about 25% during the Anomaly integration (Figure 15(b)). A similar reduction has been observed in the corresponding experiment at GFDL (Manabe et. al, 1991). As in the GFDL case, the change appears to be related to a reduction in the salinity of the surface water in the North Atlantic, perhaps caused by an increase in the net surface fresh water flux, arising from increased precipitation (see Section 4.3). Reduced salinity increases the stability of the water column, thus tending to inhibit the deep mixing which drives the thermohaline overturning.

Figure 15 shows that the Antarctic overturning cell is also slightly weaker in the Anomaly experiment. Interpretation of this feature is, however, complicated by the fact that the cell strengthens substantially *throughout both the Anomaly and Control integrations*, due to climate drift (see Section 2.3). Since the onset of this drift happens to be slightly delayed at the start of the Anomaly run (probably due to natural variability), at any given stage the Antarctic cell is always a little weaker compared with the Control. Therefore, whilst the Anomaly integration shows increased precipitation south of 40 Deg S during its latter stages, it is not clear that the reduced strength of the Antarctic cell can be associated with the resulting change in surface buoyancy forcing.

Nevertheless, these reductions in thermohaline overturning are examples of how the ocean circulation can, in principle, interact with other aspects of the climate response. It is important to establish the effect of such changes on the surface warming in the relevant areas. Remember that irrespective of any dynamical response, a reduced warming would be expected in the North Atlantic and the Southern Ocean, due simply to the large effective heat capacity in these areas. In fact, the results of Manabe and Stouffer (1988) show that a reduction in thermohaline overturning may have a significant additional cooling effect on the North Atlantic. They examined two alternative steady states of the GFDL coupled model, under identical boundary conditions, where the two equilibria were distinguished by the presence or absence of the Atlantic thermohaline circulation. North Atlantic SSTs were found to be up to 7 degrees colder in the integration without the thermohaline overturning, due to the absence of any net northward advection of warm water in the surface layers. Furthermore, Manabe et. al (1990)

show that a reduction in convective mixing in the Southern Ocean can also lead to a reduction in SST. This is because the deep water is warmer than the surface water in this region, hence a decrease in mixing tends to cool the surface. In short, these results suggest that the circulation changes of Figure 15 will indeed have accentuated the difference between the slab model and AOGCM response patterns of Figure 13, particularly in the North Atlantic; however a quantitative assessment requires further analysis of the AOGCM ocean heat budget.

4.3 Seasonal Response

The surface temperature patterns averaged over December, January and February (DJF), and over June, July and August (JJA), are shown in Figure 16 for the decade of doubling. The seasonal contrasts revealed are in many respects similar to those observed in typical slab model equilibrium doubling studies (see IPCC, 1990).

For example, the northern hemisphere high latitude response is much larger in DJF than in JJA. Most of the excess surface heating in summer is used in melting sea-ice, and even in areas where sea-ice disappears completely, the heat capacity of the ocean mixed layer prevents a large warming, despite the presence of a substantial temperature/albedo feedback. In late autumn and winter, however, the heat stored during the summer delays the re-formation of sea-ice, and the associated drop in surface temperature. Also, the sea-ice formed is thinner, allowing a greater heat flux through the ice from the ocean below. Thirdly, the high-latitude temperature inversion in the winter atmosphere confines the warming to the surface layers (see Ingram et. al, 1989).

Also common to equilibrium studies is the large warming over the mid-latitude northern continents in both summer and winter. In summer, the warming is increased by the absorption of additional solar radiation due to reductions in cloud cover. From 30-50 Deg N, an increase in short-wave heating is also apparent during winter, again associated with cloud changes. Further north, there is no such increase, despite significant reductions in continental snow depth in many areas. Here, the land surface warming is maintained largely by the release of heat stored in the high-latitude ocean during summer.

In the tropics, there is little seasonal variation in the oceanic response. The area of reduced warming in the North Atlantic also persists throughout the year, being somewhat more extensive in winter when the oceanic mixed layer is at its deepest. There is also an area of cooling centred on Alaska in DJF, which is associated with increased northerly flow arising from a rise in surface pressure over the North Pacific (see Figure 20(a), Section 4.5).

In contrast to the corresponding slab model results, the southern hemisphere oceanic response decreases at higher latitudes in JJA. This is due mainly to the coupling between the surface and the deep water in southern winter, which increases the effective heat capacity of the ocean (See Section 4.2). Note also that, as discussed in Section 2.3, the gradual disappearance of most of the Antarctic sea-ice during the Control integration prevents the occurrence of a significant temperature\albedo feedback, and therefore of any seasonal heat storage effects of the type described above.

The seasonal response of precipitation is shown in Figure 17. Between the pole and 45 degrees, there are zonal-mean increases over the ocean of typically 0.2 mm/day in both hemispheres for summer and winter alike. This is consistent with additional meridional moisture transport arising from increased specific humidity in the Anomaly experiment, and is in accordance with results from equilibrium studies (see IPCC, 1990). In DJF, there are also increases over land at mid- and high-latitudes in the northern hemisphere; however in JJA reductions occur over large areas of the mid-latitude continents, notably over the whole of southern Europe, much of the central United States and parts of central Asia. These reductions appear to be related to decreases in local surface evaporation, arising from reductions in soil moisture content (not shown), in areas where the

soil is already sufficiently dry to restrict the surface moisture flux.

In both DJF and JJA, there is a modest increase in the tropical maximum of precipitation to the north of the equator, accompanied by a decrease to the south. This is consistent with the change in the mean meridional circulation (not shown), which shows a rising branch to the north of the equator and compensatory sinking to the south , reflecting the interhemispheric asymmetry in the temperature response, wherein the warming in the northern tropics exceeds that in the southern tropics (Figure 16). The pattern of tropical changes in Figure 17 is complex, showing detailed small-scale structure. Some of the increases appear to represent an *in situ* enhancement of existing rainfall maxima simulated by the Control. This is particularly true in JJA, when the change in the mean meridional circulation acts to intensify the existing Hadley circulation. For example, the bands of increased rainfall over the east and central Pacific, and over the Atlantic, are coincident with the site of the Inter Tropical Convergence Zone in the Control. In common with a number of other models (IPCC, 1990), there is an intensification of the Asian summer monsoon, and there is also an increase over the eastern Sahel. Due to the large interannual variability of precipitation, the statistical significance of the changes is difficult to establish from a single 10 year period. However, the major features in the corresponding patterns for earlier decades (from around years 21-30 onwards) generally show good agreement with Figure 17, especially in JJA, increasing confidence in the statistical reliability of the changes. To place the results in context, it must be emphasised that there is currently little agreement between models regarding the pattern of the tropical response (IPCC, 1990), due, for example, to the sensitivity of the simulated precipitation patterns to sub grid-scale processes such as convection, cloud formation, and surface evaporation, the representations of which vary substantially from one model to another.

4.4 Evolution of Temperature Response

Figure 18 illustrates the annual-mean surface temperature response for years 21-30 and 41-50, to be compared with the response for years 66-75 shown in Figure 13(b). In the northern hemisphere, the main characteristics of the pattern are similar in all three periods. An enhanced warming over the mid-latitude continents is clearly established by years 21-30, and evidence of a polar amplification of the response is also present. Both of these features increase in amplitude between years 21-30 and 41-50; however their *relative* magnitudes alter somewhat between the two periods, such that the polar amplification becomes more pronounced. This is probably associated with the time-dependent behaviour of Arctic sea-ice cover (not shown). Whilst there is already a significant decrease in the total mass of Arctic sea-ice at years 21-30, there is only a slight reduction in areal cover at this stage. Beyond about year 40, however, the reduction in areal cover becomes larger. This leads to a temperature\albedo feedback, which acts to accelerate the high latitude response. An area of cooling is apparent in the North Atlantic at years 21-30, even though the reduction in Atlantic thermohaline overturning does not begin to occur until approximately year 35. This shows that the deep winter mixed layer in this region is effective in delaying the response, independent of any change in the ocean circulation (cf Section 4.2).

In common with years 66-75, the tropical response is smaller than the extratropical northern hemisphere response at years 21-30 and 41-50. However, even at years 21-30, the tropical warming is spatially uniform (apart from certain areas in the southern hemisphere tropics, discussed below), despite typically amounting only to 0.2-0.3 degrees. Figure 19 illustrates the statistical significance of the response for years 21-30, calculated separately at each grid point using a two-tailed Welch test (see Appendix). The results show that the tropical response is just as significant as the extratropical northern hemisphere response, reflecting the smaller level of natural variability in the tropics, and also the fact that the oceanic heating is initially confined to a relatively shallow layer, due to the absence of any significant seasonal deepening of the mixed layer. This suggests that, despite the increased response at extratropical

northern latitudes, the initial detection of a definite change in climate is equally likely to occur in some other part of the globe.

In the Southern Ocean, the response shows a cooling during the first 60 years of the experiment, which is eventually replaced by a modest warming over the last 15 years. As discussed in Section 4.1, the smallness of the warming at years 66-75 can be understood in terms of the large effective heat capacity of the Southern Ocean associated with deep convective mixing. However, whilst the preceding cooling apparent in Figure 18 is a statistically significant feature, it is not necessarily a physically reliable component of the transient response, since it is associated with the aforementioned climate drift in the Southern Ocean (Sections 2.3 and 4.2). This drift manifests itself as an absolute warming in the surface layers during both the Anomaly and Control integrations (see Section 2.3 (Figure 4(b)). Since the onset of the drift is slightly delayed in the Anomaly experiment (see Section 4.2), a significant cooling appears in the (Anomaly minus Control) response pattern, but this does not appear to represent a genuine climate change arising from the enhanced greenhouse forcing. Such a feature emphasises the need to eliminate climate drift in future experiments, particularly since the influence of the Southern Ocean cooling is extended beyond its immediate source region (i.e. the area of deep mixing south of 60 Deg S), by the action of horizontal advection and diffusion in the ocean. This is clearly illustrated at years 21-30 by the tongues of colder water extending north-westwards into the tropical Atlantic and Pacific Oceans, which can be identified with equatorward currents on the eastern flank of the main southern hemisphere mid-latitude ocean gyres in the two basins.

4.5 Mean Sea-Level Pressure (PMSL) Response

Figure 20(a) shows the PMSL response for DJF, averaged over the decade of doubling. The most interesting feature occurs in the northern hemisphere, where a distinctive large-scale structure is apparent at mid-latitudes, with reduced pressure over the continents and increases over the oceans. This pattern correlates well with the surface temperature response (Figure 16(a)), suggesting that the PMSL response essentially represents a monsoon circulation driven by the differential warming of the land relative to the sea. There is a reduction in pressure over the Arctic Ocean, in common with other simulations which produce diminished Arctic sea-ice cover (e.g. Wilson and Mitchell, 1987). Coupled with the increase in pressure to the south, this leads to enhanced westerly flow across the North Atlantic, with anomalous north-westerly flow across the UK and much of northern and western Europe. The increased westerlies coincide with an increase in the strength of the Atlantic storm track (not shown). In JJA (Figure 20(b)), PMSL is again lower over the continents, in both the northern and southern hemispheres. Whilst the northern hemisphere reductions are smaller than in DJF, they carry a greater statistical significance (Figure 21), due to the smaller natural variability in summer. The reduction in pressure over northern India and Pakistan is consistent with the increase in precipitation associated with the Asian summer monsoon (see Section 4.3). In the southern hemisphere, increases in pressure occur over the mid-latitude oceans, where the temperature response is a minimum. Since pressure is lower at high southern latitudes, the response shows increased westerly flow in the latitude band 45-60 Deg S.

An indication of the evolution of the PMSL response can be obtained by comparing Figure 20 with Figure 22, which shows the response for years 21-30. Interestingly, Figure 22(a) demonstrates that by years 21-30, the DJF mid-latitude pattern seen at years 66-75 has already developed. With the exception of years 41-50, when the increase in PMSL over the North Pacific is replaced by a reduction, this pattern, once established, is essentially persistent from decade to decade. Furthermore, the intensity of the land/sea pressure contrast does not increase very much after years 21-30. This probably reflects the fact that the accompanying land/sea contrast in the temperature response also becomes established at an early stage. For example, whilst the zonal-mean temperature response at (say) 50 Deg N grows by about 300% between years 21-30 and 66-75, the corresponding increase in land/sea temperature contrast is much smaller (around

50%). In JJA, the northern hemisphere pattern increases in strength up to years 31-40, and then declines towards the end of the experiment. Compared with years 66-75, the response at years 21-30 is therefore of similar intensity.

5. Summary

The UK Meteorological Office coupled ocean-atmosphere general circulation model (AOGCM) has been used to study the transient response of climate to a gradual (1% per year compound) increase in CO_2.

It is important to limit the development of systematic errors in the simulated Control (present-day) climate of the AOGCM, since such errors may distort the response to the imposed radiative perturbation. In order to achieve this, flux correction terms were added to the heat and water fluxes simulated at the atmosphere-ocean interface, in both the Control and Anomaly (increasing CO_2) integrations. This approach involves the implicit assumption that the flux corrections (or, equivalently, the model systematic errors) remain constant under conditions of climate change. Typically, the flux corrections are of similar magnitude to the simulated atmosphere-ocean fluxes themselves; at most locations the heat flux correction is anti-correlated with the simulated heat flux, suggesting that the model ocean achieves insufficient horizontal heat transport. With these terms in place, the climate drift of the AOGCM is severely reduced, though a gradual warming still occurs in the Southern Ocean during the Control experiment, associated with a change in the deep circulation, which eventually causes the disappearance of most of the Antarctic sea-ice.

The response of the AOGCM lies within the range implied by comparable modelling studies carried out elsewhere. At the time that CO_2 doubles (year 70), the global-mean surface warming is about 60% of the estimated equilibrium warming, the remaining 40% constituting a 'warming commitment' associated with the storage of heat in the ocean. There is a pronounced delay in the response over the first 2-3 decades. To some extent this arises from the experimental design: The (constant) rate of increase in radiative forcing is switched on discontinuously at the start of the experiment; however the coupled system needs time to build up a net atmosphere-ocean heat flux of sufficient magnitude to overcome the thermal inertia of the ocean, and cause a significant warming at the surface. Nevertheless, this 'cold start' effect (also observed in other experiments (e.g. Cubasch et. al, 1991)) is not sufficient to explain the delay entirely. In particular, calculations with a simple energy balance model (EBM), tuned to the AOGCM response, suggest that the climate sensitivity of the AOGCM increases with time, from around 1.0 degrees in the first 30 years of the experiment to approximately 2.8 degrees in the last 30 years. This is mainly due to the time dependence of the change in net downward shortwave radiation over the ocean, which does not vary linearly with the temperature response. Initially there is a reduction, tending to cool the ocean, and only in the second half of the experiment does a positive feedback set in. Further investigation is needed to clarify the reason for this behaviour. Over land, there is a much stronger positive shortwave feedback. This appears to be the main cause of the land/sea contrast in the surface warming, which is such that the land warming (2.8 degrees) is twice that of the ocean (1.3 degrees) at the time of doubling.

By forcing the EBM with the observed equivalent CO_2 forcing for 1765-1990, the AOGCM response was interpreted in terms of the observed temperature record. Whilst the ocean warming is reasonably consistent with observations, over land the warming substantially overestimates that observed during the 20th Century. However, the AOGCM does not include the negative radiative forcing arising from anthropogenically-produced tropospheric sulphate aerosol, which is thought partially to offset the enhanced greenhouse effect (Charlson et. al, 1991). Results obtained using the EBM suggest that according to current estimates, this forcing, which occurs predominantly over land, is (at least) large enough to account for the difference between the modelled and observed responses over land. More sophisticated studies are now needed to investigate this issue further.

In many respects, the geographical distribution of the transient response is similar to the equilibrium response; however, in common with the results of Manabe et. al (1991) and Cubasch et. al (1991), the surface warming is small in the Southern Ocean, and also in the North Atlantic Ocean, where the effective oceanic heat capacity is very large, due to deep convective mixing associated with sinking branches of the thermohaline circulation. In these regions, the ocean warms throughout the depth of the water column, whereas elsewhere the response is small below about 500 metres. In the North Atlantic, the strength of the thermohaline circulation decreases by about 25% by the time of CO_2 doubling, possibly due to freshening of the surface layers of the ocean arising from increased precipitation. As discussed by Manabe and Stouffer (1988), this is likely further to limit the surface warming, through reduced northward advection of warm sub-tropical water in the surface layers.

In addition to the features discussed above, the main characteristics of the transient response are an enhanced warming in the northern hemisphere at high latitudes, and over the mid-latitude continents, and a large interhemispheric asymmetry, the southern hemisphere response (influenced by the Southern Ocean) being generally much smaller. These elements all become clearly established by the end of the third decade, and essentially remain fixed thereafter, although the relative amplitude of the northern high-latitude warming increases in the second half of the experiment, once significant reductions in areal sea-ice cover begin to occur. In the Southern Ocean there is a significant cooling in the first 60 years, which is replaced by a small warming only in the last 15 years; however the detailed response in this region may have been influenced by climate drift in the Control integration (see above).

The seasonal variations in the surface temperature and precipitation changes are generally similar to those observed in studies of the equilibrium response. In the northern hemisphere, the high latitude amplification of the surface warming is much larger in winter than in summer, but the enhanced continental warming is present throughout the year, sustained by increased net solar radiation in summer, and by heat released from the high latitude ocean in winter. At middle and high latitudes, precipitation increases over the ocean in both hemispheres, consistent with enhanced poleward moisture transport in the warmer atmosphere; however in northern summer there are reductions in precipitation over large areas of the northern continents, associated with drying of the soil and reduced surface evaporation. In northern winter, the change in mean sea-level pressure shows a strong wavenumber 2 pattern, with increases over the ocean and reductions over land. This pattern, which appears to be linked to the land/sea contrast in the temperature response, develops early in the experiment, and is generally persistent from decade to decade.

Further work is needed to clarify the physical mechanisms underlying some of the results presented in this report. More generally, a number of urgent priorities for future experiments can be identified. The systematic errors in AOGCM simulations of present climate need to be reduced; particular emphasis should be placed on reducing the magnitude of the flux correction terms. Furthermore, the flux correction scheme should itself be improved, to prevent, if possible, secular climate drift of the kind observed in the Southern Ocean in the present experiment. The AOGCM transient response should be assessed against the observed climate record, to help establish the trustworthiness of the model's predictions of future climate. Notwithstanding the idealised approach employed in the present study, this requires an AOGCM experiment driven by the observed anthropogenic greenhouse forcing from the pre-industrial period to present day. (The need for such an experiment is illustrated, for example, by the apparent time-dependence of the climate sensitivity in the present experiment, which may, in practice, be a scenario-dependent feature). In addition, the radiative contribution of anthropogenic aerosol also needs to be included, once this can be quantified more precisely.

Appendix: Statistical Significance of Simulated Differences

In studies of the equilibrium response to a doubling of CO_2 (e.g. Wilson and Mitchell, 1987), Student's t-test is often used to examine the significance of the difference between N-year samples of the simulated Anomaly and Control climates. This is acceptable, subject to the limitations noted by Mitchell et. al (1987), provided there is no *a priori* reason to expect a change in natural variability between the two simulations. The respective interannual sample variances, s_a and s_c, can then be assumed to be equal within the limits of sampling fluctuation. However, in the present experiment, the correct *a priori* assumption is that $s_a > s_c$, since the Anomaly integration is expected to contain a systematic trend superposed on the natural variability, representing the progress of the transient response.

This inequality of variances can be accounted for using the Welch test, as discussed by Afifi and Azen (1979). If $\langle x_a \rangle$ and $\langle x_c \rangle$ represent N-year samples from the two integrations, the test statistic is given by $t_w = (\langle x_a \rangle - \langle x_c \rangle)/((s_a^2+s_c^2)/N)^{1/2}$, identical to the Student's t-test statistic. For large samples, the distribution of t_w approximately follows the Student's t distribution, but the approximate number of degrees of freedom, d, is given by $d = ((N-1)(s_a^2+s_c^2)^2)/(s_a^4+s_c^4)$, cf $d = 2(N-1)$ for Student's t-test. Since d may be non-integral, the significance level corresponding to t_w was established using linear interpolation of values given in standard tables of Student's t distribution.

Acknowledgements

This work was sponsored by the UK Department of the Environment. Thanks are due to Dr J F B Mitchell and to Dr P R Rowntree for useful comments and notes on aspects of the response, which have been incorporated in the discussion. I also wish to thank Dr D L Roberts, who provided much valuable help in setting up the coupled model for this experiment.

References

Afifi, A A, and S P Azen, 1979. Statistical Analysis-A Computer Oriented Approach. Academic Press.

Bryan, K, and M D Cox, 1972. An approximate equation of state for numerical models of ocean circulation. *J. Phys. Oceanogr.*,2,510-514.

Bryan, K, Manabe S, and M J Spelman, 1988. Interhemispheric asymmetry in the transient response of a coupled ocean-atmosphere model to a CO_2 forcing. *J. Phys. Oceanogr.*,18,851-867.

Charlson, R J, Langner, J, Rohde, H, Leovy, C B, and S G Warren, 1991. Perturbation of the northern hemisphere radiative balance by backscattering from anthropogenic sulfate aerosols. *Tellus*,43A-B,152-163.

Charlson, R J, Schwartz, S E, Hales, J M, Cess, R D, Coakley Jr., J A, Hansen, J E, and D J Hofmann, 1992. Climate forcing by anthropogenic aerosols. *Science*,255,423-430.

Cox, M D, 1984. A primitive equation, three dimensional model of the ocean. *GFDL Ocean Group Technical Report No. 1*. GFDL, Princeton.

Cubasch, U, Hasselmann, K, Hock, H, Maier-Reimer, E, Mikolajewicz, U, Santer, B D, and R Sausen, 1991. Time-dependent greenhouse warming computations with a coupled ocean-atmosphere model. *Max Planck Inst. Meteor. Report 67*, Hamburg.

Gordon, C, 1989. Tropical ocean-atmosphere interactions in a coupled model. *Phil. Trans. R. Soc. Lond.*,A 329,207-223.

Gregory, D, and P R Rowntree, 1990. A mass flux convection scheme with representation of cloud ensemble characteristics and stability dependent closure. *Mon. Wea. Rev.*,118,1483-1506.

Gill, A E, 1982. Atmosphere-Ocean Dynamics. Academic Press.

Hibler, W D, 1979. A dynamic-thermodynamic sea ice model. *J. Phys. Oceanogr.*,9,815-846.

Hoffert, M I, Calligari, A J, and C-T Hsieh, 1980. The role of deep sea heat storage in the secular response to climatic forcing. *J. Geophys. Res.*,85,6667-6679.

Ingram, W J, Wilson, C A, and J F B Mitchell, 1989. Modeling climate change: An assessment of sea-ice and surface albedo feedbacks. *J. Geophys. Res.*,94,8609-8622.

Intergovernmental Panel on Climate Change, 1990. Scientific Assessment of Climate Change, 366 pp., WMO-UNEP, Cambridge University Press, Cambridge, U.K..

IPCC Climate Change 1992. The Supplementary Report to the IPCC Scientific Assessment, 200 pp., WMO-UNEP, Cambridge University Press, Cambridge, U.K.

Jerlov, N G, 1968. Optical Oceanography. Elsevier, Amsterdam.

Jones, P D, 1988. Hemispheric surface air temperature variations:

recent trends and an update to 1987. *J. Climate*,1,654-660.

Kraus, E B, and J S Turner, 1967. A one dimensional model of the seasonal thermocline. Part II. *Tellus*,19, 98-105.

Levitus, S, 1982. Climatological Atlas of the World Ocean. *NOAA Professional Pap. 13*, National Oceanic and Atmospheric Administration, Rockville, Maryland.

Manabe, S, Bryan, K, and M J Spelman, 1990. Transient response of a global ocean-atmosphere model to a doubling of atmospheric carbon dioxide. *J. Phys. Oceanogr.*,20,722-749.

Manabe, S, and R J Stouffer, 1988. Two stable equilibria of a coupled ocean-atmosphere model. *J. Climate*,1,841-866.

Manabe, S, Spelman, M J, and R J Stouffer, 1992. Transient responses of a coupled ocean-atmosphere model to gradual changes of atmospheric CO_2. Part II: Seasonal response. *J. Climate*,5,105-126.

Manabe, S, Stouffer, R J, Spelman, M J, and K Bryan, 1991. Transient responses of a coupled-ocean atmosphere model to gradual changes of atmospheric CO_2. Part I: Annual mean response. *J. Climate*,4,785-818.

Mead, C T, 1988. Asymmetries of the oceanic thermohaline circulation and meridional heat transport. Ph.D Thesis, University of Southampton.

Mitchell, J F B, Wilson, C A, and W M Cunnington, 1987. On CO_2 climate sensitivity and model dependence of results. *Quart. J. Roy. Met. Soc.*,113,293-322.

Pacanowski, R C, and S G Philander, 1981. Parametrization of vertical mixing in numerical models of tropical oceans. *J. Phys. Oceanogr.*,11,1443-1451.

Palmer, T N, Shutts, G J, and R Swinbank, 1986. Alleviation of a systematic westerly bias in general circulation and numerical weather prediction models through an orographic gravity wave drag parametrization. *Quart. J. Roy. Met. Soc.*,112,1001-1039.

Paulson, C A, and J J Simpson, 1977. Irradiance measurements in the upper ocean. *J. Phys. Oceanogr.*,7,952-956.

Penner, J E, Dickinson, R E, and C A O'Neill, 1992. Effects of aerosol from biomass burning on the global radiation budget. *Science*,256,1432-1434.

Ramaswamy, V, Schwarzkopf, M D, and K P Shine, 1992. Radiative forcing of climate from halocarbon-induced global stratospheric ozone loss. *Nature*,355,810-812.

Raval, A, and V Ramanathan, 1989. Observational determination of the greenhouse effect. *Nature*,342,758-761.

Redi, M H, 1982. Oceanic isopycnal mixing by coordinate rotation. *J. Phys. Oceanogr.*,12,1154-1158.

Roberts, D L, and H Cattle, 1989. Simulation of sea-ice in a coupled ocean-atmosphere model. *Met O 20 DCTN85*, Meteorological Office, Bracknell.

Roeckner, E, Schlese, U, Biercamp, J, and P Loewe, 1987. Cloud optical depth feedbacks and climate modelling. *Nature*,329,138-140.

Sausen, R, Barthel K, and K Hasselmann, 1988. Coupled ocean-atmosphere models with flux correction. *Climate Dynamics*,2,145-163.

Schmitt, C, and D A Randall, 1991. Effects of surface temperature and clouds on the CO_2 forcing. *J. Geophys. Res.*,96,9159-9168.

Schneider, S H, and S L Thompson, 1981. Atmospheric CO_2 and climate: Importance of transient response. *J. Geophys. Res.*,86,3135-3147.

Semtner, A J, 1976. A model for the thermodynamic growth of sea ice in numerical investigations of climate. *J. Phys. Oceanogr.*,6,379-389.

Senior, C A, and J F B Mitchell, 1992. CO_2 and climate: The impact of cloud parameterization. *J. Climate*, To Appear.

Slingo, A (Editor), 1985. Handbook of the Meteorological Office 11-layer atmospheric general circulation model. Volume I: Model description. *Met O 20 DCTN 29*, Meteorological Office, Bracknell.

Slingo, A, and D W Pearson, 1987. A comparison of the impact of an envelope orography and of a parametrization of orographic gravity-wave drag on model simulations. *Quart. J. Roy. Met. Soc.*,113,847-870.

Slingo, A, Wilderspin, R C, and R N B Smith, 1988. The effect of improved physical parametrizations on simulations of cloudiness and the earth's radiation budget in the tropics. *J. Geophys. Res.*,94,2281-2301.

Smith, R N B, 1990. A scheme for predicting layer clouds and their water content in a general circulation model. *Quart. J. Roy. Met. Soc.*,116,435-460.

Warrilow, D A, and E Buckley, 1989. The impact of land surface processes on the moisture budget of a climate model. *Annales Geophysicae*,7,439-450.

Warrilow, D A, Sangster, A B, and A Slingo, 1986. Modelling of land surface processes and their influence on European climate. *Met O 20 DCTN 38*,Meteorological Office, Bracknell.

Washington, W M, and G A Meehl, 1989. Climate sensitivity due to increased CO_2: Experiments with a coupled atmosphere and ocean general circulation model. *Climate Dynamics*,4,1-38.

Wetherald, R T, and S Manabe, 1988. Cloud feedback processes in a general circulation model. *J. Atmos. Sci.*,45,1397-1415.

Wigley, T M L, Holt, T, and S C B Raper, 1991. STUGE (an Interactive Greenhouse Model): User's Manual, Climatic Research Unit, Norwich, U.K., 44pp.

Wigley, T M L, and S C B Raper, 1992. Implications for climate and sea level of revised IPCC emissions scenarios. *Nature*,357,293-300.

Wilson, C A, and J F B Mitchell, 1987. A doubled CO_2 climate sensitivity experiment with a global climate model including a simple ocean. *J. Geophys. Res.*,92,13315-13343.

Tables

Table 1

Ocean Model Layer Depths (m)

Model Layer	Thickness	Depth at mid-point
1	10.0	5.0
2	10.0	15.0
3	10.0	25.0
4	10.2	35.1
5	15.3	47.4
6	23.0	66.5
7	34.5	95.8
8	51.8	138.9
9	77.8	203.7
10	116.8	301.0
11	175.3	447.1
12	263.2	665.3
13	395.3	995.6
14	593.5	1490.0
15	891.1	2232.3
16	1236.2	3295.9
17	1586.0	4707.0

Table 2

Response of Coupled Ocean-Atmosphere Models at Time of CO_2 Doubling

Model	Surface Temperature Response (Deg C)	Equilibrium Response	Realised Fraction of Equilibrium Response
GFDL	2.3	4.0	58%
MPI	1.3	2.5	52%
UKMO	1.7	2.8	61%
IPCC (High)	2.2	4.5	49%
IPCC (Low)	1.1	1.5	73%

Table 3

Time Variation of Effective Oceanic Heat Capacity, c_o

Period	c_o ($10^9 Jm^{-2}K^{-1}$)
Years 1-15	1.33
Years 16-30	1.38
Years 31-45	2.82
Years 46-60	1.41
Years 61-75	1.66

Figure Captions

Figure 1. Schematic diagram of experimental design.

Figure 2. Time variation of normalised globally averaged ocean temperature (T) in the calibration experiment, at various levels. The ordinate represents $(T(t)-T_{init})/(T_{final}-T_{init})$, where T(t) denotes the 5-year mean centred on year t, T_{final} the mean over years 141-150, and T_{init} the observed annual-mean, representing the initial state.

Figure 3. Zonal-mean net heat flux from atmosphere to ocean, and heat flux correction, in W/m^2, averaged over last 10 years of calibration experiment.

Figure 4. Difference of annual-mean sea surface temperature from climatology, for: (a) Year 10 of a parallel Control integration without flux correction; (b) Years 66-75 of Control integration.

Figure 5. Response of annual-mean surface temperature to increasing CO_2 averaged over land, sea and globe.

Figure 6. Decadal mean changes in globally averaged surface temperature in various coupled ocean-atmosphere experiments (the NCAR curve is for sea temperatures only). Forcing scenarios vary from model to model. See text for further information.

Figure 7. Schematic diagram of a four-box globally averaged energy balance model, used to investigate the response of the AOGCM. ΔQ= Imposed radiative perturbation; ΔT= Temperature response; C= Effective heat capacity; λ= Radiative feedback parameter; k= Energy transfer coefficient; F= Net energy flux; $f_{o(l)}$= Fraction of surface occupied by ocean (land).

Figure 8. Response of energy balance model when calibrated using fluxes and temperature changes simulated by the AOGCM over years 46-75, compared to corresponding (5-year mean) response of the AOGCM itself. Land surface, ocean surface and tropospheric averages are shown.

Figure 9 Five-year mean surface shortwave feedback (Wm^{-2}), measured as the change in net downward shortwave radiation minus the contribution arising directly from increased CO_2, averaged over (a) ocean points; (b) land points.

Figure 10. Time dependence of climate sensitivity of AOGCM. The curves show the predicted equilibrium surface warming in response to a doubling of CO_2, averaged over land, ocean and the whole globe, obtained by calibrating the energy balance model using time-mean fluxes and temperature changes from overlapping 30-year periods (centred on points marked x) of the AOGCM experiment.

Figure 11. Comparison of observed and modelled annual-mean surface temperature records, averaged over ocean (top panel) and land (bottom panel). (i) Observed (_____); (ii)

Energy balance model, calibrated using AOGCM fluxes and temperature changes from years 46-75, and driven using observed equivalent CO_2 radiative forcing from 1765-1990 (-------); (iii) As (ii) but using forcing-dependent feedback parameters for surface shortwave radiation, chosen to match the behaviour of the AOGCM (xxxxxxx).

Figure 12(a). As Figure 11 except: (iii) As (ii) with radiative forcing amended to include estimated effect of anthropogenically produced tropospheric sulphate aerosol (xxxxxxx).

Figure 12(b). As Figure 12(a), except that aerosol forcing is reduced by 50% in (iii).

Figure 13. Decadal mean response of surface temperature to a doubling of CO_2. (a) Equilibrium response of coupled 'slab' ocean-atmosphere model (see text); (b) Transient response of AOGCM averaged over years 66-75. Contour interval 1 deg C. Increases over 4 deg C heavily stippled, reductions lightly stippled.

Figure 14. Latitude-depth distribution of the zonal-mean ocean temperature response, averaged over years 66-75. Contour interval 0.2 deg C, reductions stippled.

Figure 15. Latitude-depth distribution of the streamfunction of the meridional circulation in the global ocean, averaged over years 66-75. (a) Control experiment; (b) Anomaly experiment. Units are Sverdrups (i.e. 10^6 m^3s^{-1}), positive values stippled.

Figure 16. Seasonal response of surface temperature, averaged over years 66-75. (a) Mean over December, January and February; (b) Mean over June, July and August. Contour interval 1 deg C. Increases over 4 deg C heavily stippled, reductions lightly stippled.

Figure 17. As Figure 16 for total precipitation. Contours plotted are 0,+ or - 1,2,5 mm/day, reductions stippled.

Figure 18. Decadal mean response of surface temperature for (a) Years 21-30, (b) Years 41-50. Contour interval 1 deg C. Increases over 4 deg C heavily stippled, reductions lightly stippled.

Figure 19. Statistical significance of the surface temperature response for years 21-30, according to a two-tailed Welch test. 5% and 1% significance levels contoured, with changes significant at the 5% level stippled, light for decreases, dark for increases.

Figure 20. Seasonal response of mean sea-level pressure, averaged over years 66-75. (a) Mean over December, January and February; (b) Mean over June, July and August. Contour interval 1mb, reductions stippled.

Figure 21. Statistical significance of the mean sea-level pressure changes for years 66-75 shown in Figure 20, according to a two-tailed Welch test, for (a) December, January and February; (b) June, July and August. 5% and 1% significance levels contoured, with changes significant

at the 5% level stippled, light for decreases, dark for increases.

Figure 22. As Figure 20, for years 21-30.

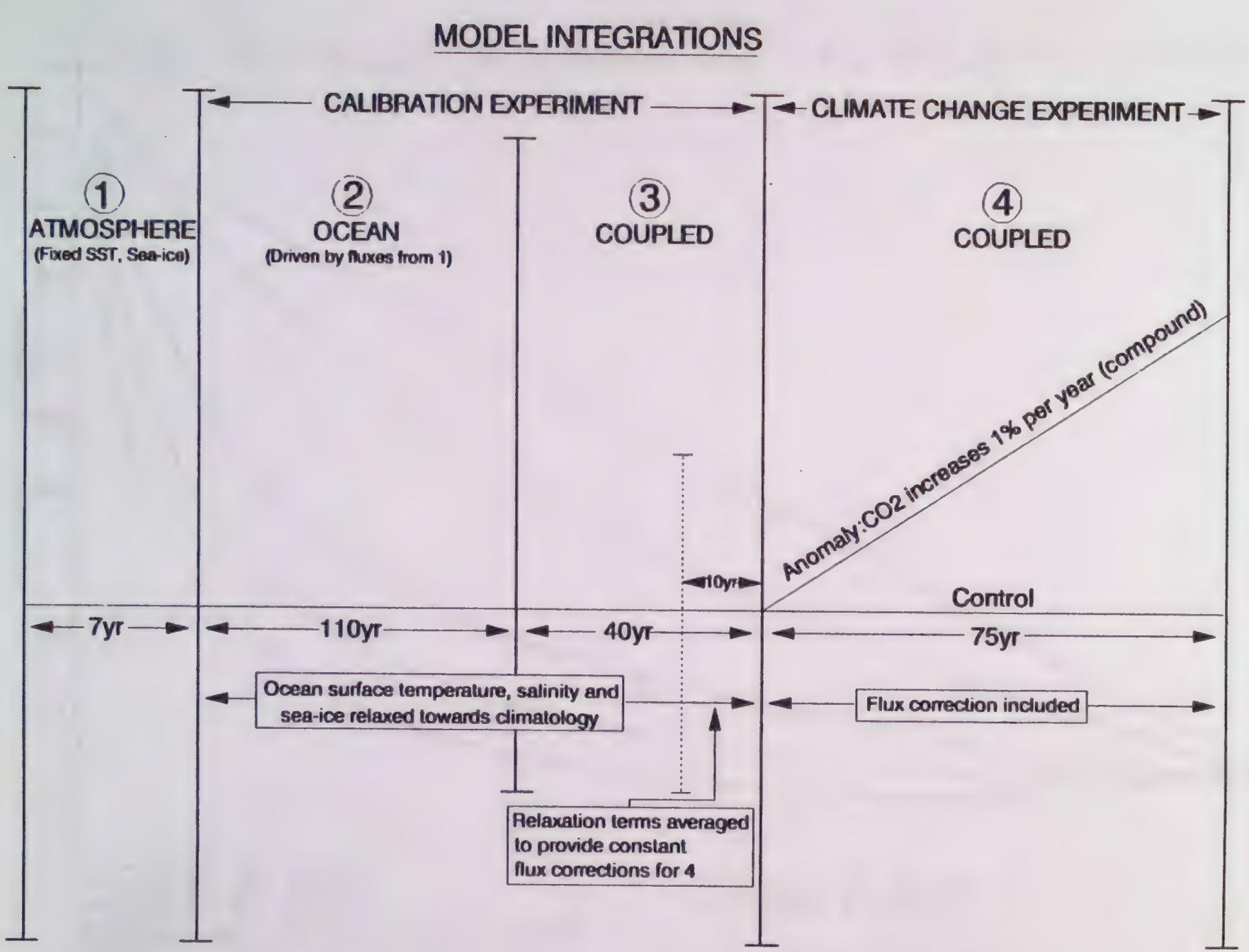
MODEL INTEGRATIONS
CALIBRATION EXPERIMENT
CLIMATE CHANGE EXPERIMENT
1
ATMOSPHERE
(Fixed SST, Sea-ice)
2
OCEAN
(Driven by fluxes from 1)
3
COUPLED
4
COUPLED
Anomaly:CO2 increases 1% per year (compound)
10yr
Control
7yr
110yr
40yr
75yr
Ocean surface temperature, salinity and sea-ice relaxed towards climatology
Flux correction included
Relaxation terms averaged to provide constant flux corrections for 4

Figure 1

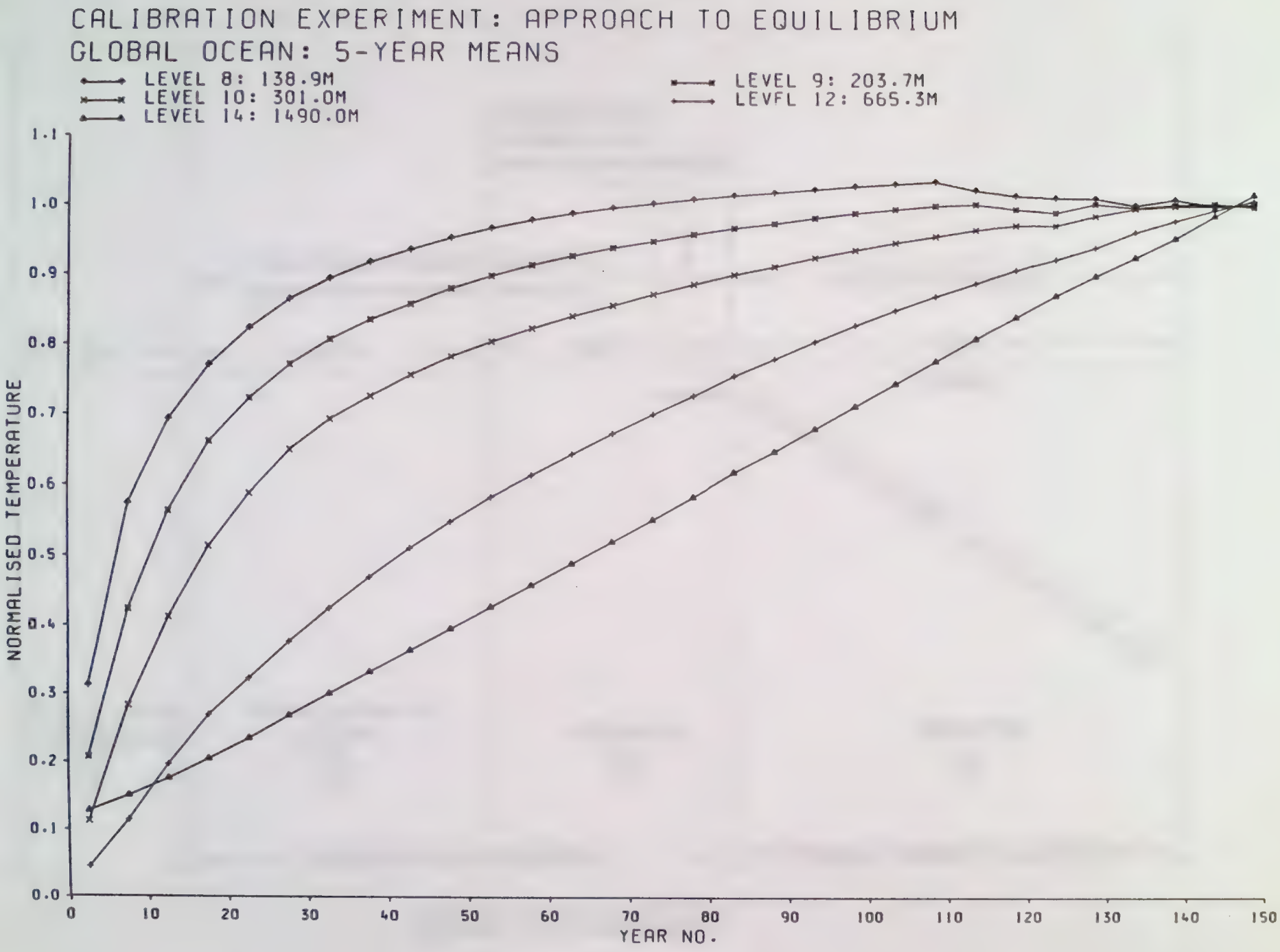
CALIBRATION EXPERIMENT: APPROACH TO EQUILIBRIUM
GLOBAL OCEAN: 5-YEAR MEANS
LEVEL 8: 138.9M
LEVEL 9: 203.7M
LEVEL 10: 301.0M
LEVEL 12: 665.3M
LEVEL 14: 1490.0M
NORMALISED TEMPERATURE
1.1
1.0
0.9
0.8
0.7
0.6
0.5
0.4
0.3
0.2
0.1
0.0
0
10
20
30
40
50
60
70
80
90
100
110
120
130
140
150
YEAR NO.

Figure 2

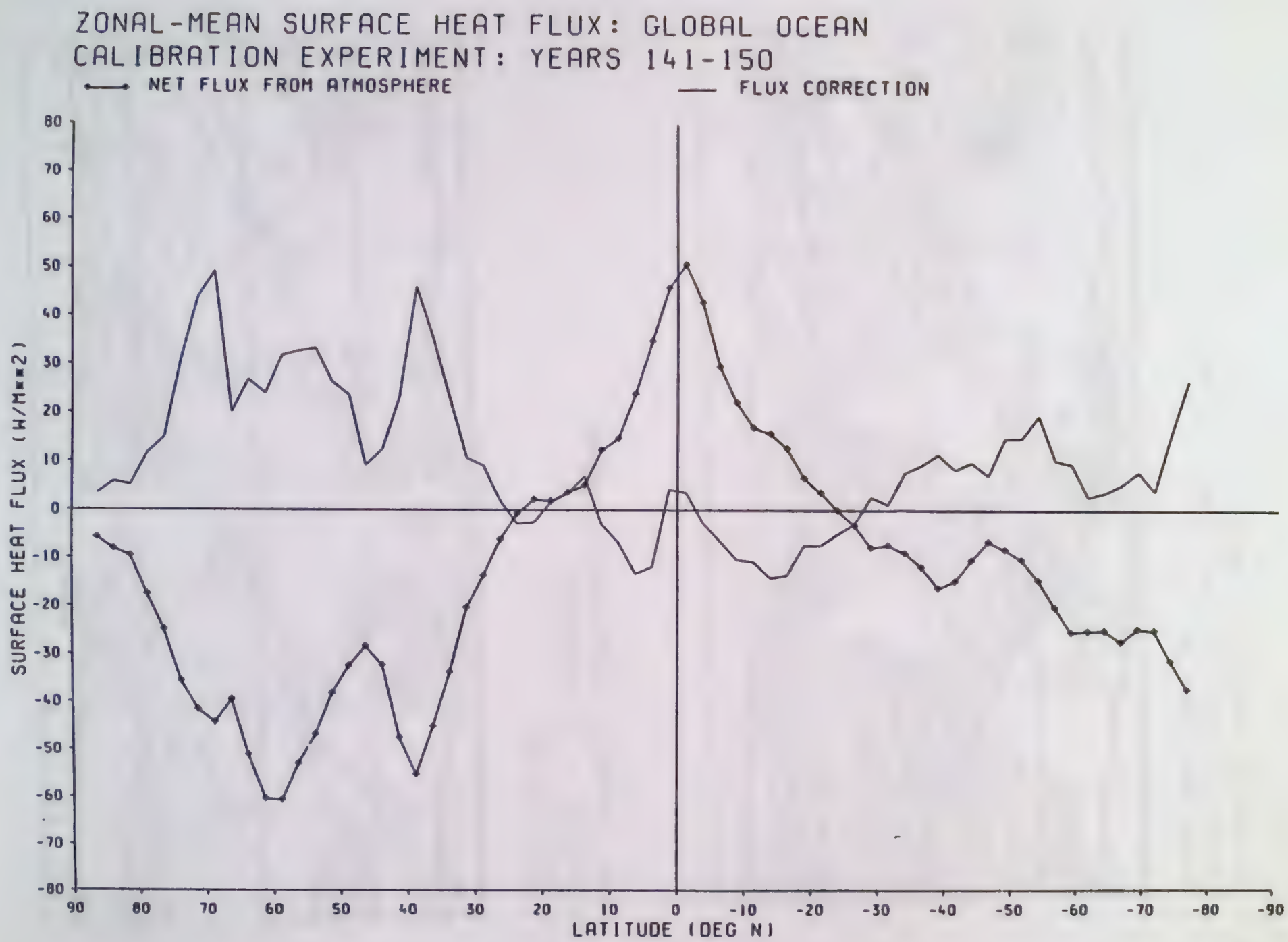
ZONAL-MEAN SURFACE HEAT FLUX: GLOBAL OCEAN
CALIBRATION EXPERIMENT: YEARS 141-150
NET FLUX FROM ATMOSPHERE
FLUX CORRECTION
SURFACE HEAT FLUX (W/M**2)
80
70
60
50
40
30
20
10
0
-10
-20
-30
-40
-50
-60
-70
-80
90 80 70 60 50 40 30 20 10 0 -10 -20 -30 -40 -50 -60 -70 -80 -90
LATITUDE (DEG N)

Figure 3

(a) SEA SURFACE TEMPERATURE (DEG C)
CONTROL (WITHOUT FLUX CORRECTION) - CLIMATOLOGY
ANNUAL MEAN: YEAR 10

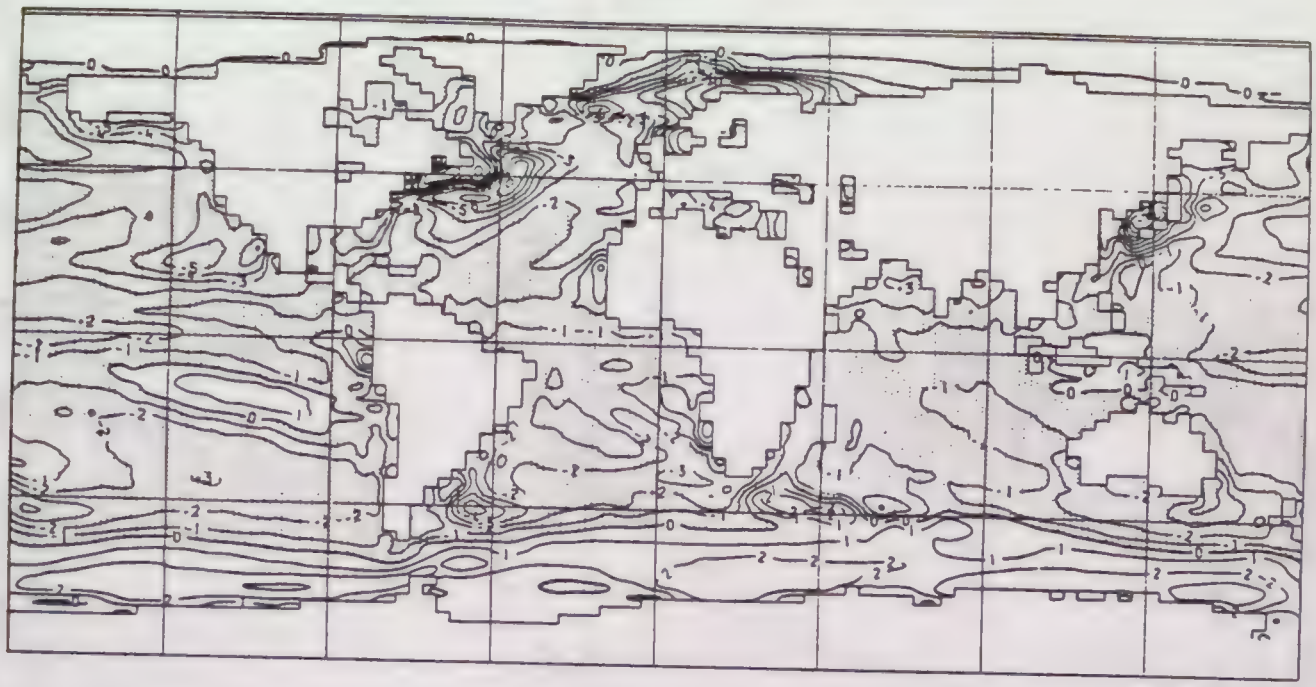

(b) SEA SURFACE TEMPERATURE (DEG C)
CONTROL - CLIMATOLOGY
YEARS 66-75

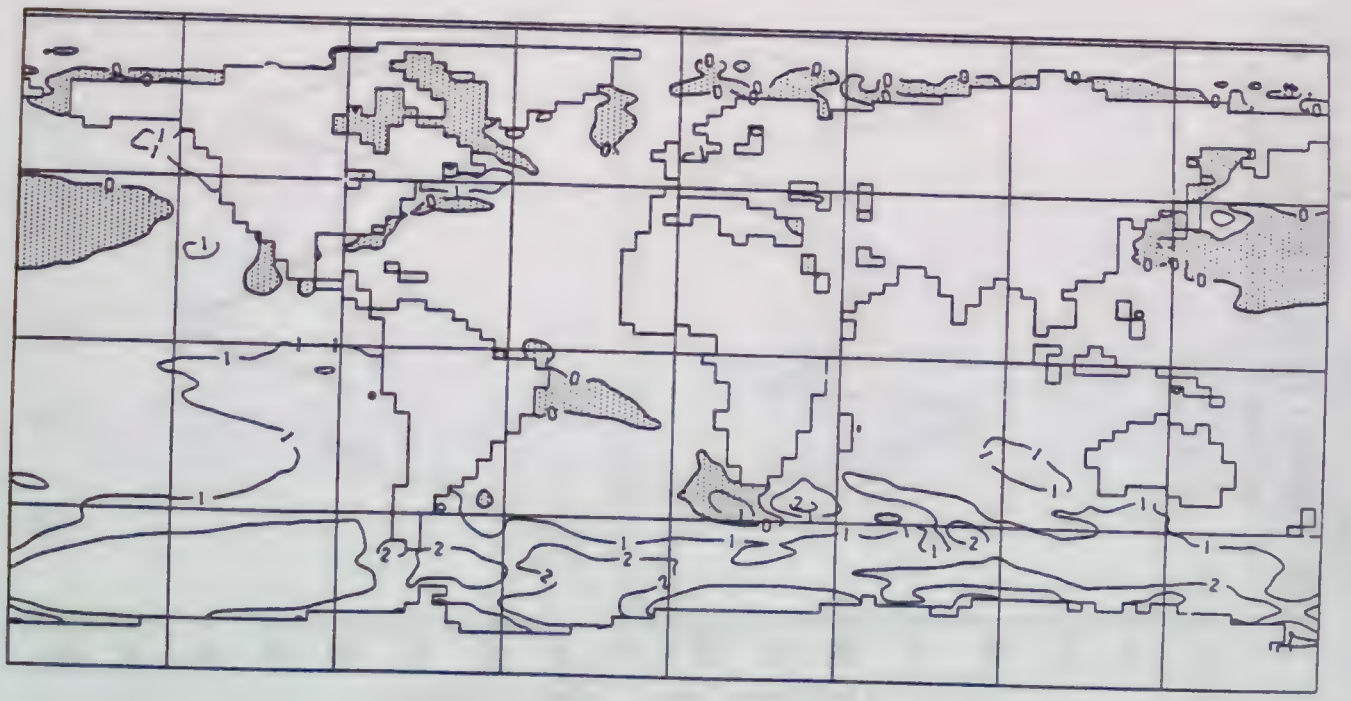

Figure 4

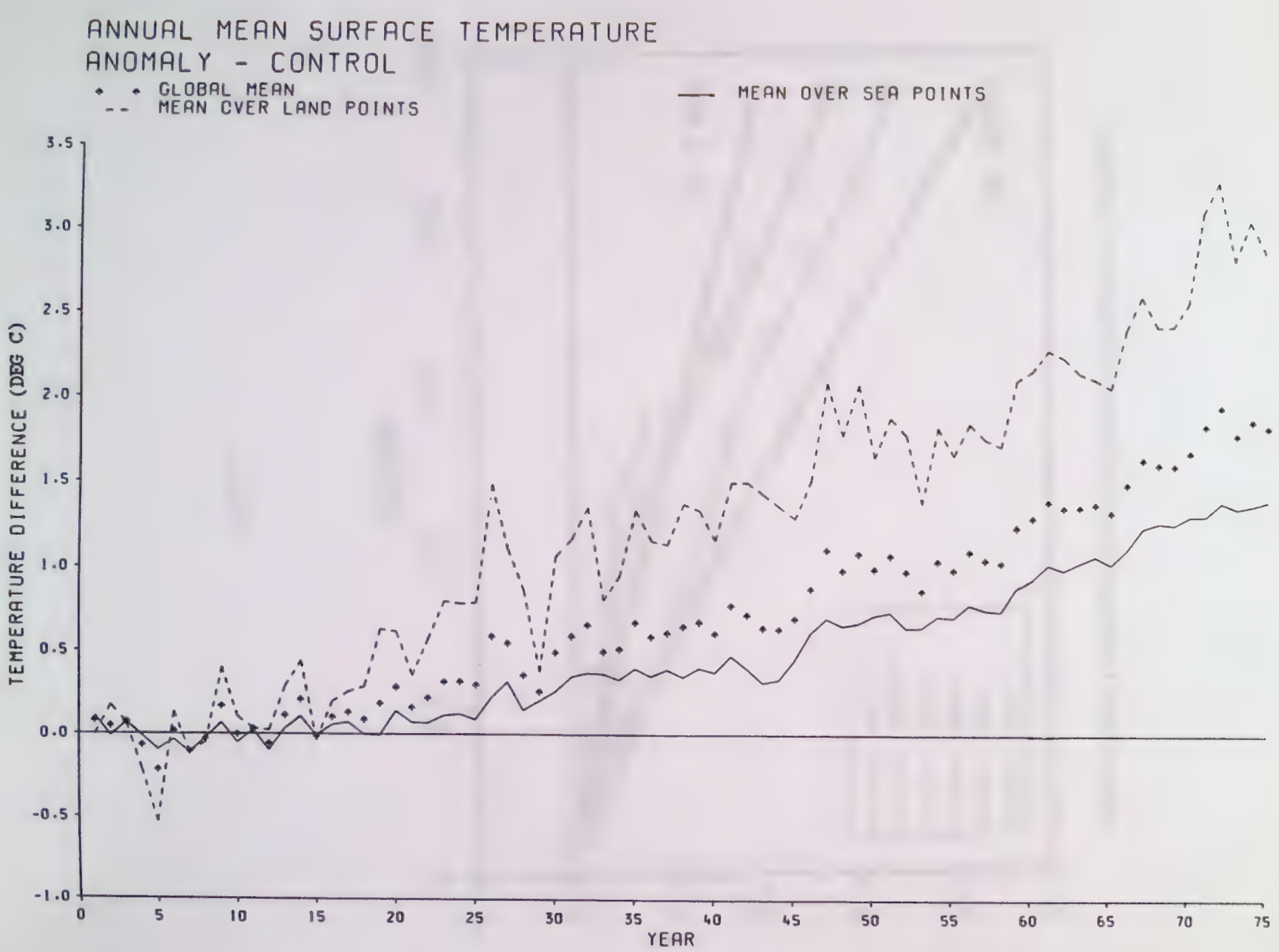
ANNUAL MEAN SURFACE TEMPERATURE
ANOMALY - CONTROL
GLOBAL MEAN
MEAN OVER LAND POINTS
MEAN OVER SEA POINTS
TEMPERATURE DIFFERENCE (DEG C)
3.5
3.0
2.5
2.0
1.5
1.0
0.5
0.0
-0.5
-1.0
0
5
10
15
20
25
30
35
40
45
50
55
60
65
70
75
YEAR

Figure 5

COUPLED OCEAN-ATMOSPHERE MODEL SIMULATIONS OF TRANSIENT RESPONSE

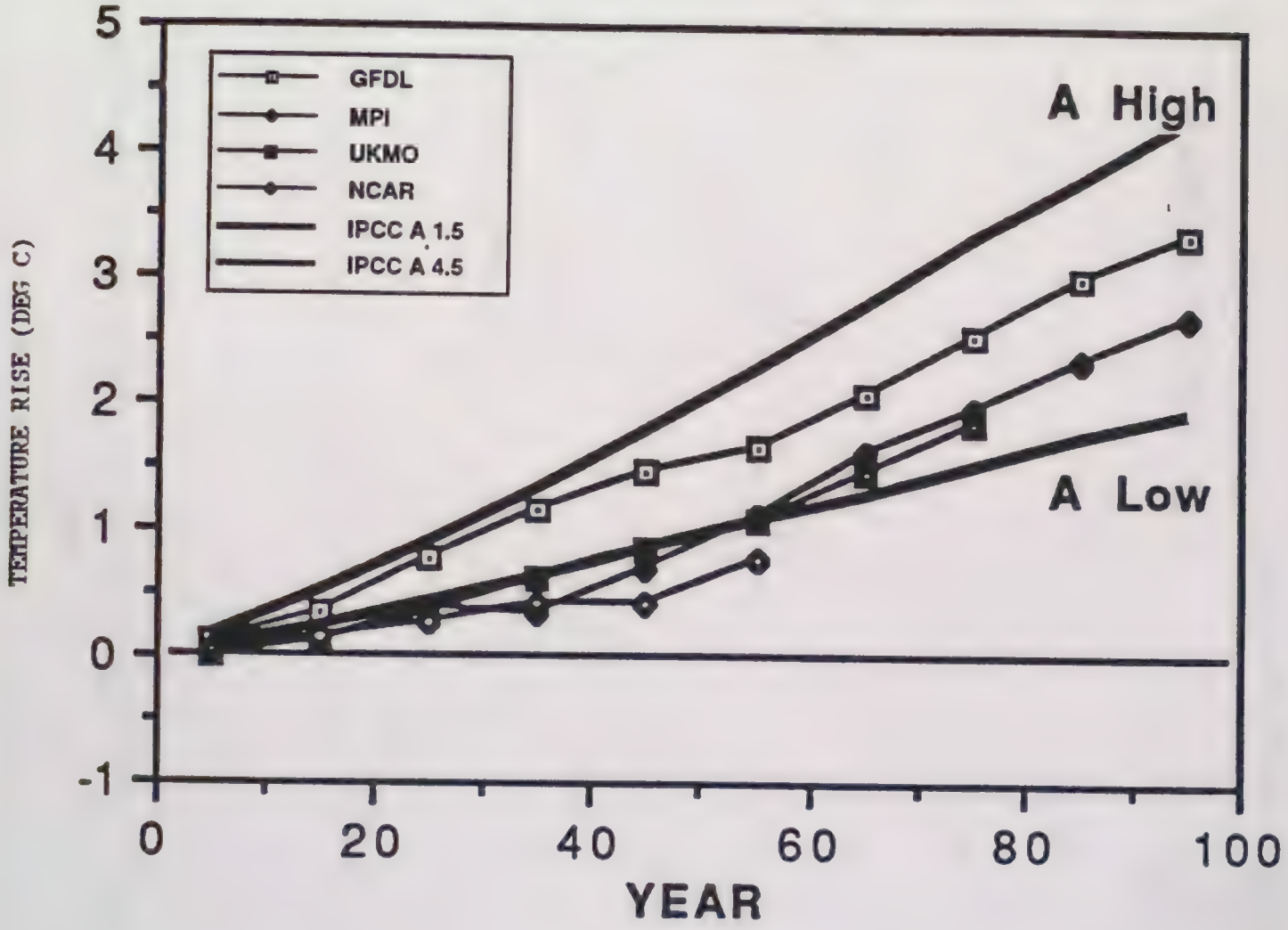

Figure 6

ENERGY BALANCE MODEL

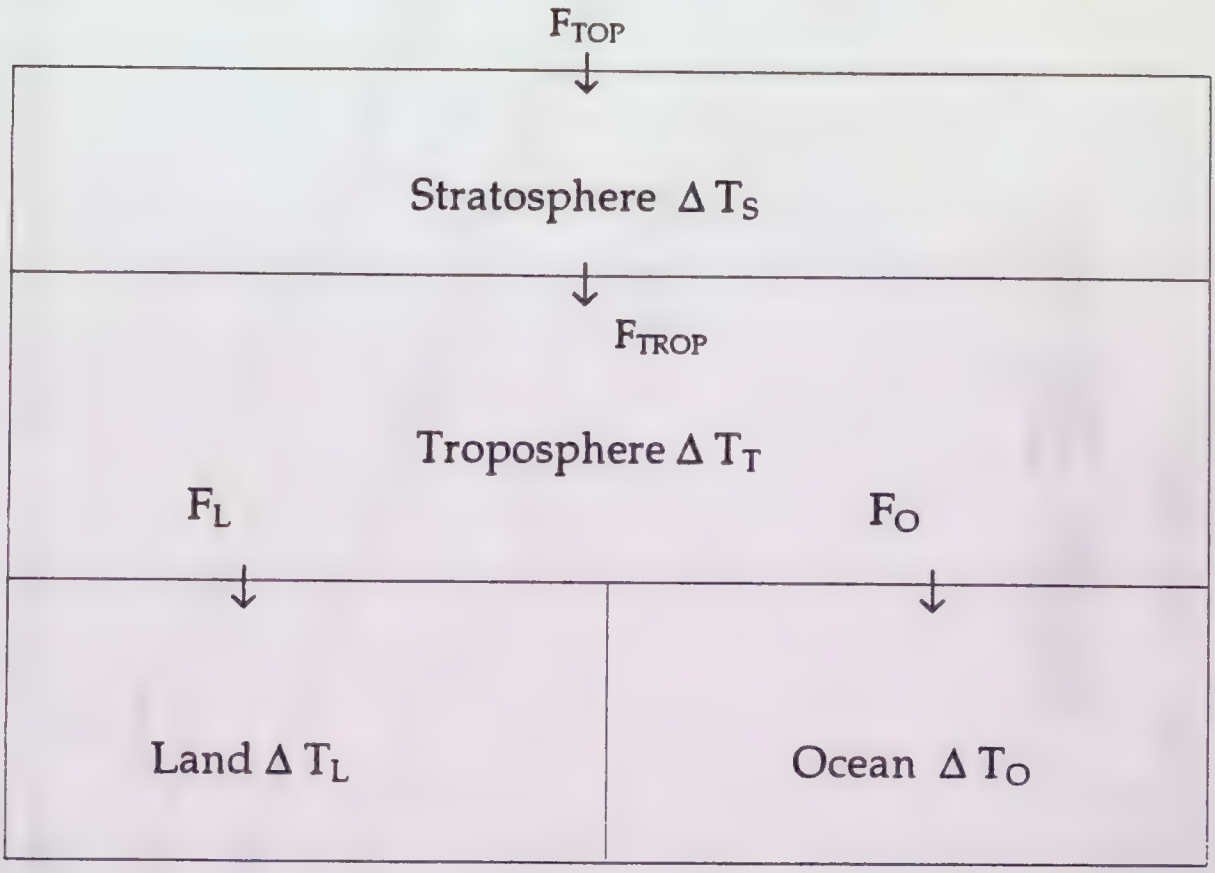

Equations

Ocean : $$C_O \frac{\partial(\Delta T_O)}{\partial t} = \Delta Q_O - \lambda_O \Delta T_O + k_O(\Delta T_T - \Delta T_O)$$

Land : $$C_L \frac{\partial(\Delta T_L)}{\partial t} = \Delta Q_L - \lambda_L \Delta T_L + k_L(\Delta T_T - \Delta T_L)$$

Troposphere : $$C_T \frac{\partial(\Delta T_T)}{\partial t} = \Delta Q_T - \lambda_T \Delta T_T - f_L k_L(\Delta T_T - \Delta T_L) - f_O k_O(\Delta T_T - \Delta T_O) + k_S(\Delta T_S - \Delta T_T)$$

Stratosphere : $$C_S \frac{\partial(\Delta T_S)}{\partial t} = \Delta Q_S - \lambda_S \Delta T_S - k_S(\Delta T_S - \Delta T_T)$$

Figure 7

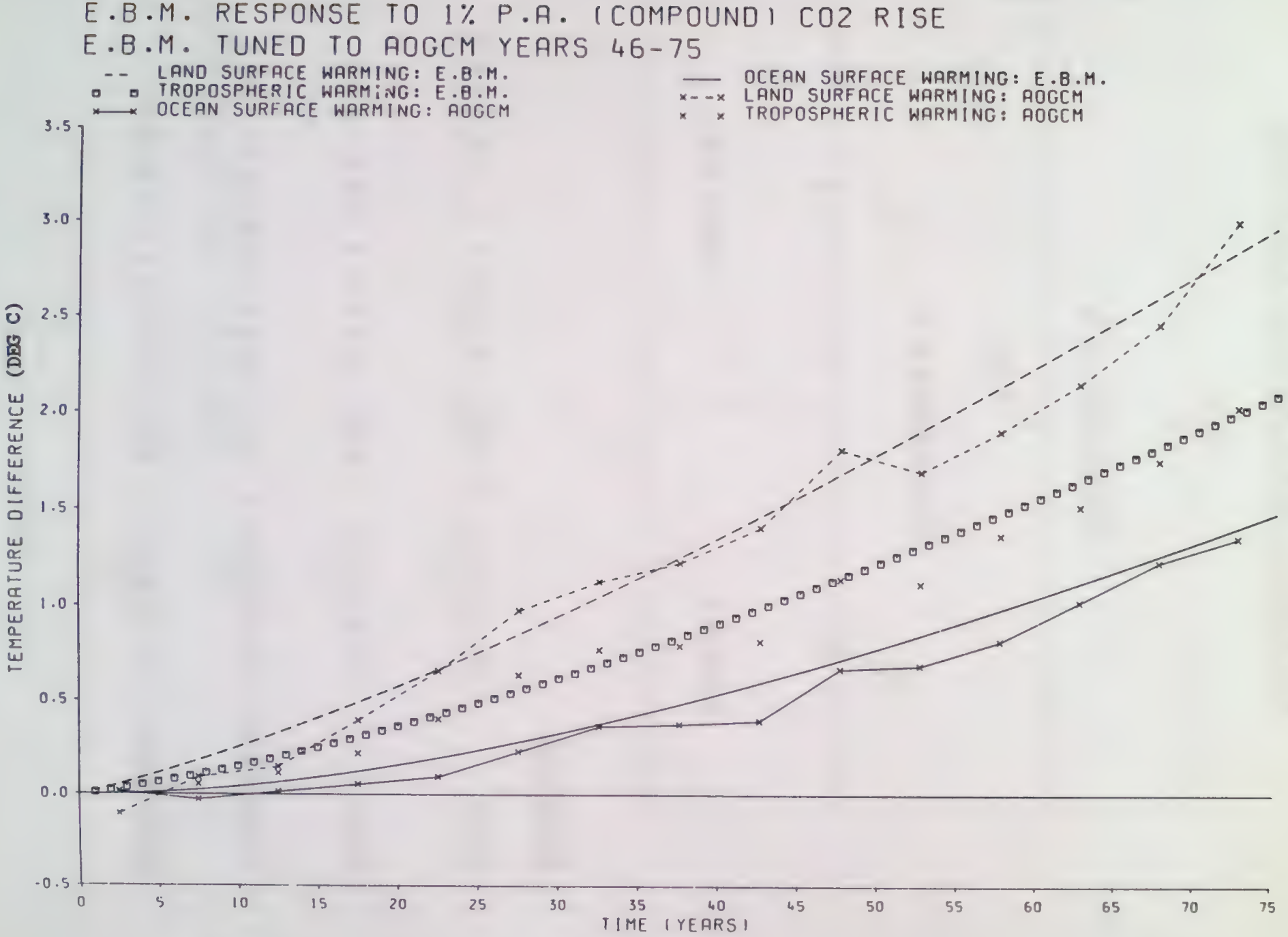
E.B.M. RESPONSE TO 1% P.A. (COMPOUND) CO2 RISE
E.B.M. TUNED TO AOGCM YEARS 46-75
LAND SURFACE WARMING: E.B.M.
TROPOSPHERIC WARMING: E.B.M.
OCEAN SURFACE WARMING: AOGCM
OCEAN SURFACE WARMING: E.B.M.
LAND SURFACE WARMING: AOGCM
TROPOSPHERIC WARMING: AOGCM
TEMPERATURE DIFFERENCE (DEG C)
TIME (YEARS)
3.5
3.0
2.5
2.0
1.5
1.0
0.5
0.0
-0.5
0
5
10
15
20
25
30
35
40
45
50
55
60
65
70
75

Figure 8

(a)

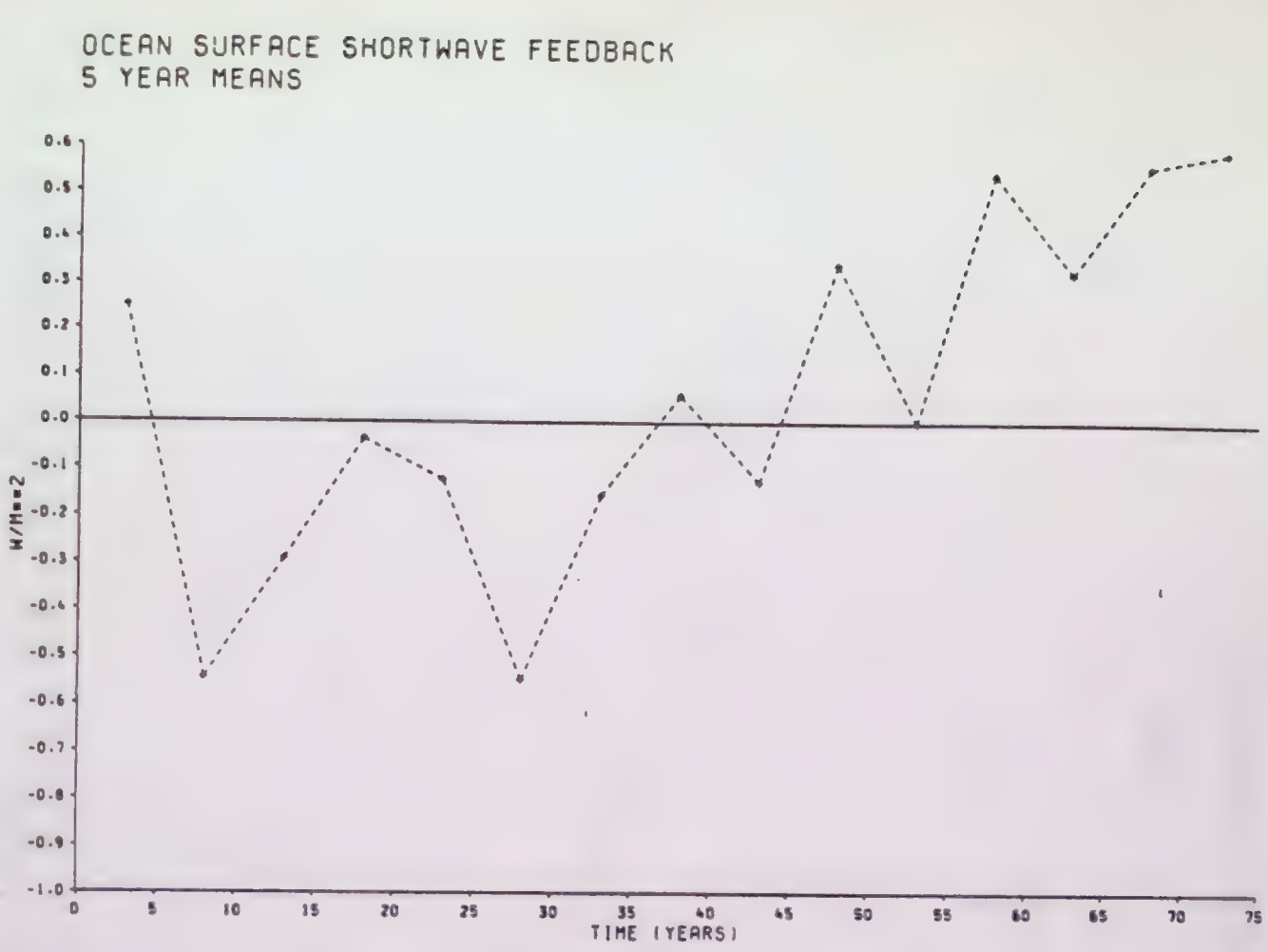
OCEAN SURFACE SHORTWAVE FEEDBACK
5 YEAR MEANS
W/M**2
TIME (YEARS)

(b)

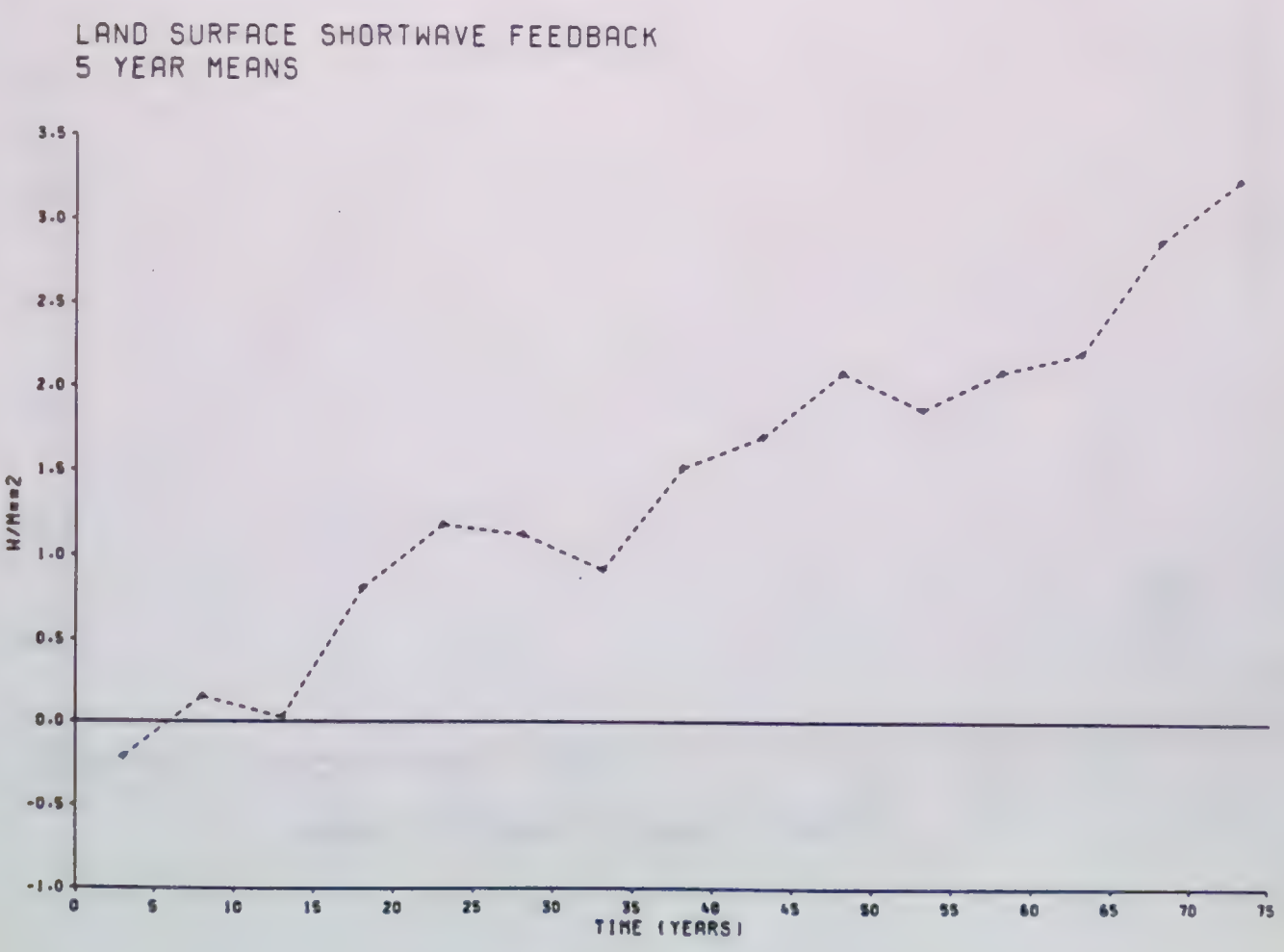
LAND SURFACE SHORTWAVE FEEDBACK
5 YEAR MEANS
W/M**2
TIME (YEARS)

Figure 9

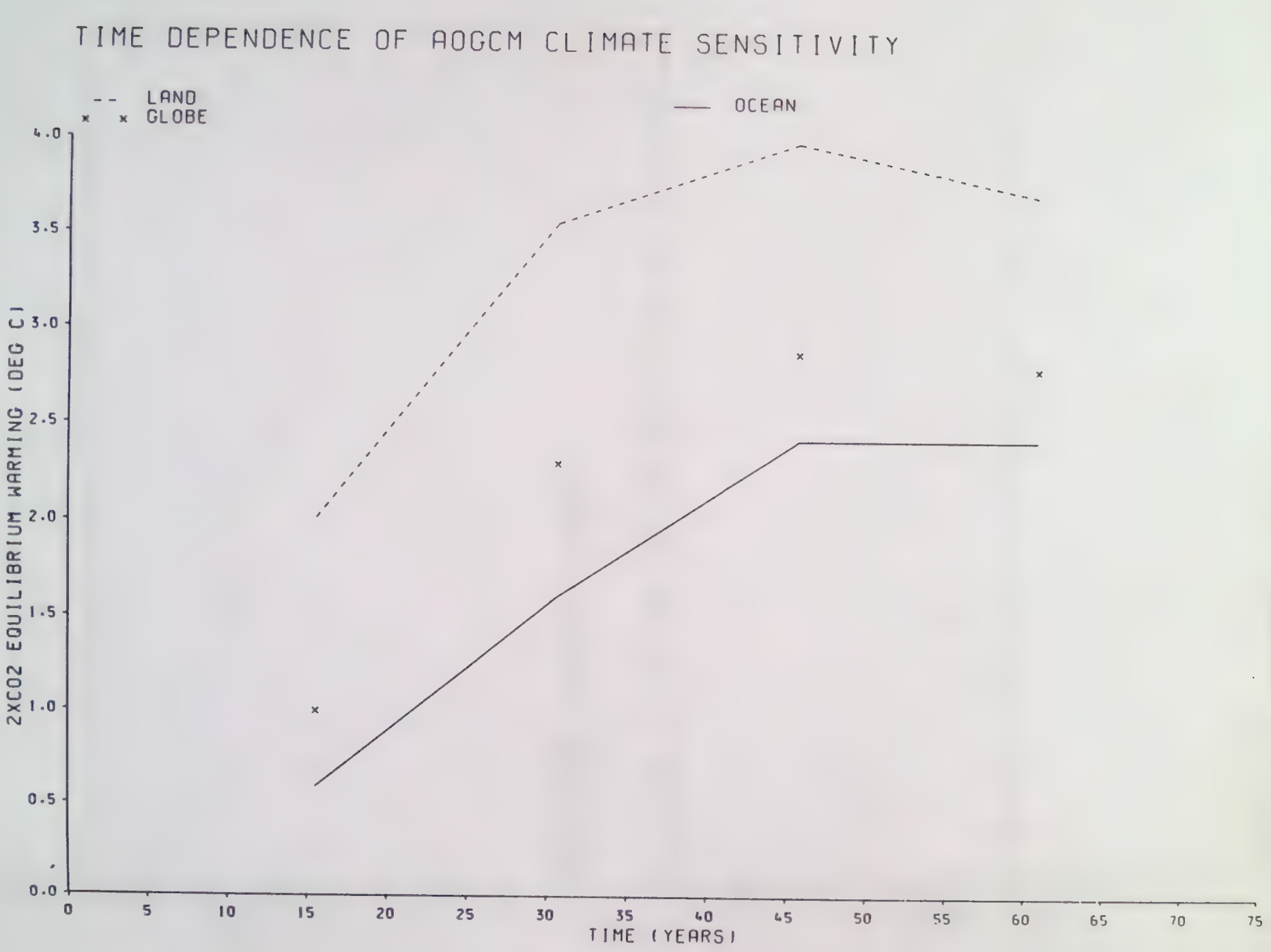
TIME DEPENDENCE OF AOGCM CLIMATE SENSITIVITY
LAND
GLOBE
OCEAN
2XCO2 EQUILIBRIUM WARMING (DEG C)
4.0
3.5
3.0
2.5
2.0
1.5
1.0
0.5
0.0
0
5
10
15
20
25
30
35
40
45
50
55
60
65
70
75
TIME (YEARS)

Figure 10

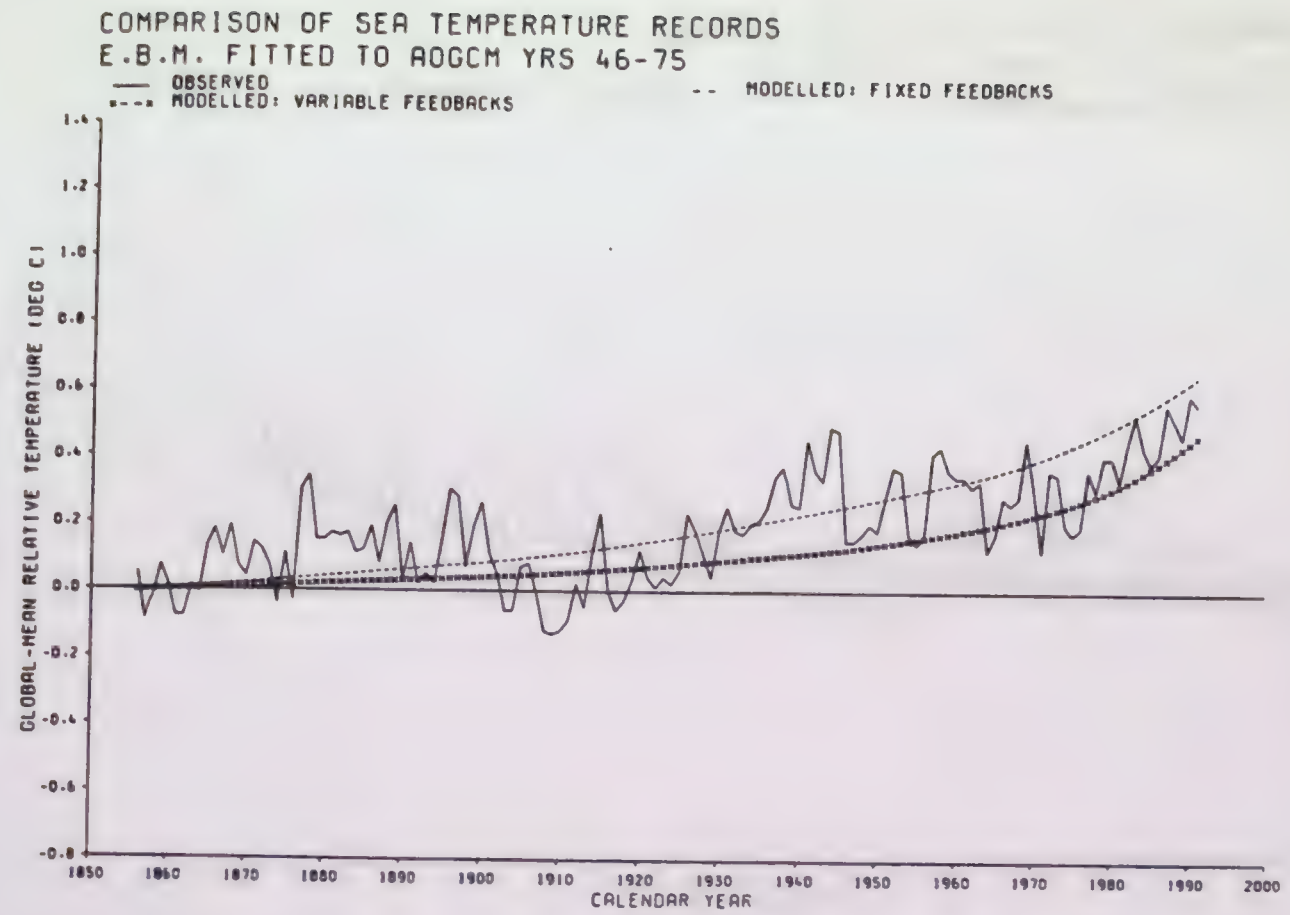
COMPARISON OF SEA TEMPERATURE RECORDS
E.B.M. FITTED TO AOGCM YRS 46-75
OBSERVED
MODELLED: VARIABLE FEEDBACKS
MODELLED: FIXED FEEDBACKS
GLOBAL-MEAN RELATIVE TEMPERATURE (DEG C)
1.4
1.2
1.0
0.8
0.6
0.4
0.2
0.0
-0.2
-0.4
-0.6
-0.8
1850
1860
1870
1880
1890
1900
1910
1920
1930
1940
1950
1960
1970
1980
1990
2000
CALENDAR YEAR

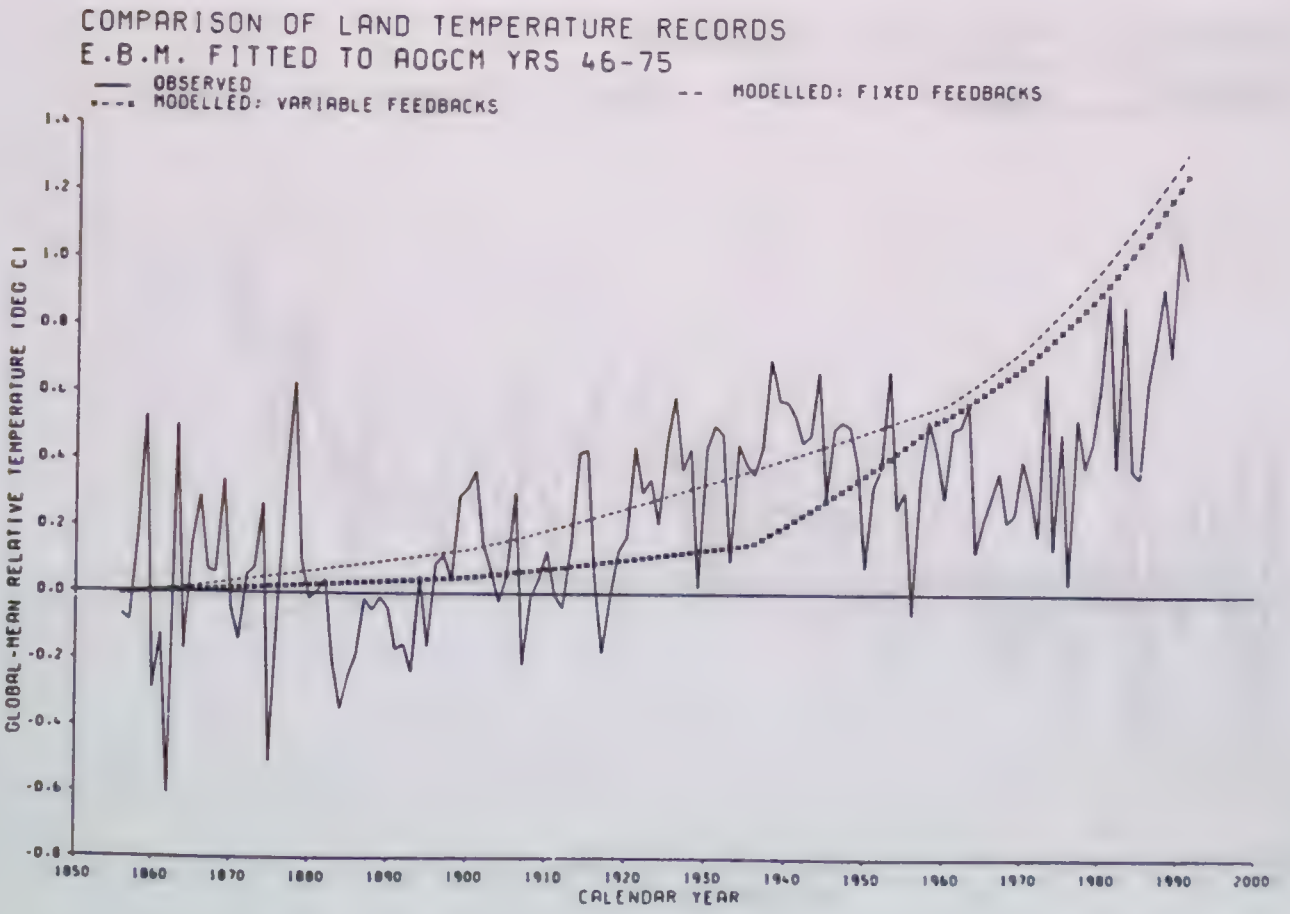
COMPARISON OF LAND TEMPERATURE RECORDS
E.B.M. FITTED TO AOGCM YRS 46-75
OBSERVED
MODELLED: VARIABLE FEEDBACKS
MODELLED: FIXED FEEDBACKS
GLOBAL-MEAN RELATIVE TEMPERATURE (DEG C)
1.4
1.2
1.0
0.8
0.6
0.4
0.2
0.0
-0.2
-0.4
-0.6
-0.8
1850
1860
1870
1880
1890
1900
1910
1920
1930
1940
1950
1960
1970
1980
1990
2000
CALENDAR YEAR

Figure 11

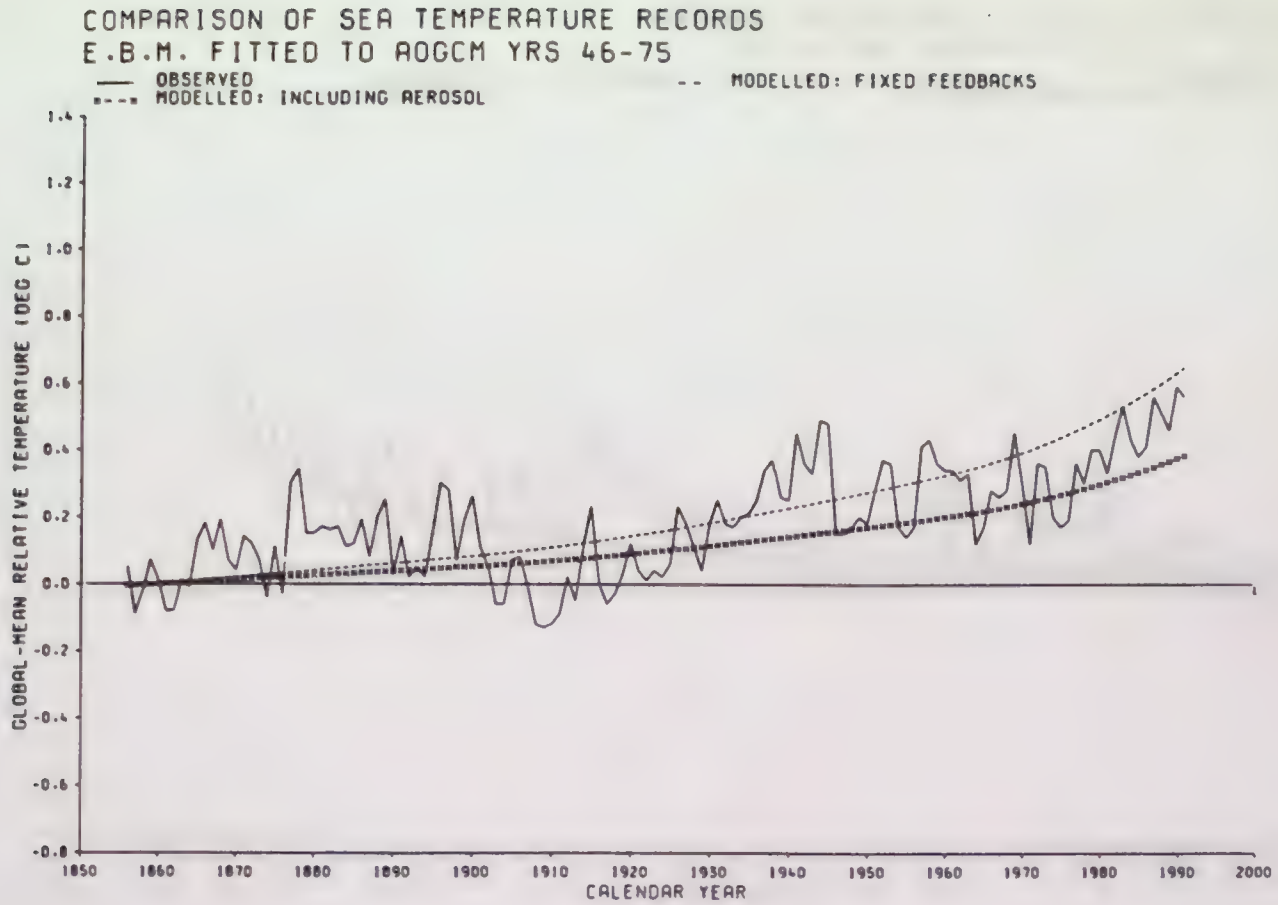
COMPARISON OF SEA TEMPERATURE RECORDS
E.B.M. FITTED TO AOGCM YRS 46-75
OBSERVED
MODELLED: INCLUDING AEROSOL
MODELLED: FIXED FEEDBACKS
GLOBAL-MEAN RELATIVE TEMPERATURE (DEG C)
CALENDAR YEAR

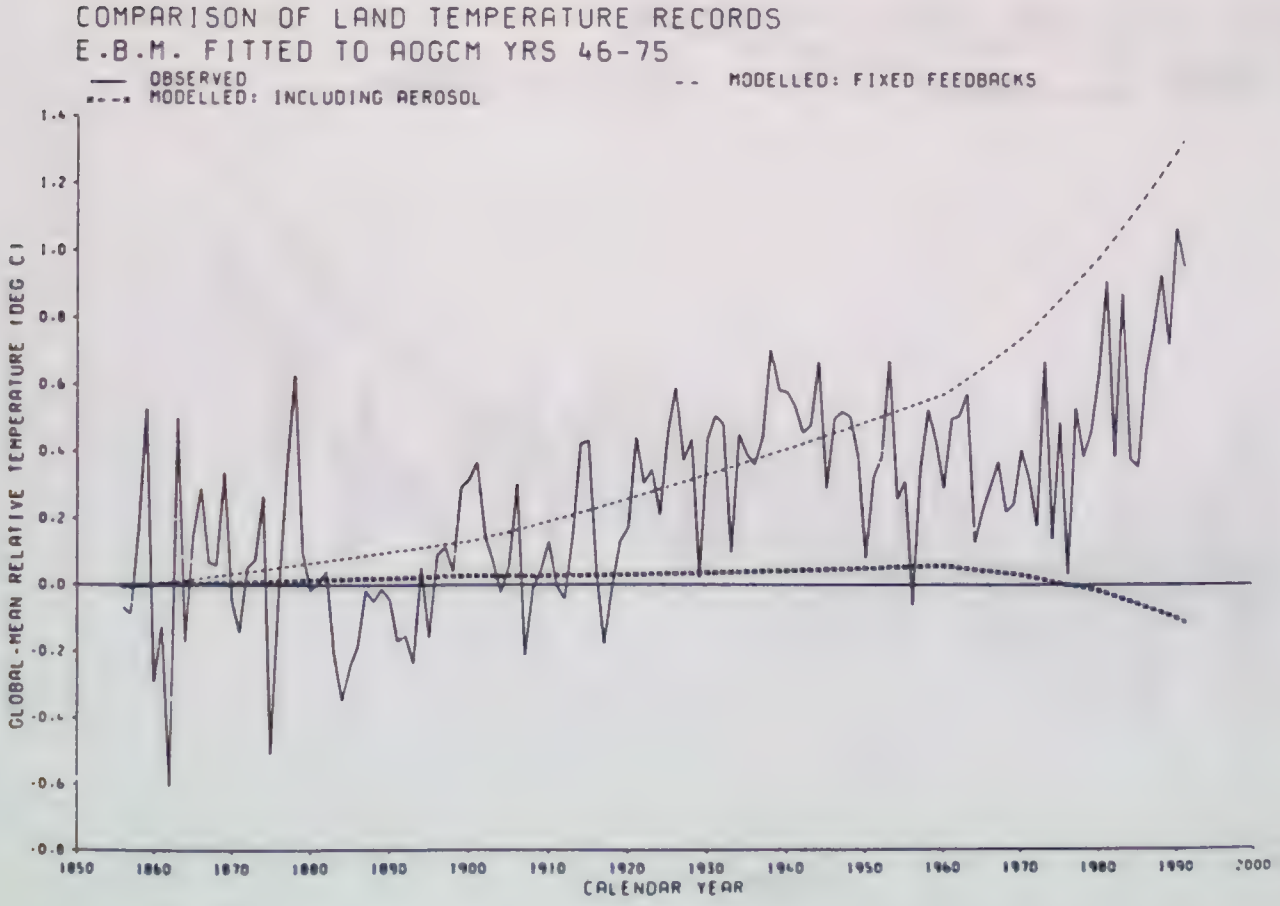
COMPARISON OF LAND TEMPERATURE RECORDS
E.B.M. FITTED TO AOGCM YRS 46-75
OBSERVED
MODELLED: INCLUDING AEROSOL
MODELLED: FIXED FEEDBACKS
GLOBAL-MEAN RELATIVE TEMPERATURE (DEG C)
CALENDAR YEAR

Figure 12(a)

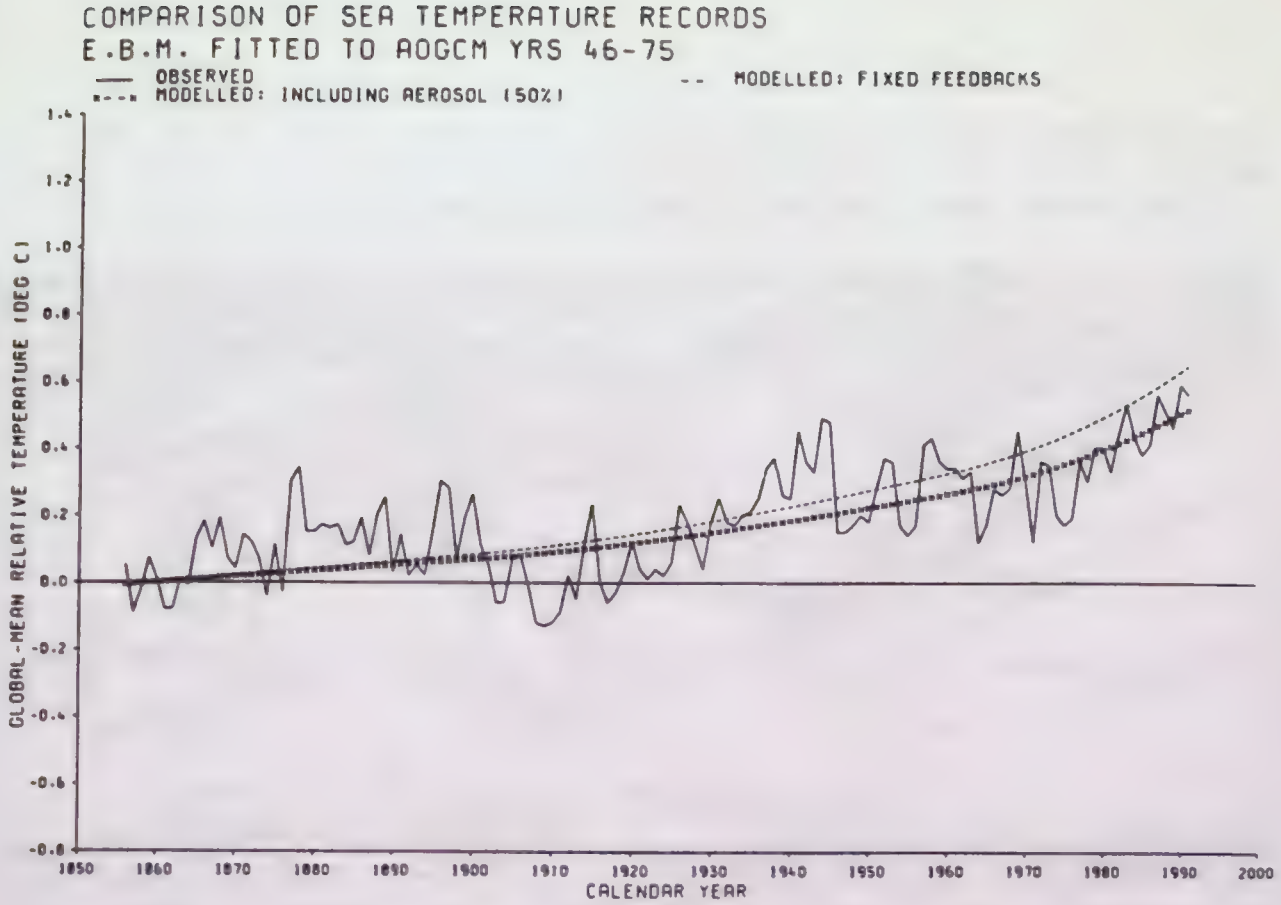
COMPARISON OF SEA TEMPERATURE RECORDS
E.B.M. FITTED TO AOGCM YRS 46-75
OBSERVED
MODELLED: INCLUDING AEROSOL (50%)
MODELLED: FIXED FEEDBACKS
GLOBAL-MEAN RELATIVE TEMPERATURE (DEG C)
1.4
1.2
1.0
0.8
0.6
0.4
0.2
0.0
-0.2
-0.4
-0.6
-0.8
1850
1860
1870
1880
1890
1900
1910
1920
1930
1940
1950
1960
1970
1980
1990
2000
CALENDAR YEAR

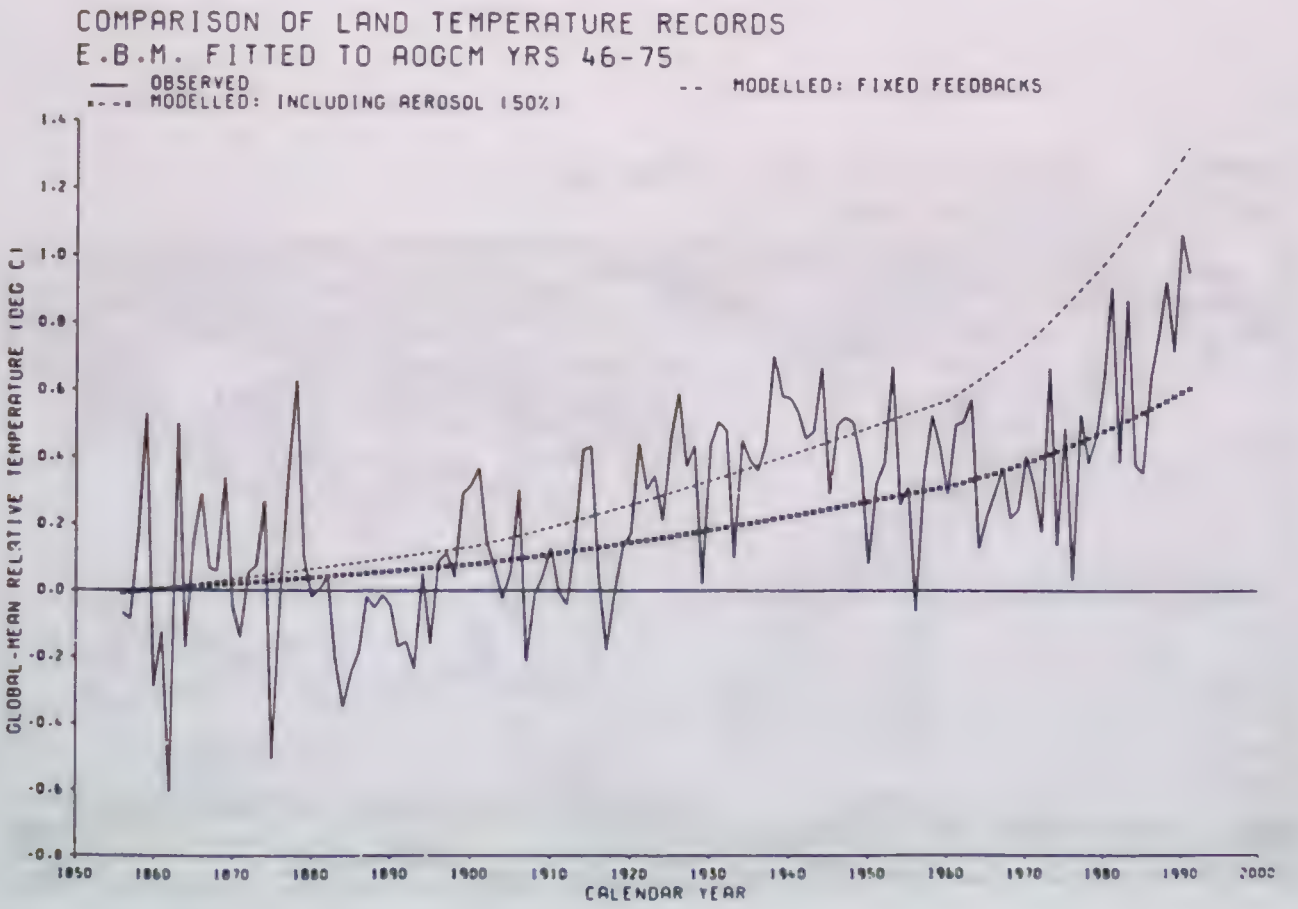
COMPARISON OF LAND TEMPERATURE RECORDS
E.B.M. FITTED TO AOGCM YRS 46-75
OBSERVED
MODELLED: INCLUDING AEROSOL (50%)
MODELLED: FIXED FEEDBACKS
GLOBAL-MEAN RELATIVE TEMPERATURE (DEG C)
1.4
1.2
1.0
0.8
0.6
0.4
0.2
0.0
-0.2
-0.4
-0.6
-0.8
1850
1860
1870
1880
1890
1900
1910
1920
1930
1940
1950
1960
1970
1980
1990
2000
CALENDAR YEAR

Figure 12(b)

(a)

COUPLED SLAB OCEAN-ATMOSPHERE MODEL
2XCO2 - 1XCO2 EQUILIBRIUM RESPONSE
10 YEAR ANNUAL MEAN SURFACE TEMPERATURE (DEG C)

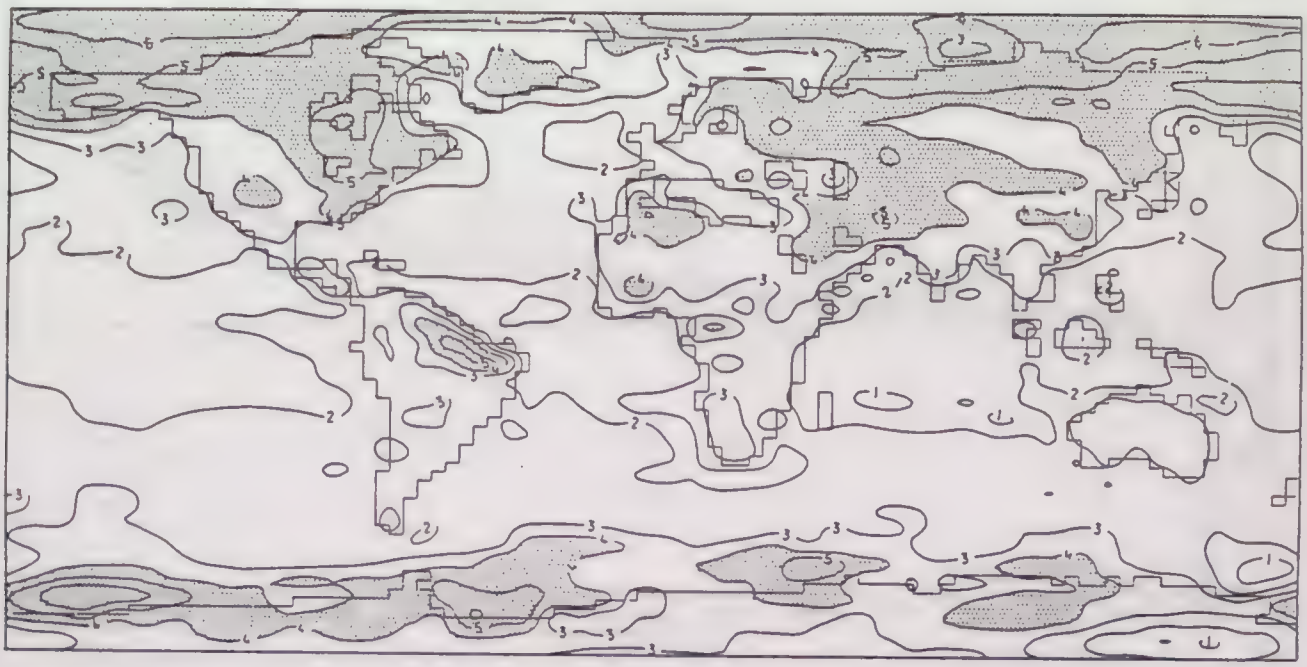

(b)

ANOMALY - CONTROL ANNUAL MEAN YEARS 66-75
SURFACE TEMPERATURE (DEG C)

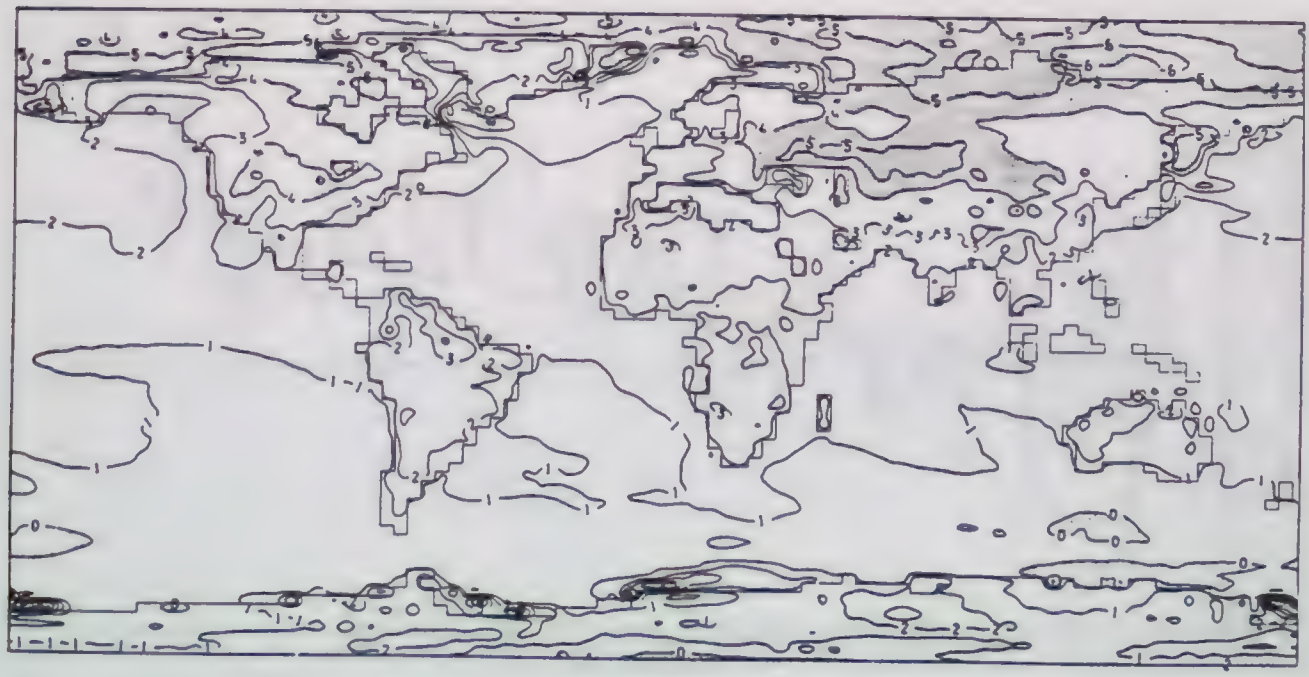

Figure 13

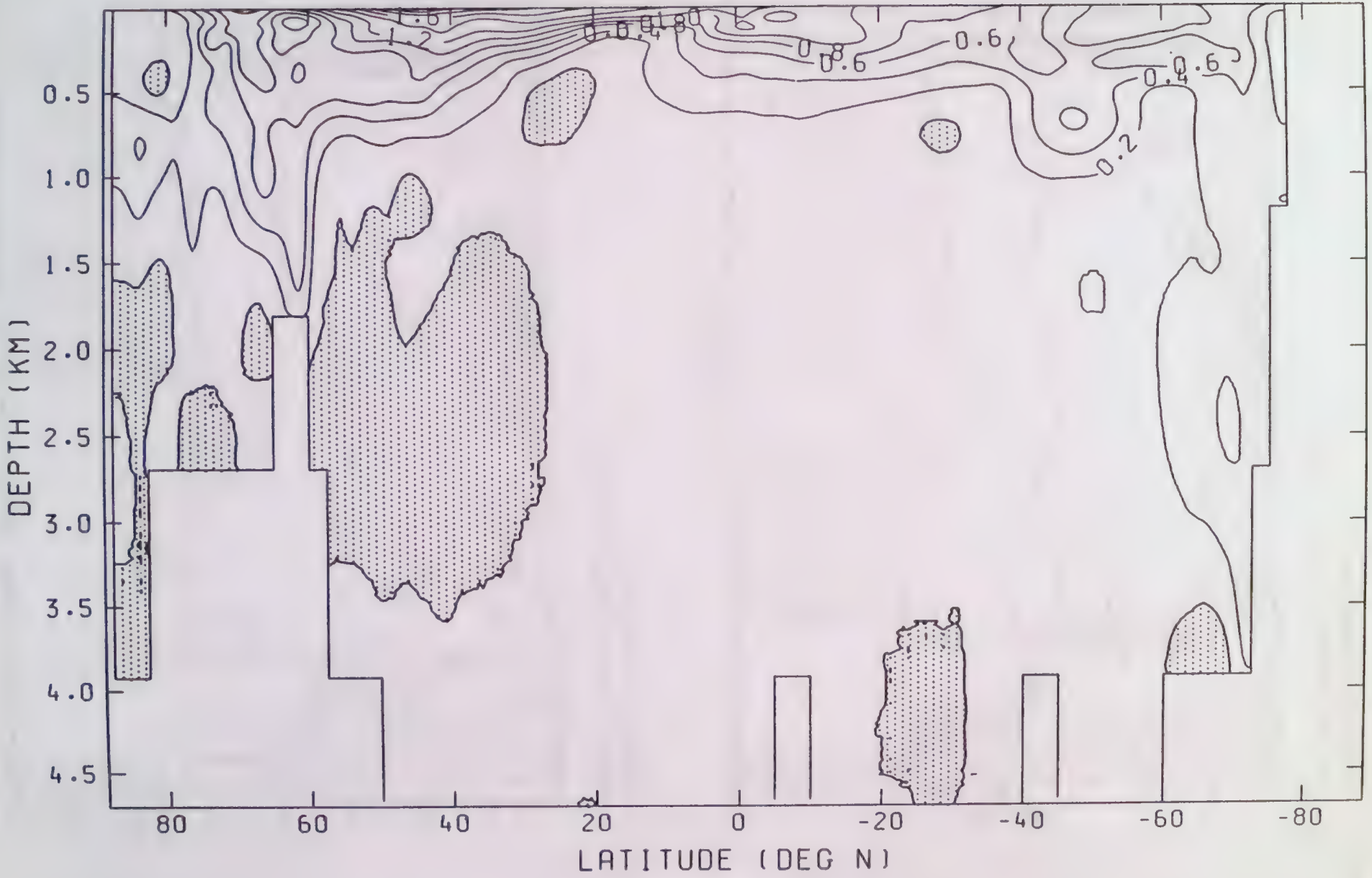
ZONAL-MEAN TEMPERATURE (DEG C)
ANOMALY MINUS CONTROL YEARS 66-75
GLOBAL OCEAN
DEPTH (KM)
0.5
1.0
1.5
2.0
2.5
3.0
3.5
4.0
4.5
80
60
40
20
0
-20
-40
-60
-80
LATITUDE (DEG N)
1.6
1.2
0.8
0.6
0.4
0.2

Figure 14

STREAMFUNCTION OF MERIDIONAL CIRCULATION (SV)

(a)

CONTROL YEARS 66-75
GLOBAL OCEAN: ANNUAL MEAN

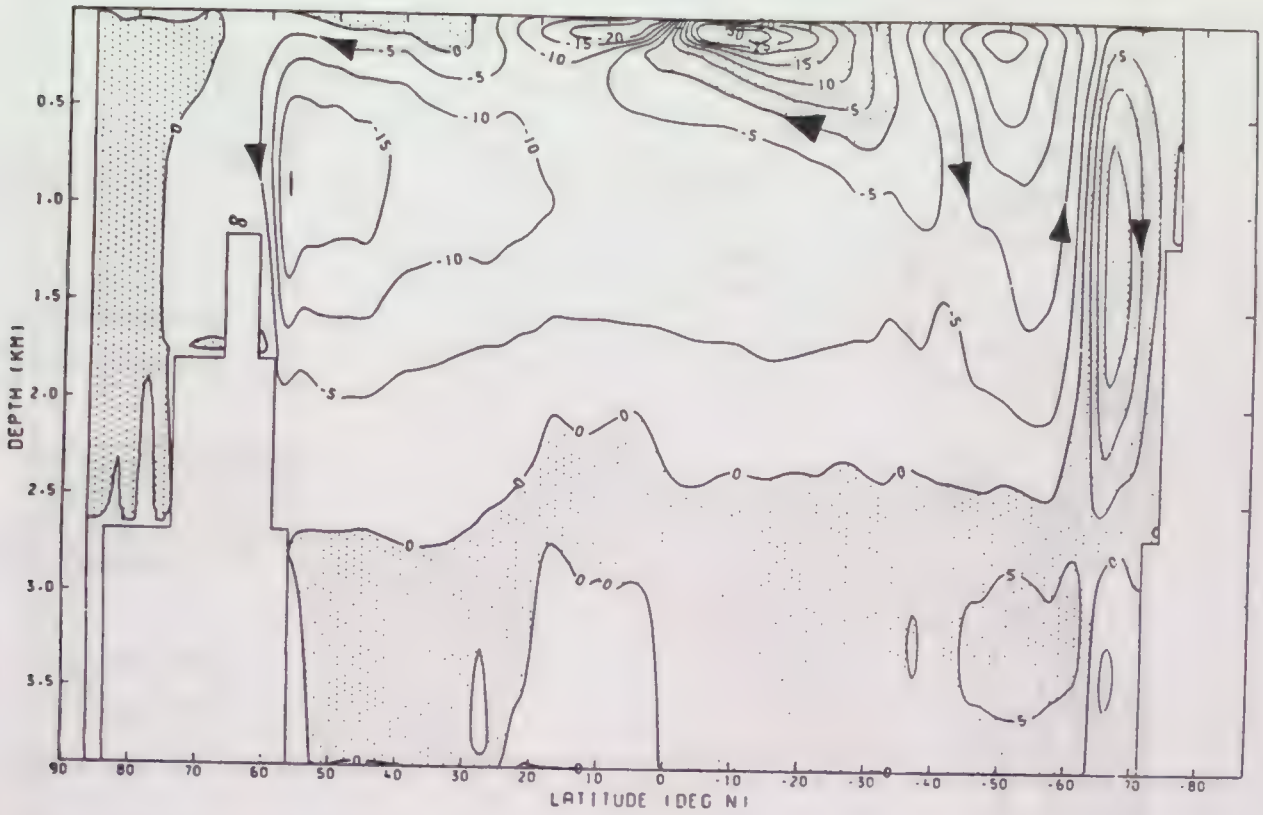

ANOMALY YEARS 66-75
GLOBAL OCEAN: ANNUAL MEAN

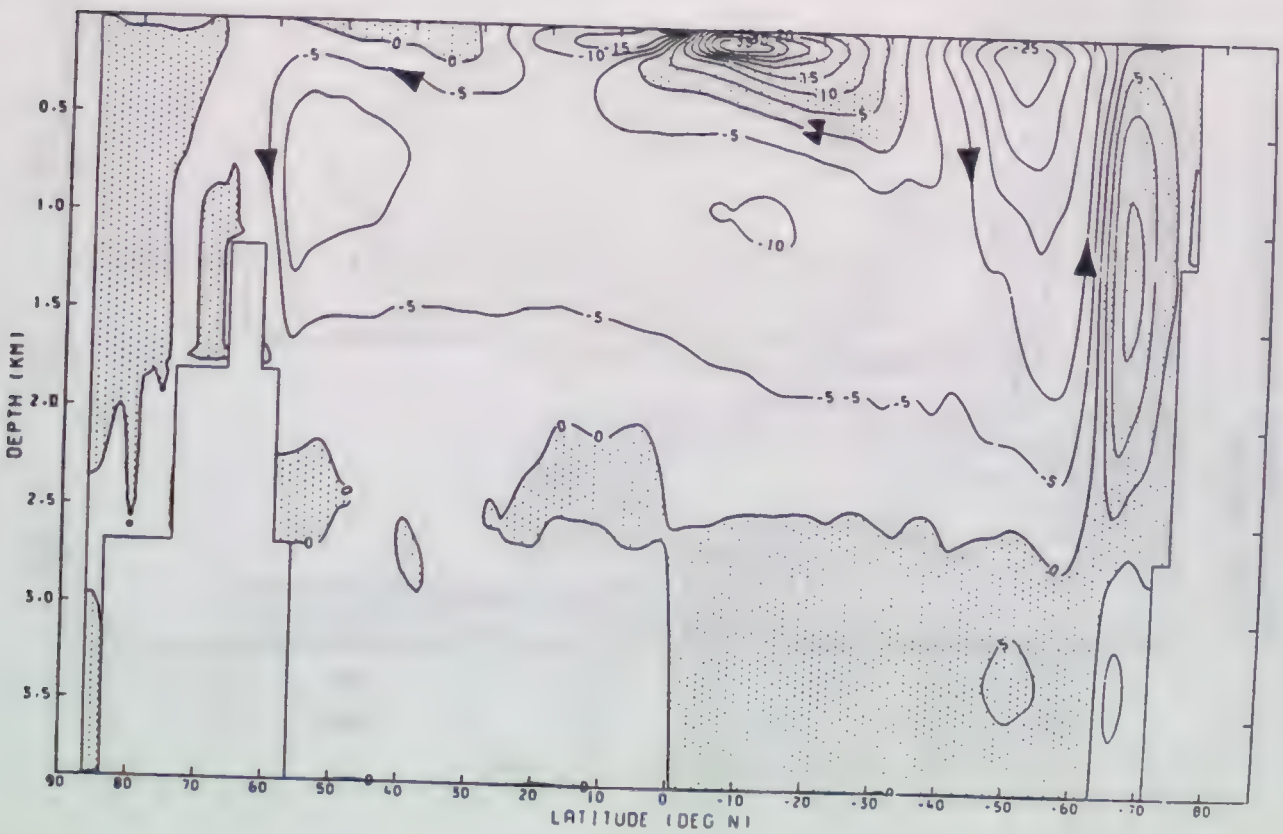

Figure 15

(a) ANOMALY - CONTROL D J F MEAN YEARS 66-75
SURFACE TEMPERATURE (DEG C)

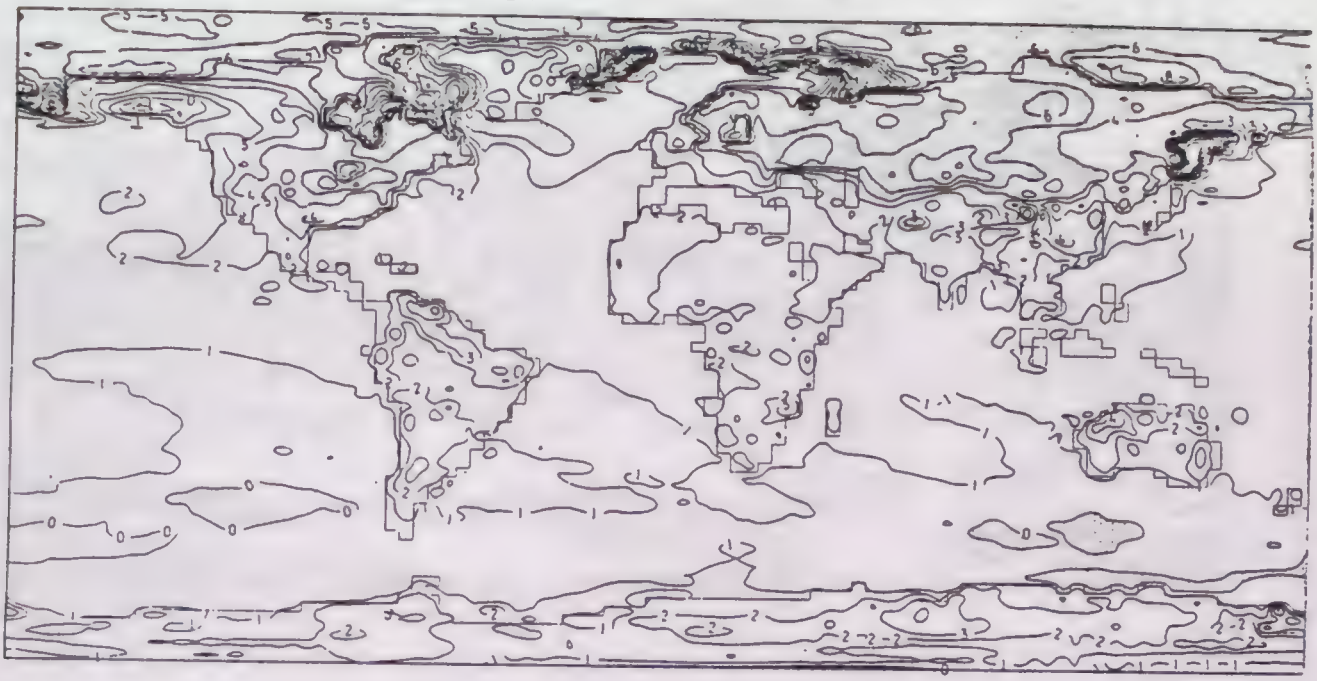

(b) ANOMALY - CONTROL J J A MEAN YEARS 66-75
SURFACE TEMPERATURE (DEG C)

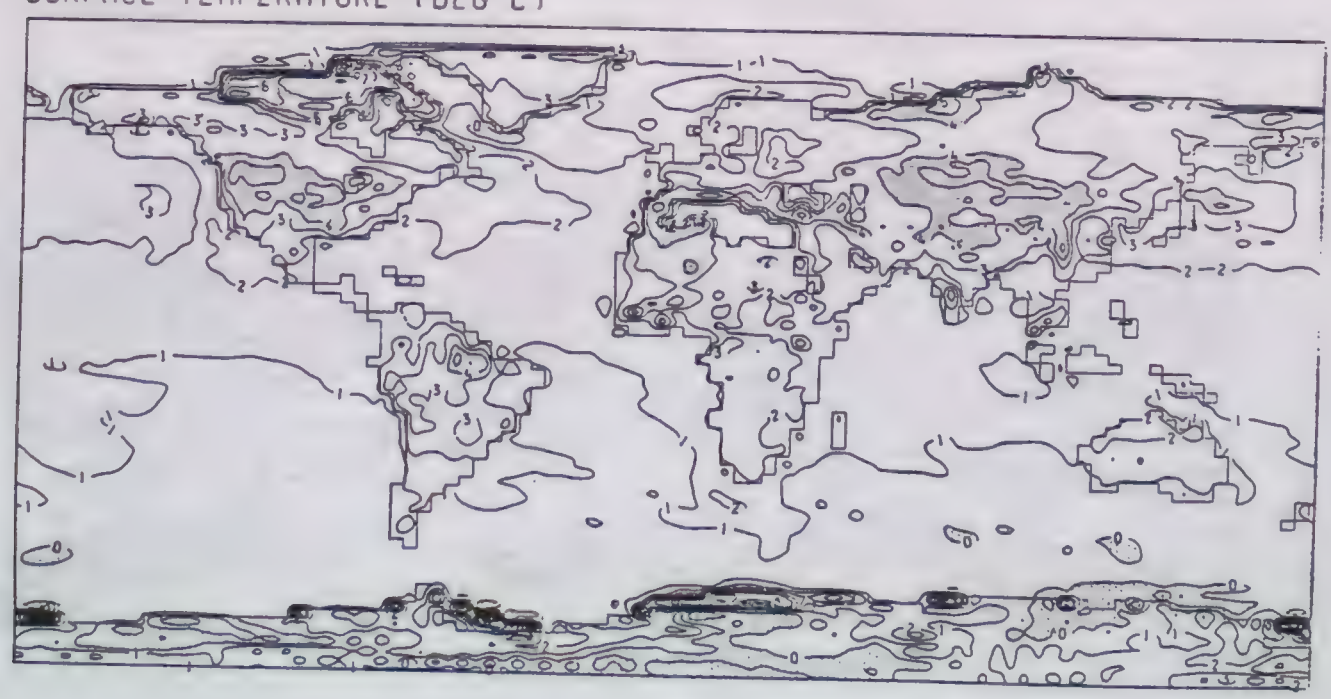

Figure 16

(a) ANOMALY - CONTROL D J F MEAN YEARS 66-75
TOTAL PRECIPITATION (MM/DAY)

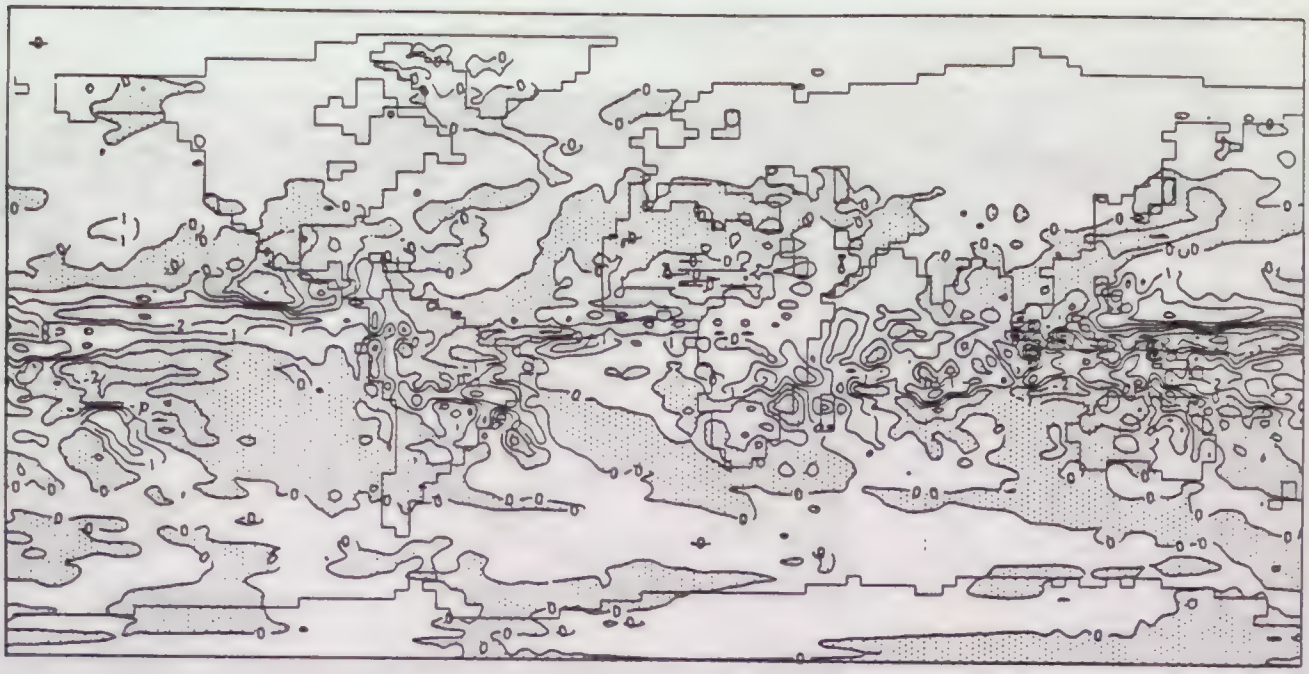

(b) ANOMALY - CONTROL J J A MEAN YEARS 66-75
TOTAL PRECIPITATION (MM/DAY)

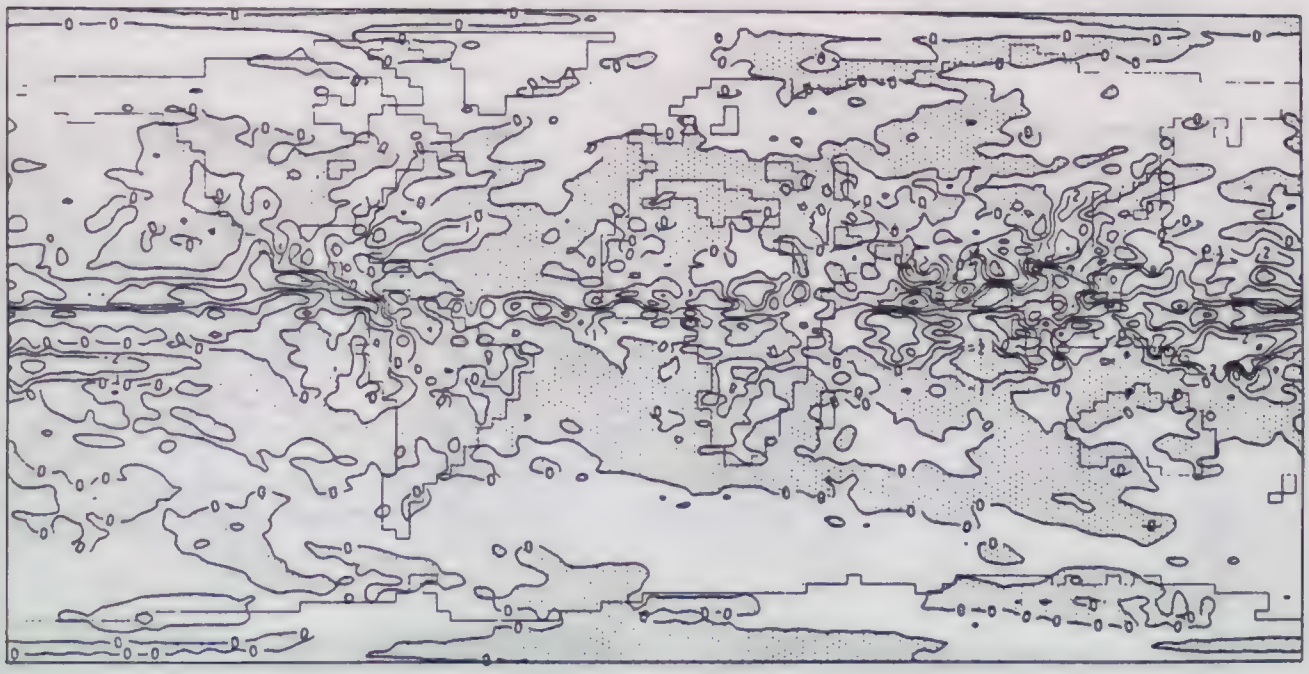

Figure 17

ANOMALY - CONTROL ANNUAL MEAN YEARS 21-30
SURFACE TEMPERATURE (DEG C)

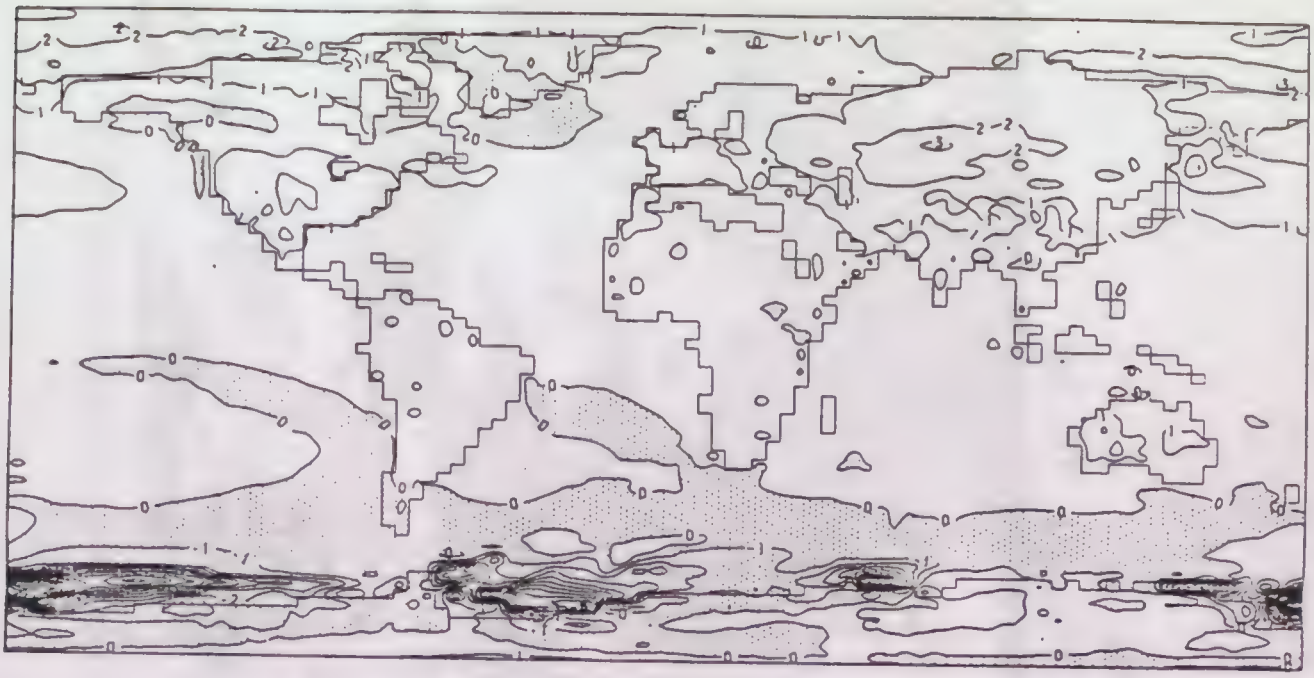

(b)

ANOMALY - CONTROL ANNUAL MEAN YEARS 41-50
SURFACE TEMPERATURE (DEG C)

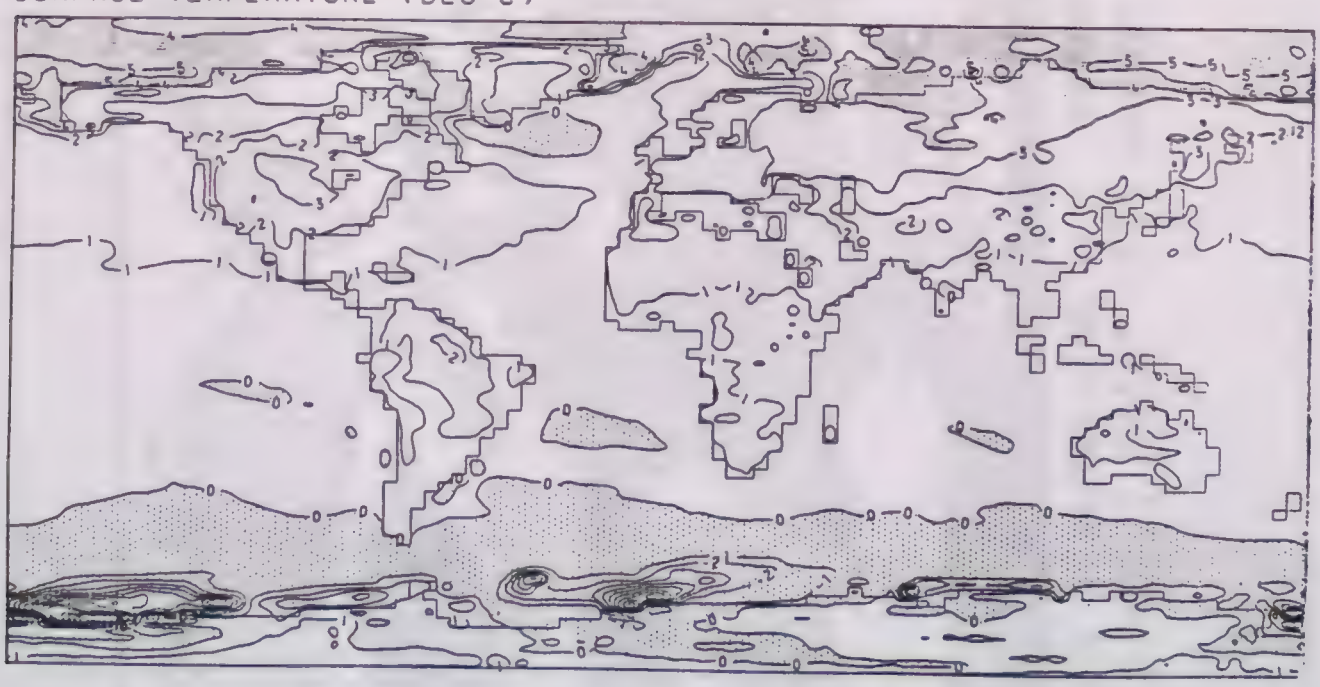

Figure 18

SIGNIFICANCE LEVEL (%): ANOMALY - CONTROL
SURFACE TEMPERATURE ANNUAL MEAN YEARS 21 TO 30

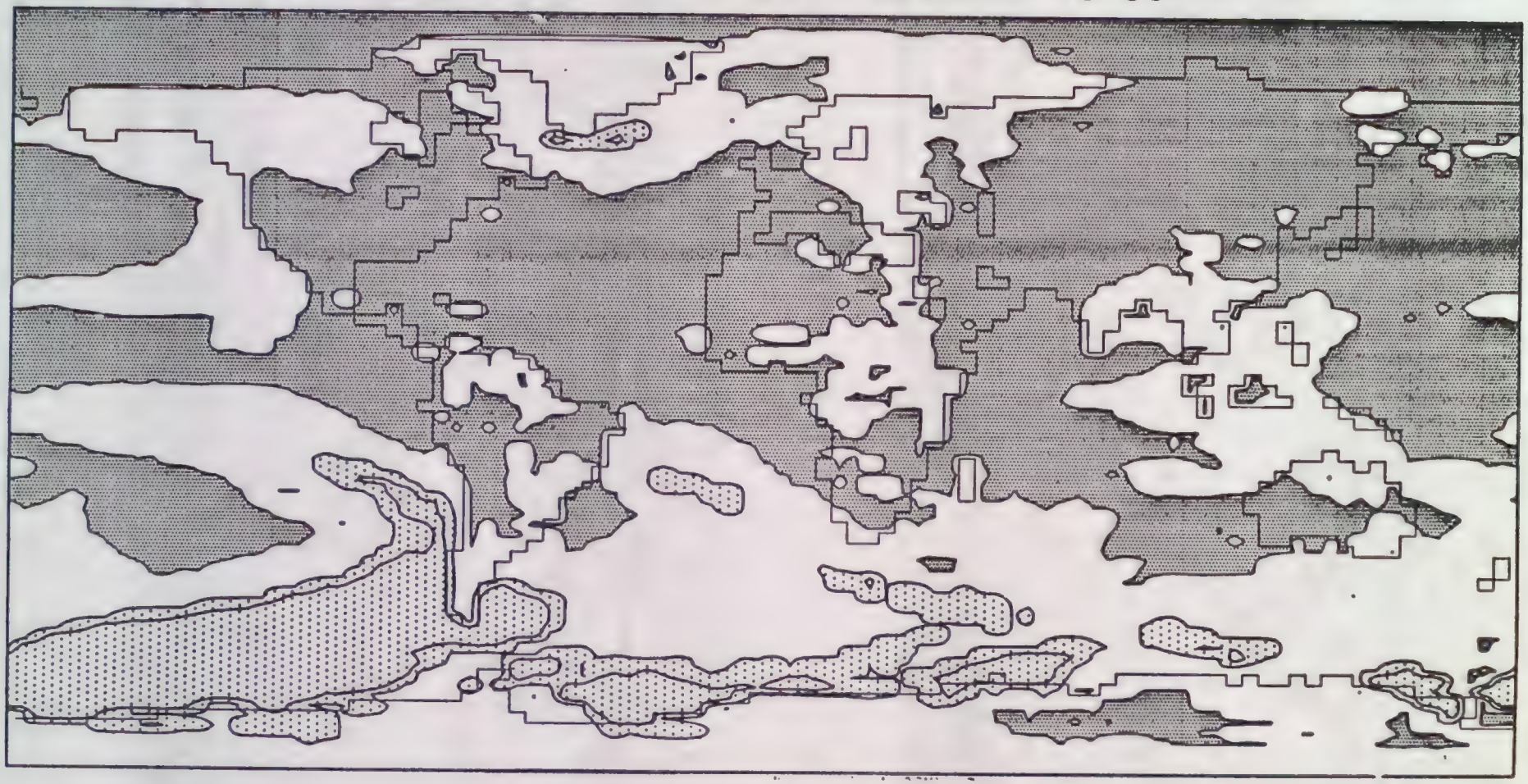

Figure 19

(a) ANOMALY - CONTROL D J F MEAN YEARS 66 TO 75
MEAN SEA LEVEL PRESSURE (MB)

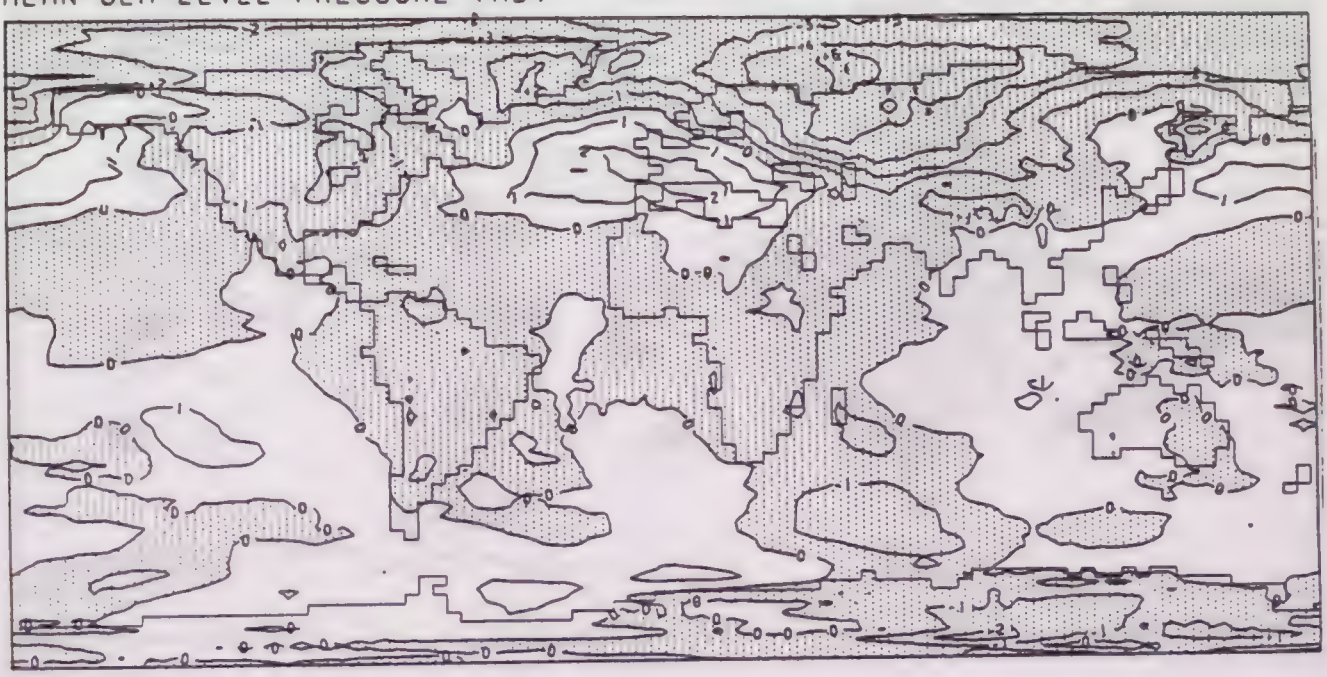

(b) ANOMALY - CONTROL J J A MEAN YEARS 66 TO 75
MEAN SEA LEVEL PRESSURE (MB)

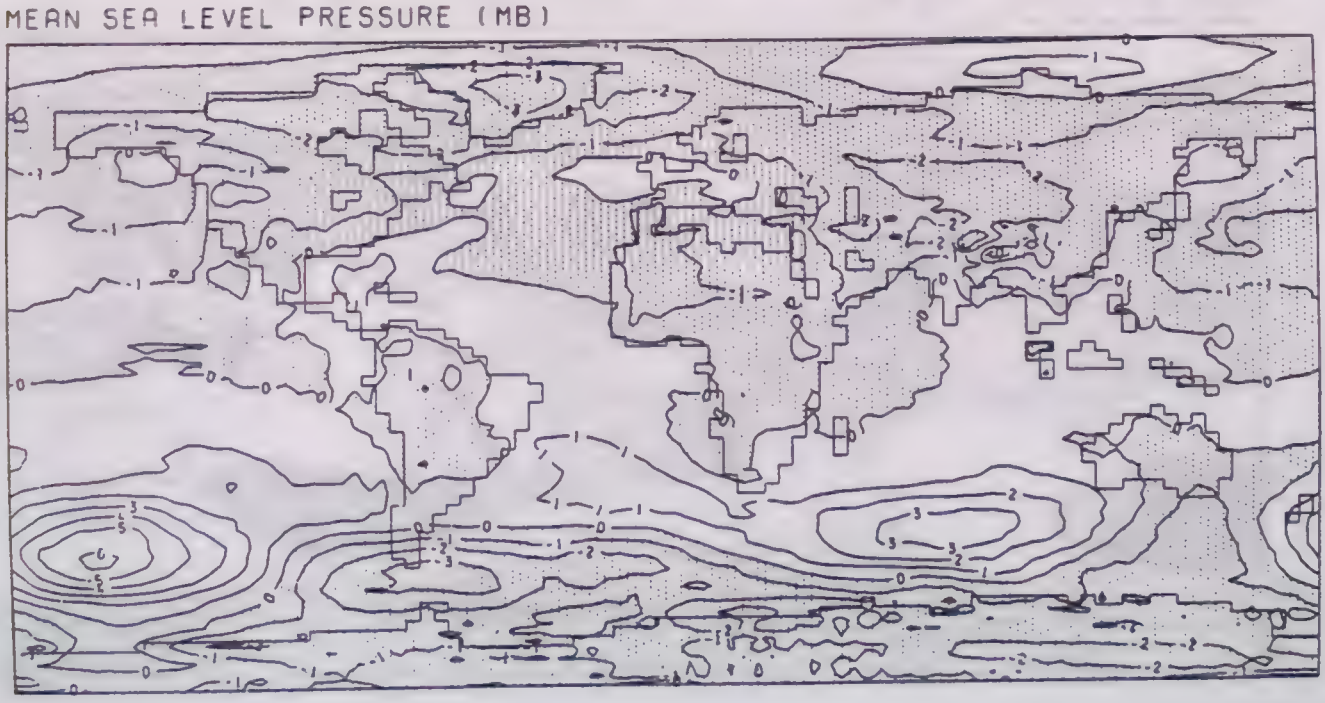

Figure 20

(a) SIGNIFICANCE LEVEL (%): ANOMALY - CONTROL
MEAN SEA LEVEL PRESSURE D J F MEAN YEARS 66 TO 75

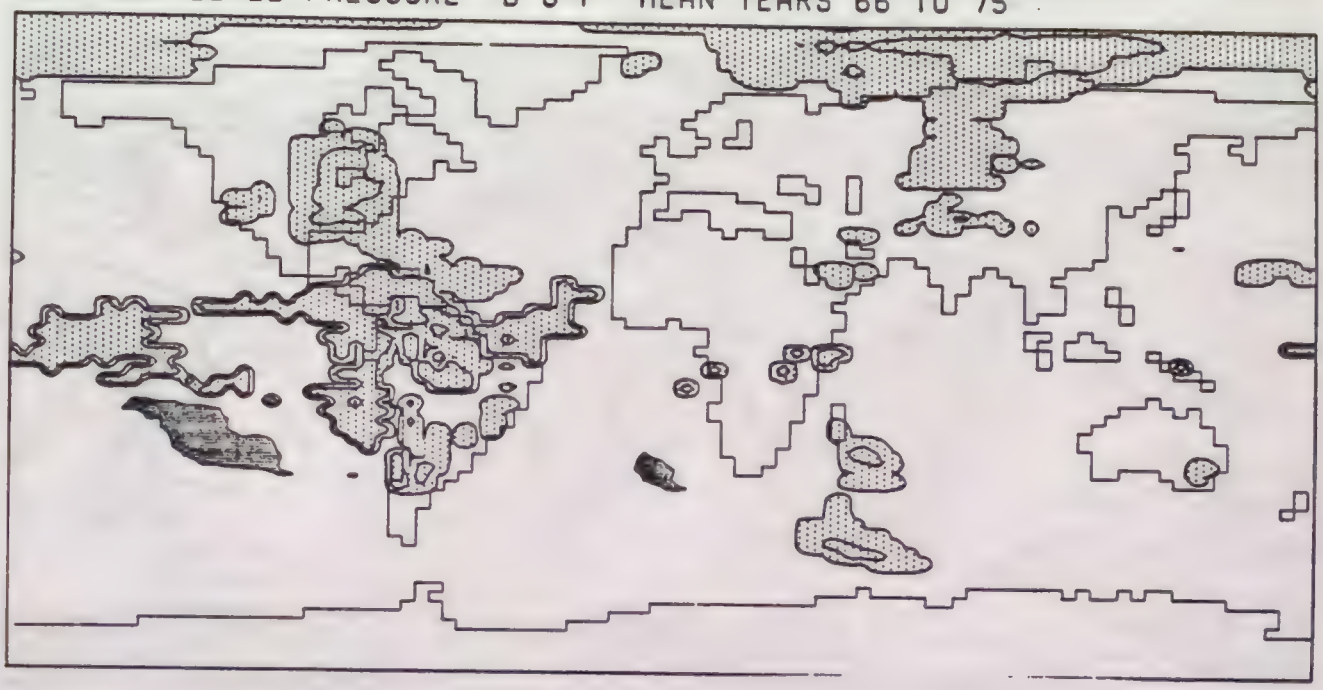

(b) SIGNIFICANCE LEVEL (%): ANOMALY - CONTROL
MEAN SEA LEVEL PRESSURE J J A MEAN YEARS 66 TO 75

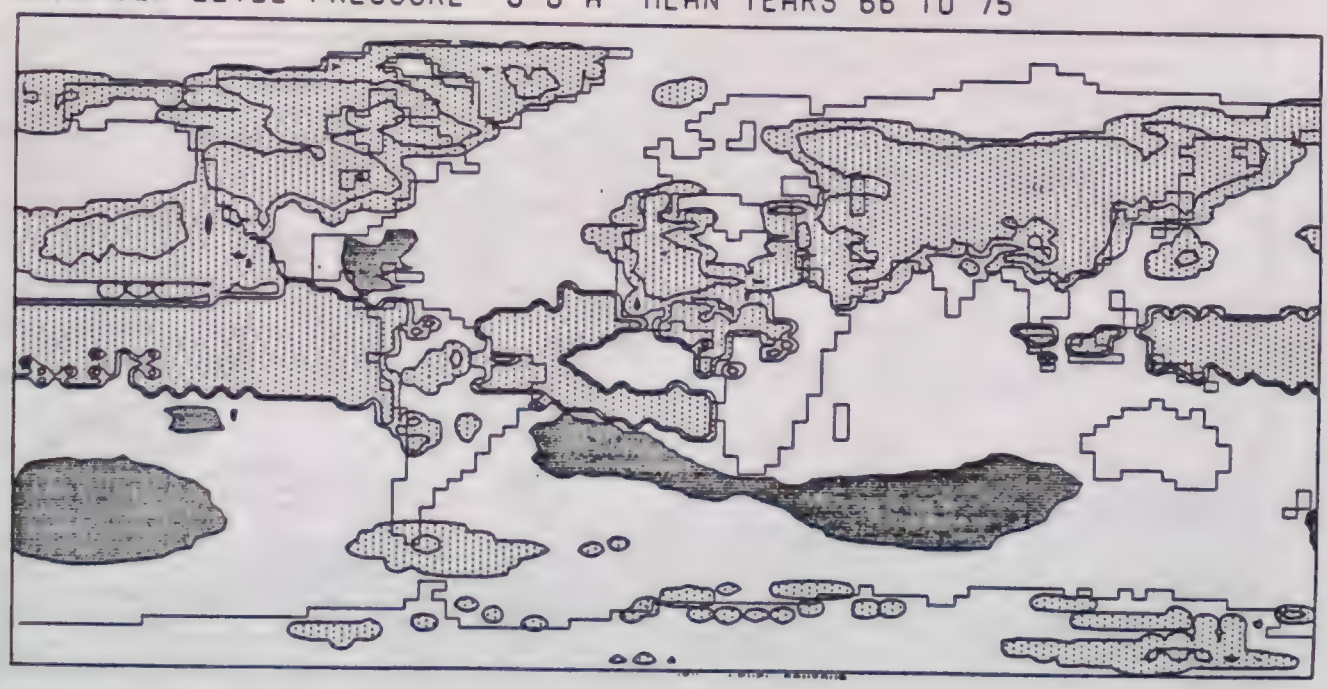

Figure 21

(a) ANOMALY - CONTROL D J F MEAN YEARS 21 TO 30
MEAN SEA LEVEL PRESSURE (MB)

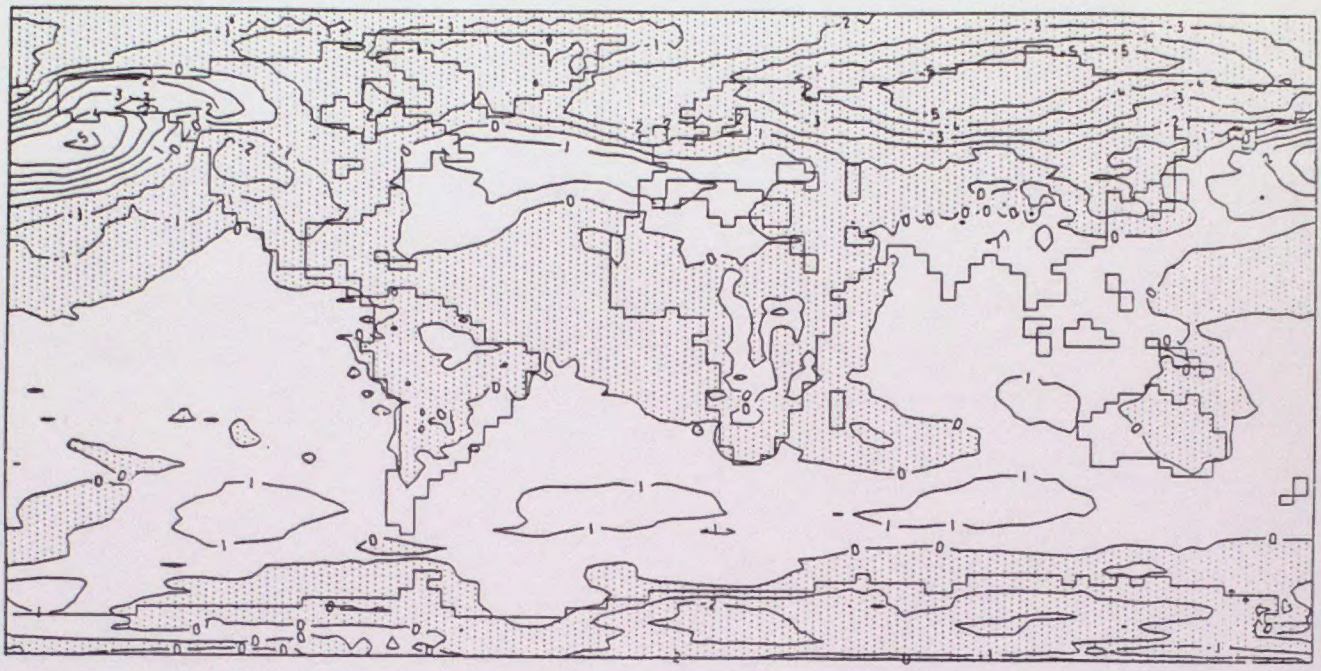

(b) ANOMALY - CONTROL J J A MEAN YEARS 21-30
MEAN SEA LEVEL PRESSURE (MB)

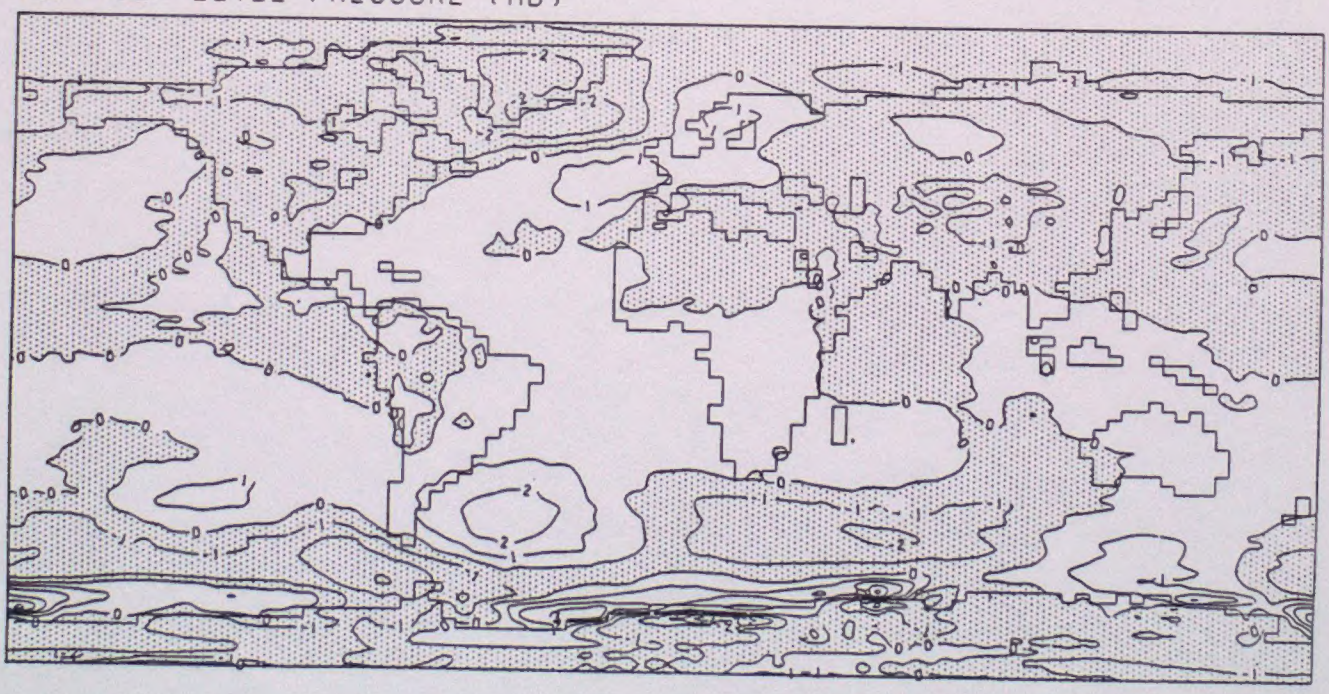

Figure 22

CLIMATE RESEARCH TECHNICAL NOTES

CRTN 1	Oct 1990	Estimates of the sensitivity of climate to vegetation changes using the Penman-Monteith equation. P R Rowntree
CRTN 2	Oct 1990	An ocean general circulation model of the Indian Ocean for hindcasting studies. D J Carrington
CRTN 3	Oct 1990	Simulation of the tropical diurnal cycle in a climate model. D P Rowell
CRTN 4	Oct 1990	Low frequency variability of the oceans. C K Folland, A Colman, D E Parker and A Bevan
CRTN 5	Dec 1990	A comparison of 11-level General Circulation Model Simulations with observations in the East Sahel. K Maskell
CRTN 6	Dec 1990	Climate Change Prediction. J F B Mitchell and Qing-cun Zeng
CRTN 7	Jan 1991	Deforestation of Amazonia - modelling the effects of albedo change. M F Mylne and P R Rowntree
CRTN 8	Jan 1991	The role of observations in climate prediction and research. D J Carson
CRTN 9	Mar 1991	The greenhouse effect and its likely consequences for climate change. D J Carson
CRTN 10	Apr 1991	Use of wind stresses from operational N.W.P. models to force an O.G.C.M. of the Indian Ocean. D J Carrington
CRTN 11	Jun 1991	A new daily Central England Temperature series, 1772-1991. D E Parker, T P Legg and C K Folland
CRTN 12	Jul 1991	Causes and predictability of Sahel rainfall variability. D P Rowell, C K Folland, K Maskell, J A Owen, M N Ward
CRTN 13	Jul 1991	Modelling changes in climate due to enhanced CO_2, the role of atmospheric dynamics, cloud and moisture. C A Senior, J F B Mitchell, H Le Treut and Z-X Li

CLIMATE RESEARCH TECHNICAL NOTES

CRTN 14	Sep 1991	Sea temperature bucket models used to correct historical SST data in the Meteorological Office. C K Folland
CRTN 15	Aug 1991	Modelling climate change, and some potential effects on agriculture in the U.K. P R Rowntree, B A Callander and J Cochrane
CRTN 16	Aug 1991	The Boreal Forests and Climate G Thomas and P R Rowntree
CRTN 17	Aug 1991	Development of a Stratosphere-Troposphere Data Assimilation System. R Swinbank.
CRTN 18	Sep 1991	A study of asynchronous coupling using a simple climate model. M K Davey.
CRTN 19	Sep 1991	The Oceanic Carbon Cycle. N K Taylor
CRTN 20	Nov 1991	Worldwide ocean-atmosphere surface fields in Sahel wet and dry years using provisionally corrected surface wind data. M N Ward
CRTN 21	Dec 1991	Coupled tropical ocean global atmosphere models at the UKMO. M K Davey, C Gordon, S Ineson and S Lawrence
CRTN 22	Dec 1991	Empirical parameterisation of tropical ocean-atmosphere coupling. M Allen, M K Davey, D L T Anderson and P D Killworth
CRTN 23	Feb 1992	The temporal evolution of Equatorial Currents in the Indian Ocean D L T Anderson, D J Carrington, R A Corry and C Gordon
CRTN 24	Feb 1992	Stratospheric analyses provided by the U.K. Meteorological Office M J Bailey, A O'Neill and V D Pope
CRTN 25	Feb 1992	Modelling interannual variability in the Indian Ocean using momentum fluxes from the UKMO and ECMWF operational weather analyses. D L T Anderson and D J Carrington

CLIMATE RESEARCH TECHNICAL NOTES

CRTN 26	Mar 1992	A GCM simulation of the impact of Amazonian deforestation on climate using an improved canopy representation J Lean and P R Rowntree
CRTN 27	Mar 1992	The parameterization of rainfall interception in GCMs A J Dolman and D Gregory
CRTN 28	Jun 1992	Development of worldwide marine data eigenvectors since 1985 A W Colman
CRTN 29	Jun 1992	A tropical ocean model with reduced physics M K Davey
CRTN 30	Jun 1992	International Temperature Workshop, Boulder, Colorado, USA, 16 January 1992 Edited by D E Parker
CRTN 31	Jul 1992	Simulation of clear-sky outgoing longwave radiation over the oceans using operational analyses A Slingo and M J Webb
CRTN 32	Sep 1992	A prediction of the transient response of climate J M Murphy